Polymer-Assisted Surface Modification of Silver Nanowire-Based Materials for Enhanced Multifunctional Performance

DISSERTATION

submitted to obtain the academic degree of Doctor of Natural Science (Dr.rer.nat.) of the Bayreuth Graduate School of Mathematical and Natural Sciences (BayNAT) of the University of Bayreuth

Presented by

Dan Fang

From JiangXi, China

Bayreuth, 2026

This thesis was carried out during the period from 01. 11. 2020 to 21. 05. 2026 in Bayreuth at the Chair of Macromolecular Chemistry II under the supervision by Prof. Dr. Andreas Greiner.

This is a full reprint of the thesis submitted to obtain the academic degree of Doctor of Natural Sciences (Dr.rer.nat) and approved by the Bayreuth Graduate School of Mathematical and Natural Sciences (BayNAT) of the University of Bayreuth.

Form of the dissertation: Monograph
Date of submission: 20. 01. 2026

Admission by the executive board: 19. 02. 2026

Date of defense: 21. 05. 2026

Action director: Prof. Dr. Jürgen Senker

Doctor committee: **Prof. Dr. Andreas Greiner** (**reviewer**)
Prof. Dr. André Gröschel (**reviewer**)
Prof. Dr. Anna Schenk (**chair**)
Prof. Dr. Matteo Bianchini

This dissertation is written as monograph. During my doctoral studies, the following two publications are part of my dissertation:

(1) Polyethyleneimine Controlled Impregnation of Silver Nanowires on Electrospun Ceramic Sponges

Dan Fang, Yitao Liu, Bin Ding, Andreas Greiner.

Macromolecular Materials and Engineering, 2024: 2400017.

https://doi.org/10.1002/mame.202400017

Disscussion in chapter 4.1. The serial number of the published article referenced in this thesis is 181.

(2) Interfacial Design Strategy for Polysiloxane-Bound AgNW/SiO_2 Sponges with Enhanced Mechanical, Thermal, and Adsorptive Properties.

Dan Fang, Andreas Greiner.

Submitted to *Small*, 2025.

Disscussion in chapter 4.2.

(3) Pt/TiO_2–x nanofibrous aerogel for effective nitrogen reduction: A simple strategy for simultaneous Pt formation and TiO_2–x vacancy engineering.

Meng Zhang, Jin Dai, Shengmei Huang, **Dan Fang**, Yitao Liu, Jianyong Yu, Bin Ding, Andreas Greiner.

Chinese Chemical Letters, 2022, 33(2), 1001–1005.

https://doi.org/10.1016/j.cclet.2021.08.069

Contents

LIST OF ABBREVIATIONS AND SYMBOLS

AgNWs	Silver nanowires
SiO_2	Silica dioxide
PVP	Polyvinylpyrrolidone
PEI	Polyethyleneimine
PVA	Polyvinyl alcohol
EG	Ethylene glycol
MB	Methylene blue
Ag	Silver
Pt	Platinum
$PtCl_6^{4-}$	Hexachloroplatinate
TEM	Transmission electron microscopy
XRD	X-ray diffractometer
UV-Vis	Ultraviolet-visible spectroscopy
TGA	Thermogravimetric analysis
SEM	Scanning electron microscopy
FCC	Face-centered cubic
SAED	Selected area electron diffraction
XPS	X-ray photoelectron spectroscopy
ECSA	Electrochemical active surface area
ICP-OES	Inductively coupled plasma optical emission spectroscopy
CV	Cyclic voltammetry
It	Chronoamperometric
MOR	Methanol oxidation reaction
DMFC	Direct methanol fuel cell
%	Percentage
s	Second
cm	Centimeter
µm	Micrometer

ml	Milliliter
t	Time
h	Hour
m	Mass
min	Minute
wt	Weight
k	Reaction rate constant

SUMMARY

This thesis focuses on surface modification as a central strategy for regulating the assembly behavior, structural stability, and functional performance of silver nanowire (AgNW)-based composite materials. Surface chemistry plays a decisive role in governing the interactions, spatial distribution, and structural evolution of nanomaterials within hierarchical porous frameworks. In this context, the study explores a series of surface-engineering approaches, including interfacial modification with polyethylenimine (PEI) to achieve controlled AgNW dispersion in silica sponges, polysiloxane surface coating to impart mechanical robustness and multifunctionality, and ligand-mediated surface regulation to tailor nanoscale alloy formation in PtAg catalysts. Collectively, these interconnected surface-modification strategies demonstrate how hierarchical control can be achieved from the molecular level to the macroscopic structure, ultimately dictating the physical, chemical, and catalytic properties of the resulting composite systems.

The first work investigates the precision and controllability of silica sponge surface modification by PEI, which regulates the distribution behavior of AgNWs. Experimental results indicated that varying PEI concentrations significantly affected the adsorption amount and distribution morphology of AgNWs in porous sponges, resulting in different conductive properties for the composite sponge materials. When the PEI concentration was 1 g/L, AgNWs formed a continuous conductive network within the SiO_2 sponge, leading to stable conductivity that varied with compression. This demonstrates that interfacial adsorption and molecular interactions directly define network continuity, though AgNW loading caused a decrease in mechanical strength. Overall, this work provides a reference for utilizing surface functionalization to precisely control nanowire distribution in 3D porous matrices.

Building on the importance of interfacial control demonstrated in the first work, the second work focuses on enhancing mechanical stability and expanding material functionality through surface modification. Here, AgNWs and silica fibers were coated with a polysiloxane layer generated from the hydrolysis and condensation of TEOS. This surface coating formed a continuous polysiloxane network that effectively reinforced the porous framework, significantly improving the mechanical robustness that was weakened in the

PEI-modified AgNW/SiO_2 sponge. Meanwhile, the embedded AgNWs created extended phonon scattering paths, which reduced thermal conductivity and improved thermal insulation performance. In addition, the organic segment of polysiloxane introduced new interfacial interaction sites, enabling hydrophobic and π–π stacking interactions with dye molecules such as methylene blue (MB), thereby enhancing adsorption performance. This part demonstrates that surface modification is not only a means of controlling nanowire dispersion, but also a versatile strategy for tailoring interfacial chemistry to integrate multiple functional behaviors, including mechanical reinforcement, thermal regulation, and pollutant adsorption. Thus, the second study deepens the role of surface modification from microstructural control to multifunctional performance engineering.

The third work further advances surface modification to the molecular scale, focusing on how organic ligands regulate metal nucleation, growth, and alloy formation in nanostructures. PVP-coated AgNWs were used as sacrificial templates for synthesizing PtAg alloys, allowing direct investigation of how ligand coverage, coordination sites, and binding strength impact morphology and composition evolution. Results showed that PVP not only induced preferential growth along the (111) facet, but also controlled Pt particle nucleation and the extent of galvanic replacement between Pt ions and AgNWs. When PVP coverage dropped below 1.84 wt%, these regulatory effects diminished, leading to changes in alloying degree, particle size, and surface crystal facets, ultimately influencing catalytic performance toward methanol oxidation. Although the assembled direct methanol fuel cell (DMFC) exhibited limited performance due to incomplete catalyst dispersion on the diffusion layer, this work provides fundamental insight into how surface ligands govern nanoscale alloy formation processes. It highlights that surface modification at the molecular scale is critical for precise catalytic interface engineering, which in turn determines electrocatalytic activity and durability.

Taken together, the three studies establish a coherent framework in which surface modification acts as the core design principle linking microstructure, interface evolution, and material functionality. By progressively advancing control from porous network-level nanowire distribution, to composite interface stabilization, and further to molecular ligand-directed alloy formation, this work illustrates how hierarchical surface engineering can be used to achieve structural precision.

ZUSAMMENFASSUNG

Diese Arbeit konzentriert sich auf die Oberflächenmodifikation als Schlüsselstrategie zur Regulierung der Assemblierung, strukturellen Stabilität und funktionalen Leistungsfähigkeit silbernanodrahtbasierter (AgNW) Verbundmaterialien. Die Oberflächenchemie spielt eine entscheidende Rolle dafür, wie sich Nanomaterialien innerhalb hierarchisch poröser Gerüststrukturen verteilen, miteinander wechselwirken und weiterentwickeln. Dementsprechend folgt diese Studie einem schrittweisen Forschungsansatz: 1. interfaciale Modifikation mittels PEI zur präzisen Regulierung der AgNW-Dispersion in Silica-Schwämmen. 2.Oberflächenbeschichtung mit Polysiloxan zur Integration mechanischer Robustheit und multifunktionaler Eigenschaften. 3. ligandengesteuerte Oberflächenkontrolle zur Einstellung der nanoskaligen Legierungsbildung in PtAg-Katalysatoren. Diese drei Schritte zeigen gemeinsam, wie Oberflächenmodifikation eine hierarchische Kontrolle von der molekularen bis zur makrostrukturellen Ebene ermöglicht und letztlich die physikalischen, chemischen und katalytischen Eigenschaften der Verbundsysteme determiniert.

Die erste Studie untersucht die Präzision und Steuerbarkeit der Oberflächenmodifikation von Silica-Schwämmen durch PEI, welches das Verteilungsverhalten von AgNWs reguliert. Die experimentellen Ergebnisse zeigen, dass unterschiedliche PEI-Konzentrationen die Adsorptionsmenge und Verteilungsmorphologie der AgNWs im porösen Gerüst signifikant beeinflussen und dadurch die elektrischen Eigenschaften des Verbundschwamms verändern. Bei einer PEI-Konzentration von 1 g/L bildeten die AgNWs ein kontinuierliches leitfähiges Netzwerk innerhalb des SiO_2-Schwammes, was zu einer stabilen, kompressionsabhängigen Leitfähigkeit führte. Dies demonstriert, dass interfaciale Adsorption und molekulare Wechselwirkungen unmittelbar die Netzwerkkontinuität definieren, obwohl die Integration der AgNWs zu einer Abnahme der mechanischen Festigkeit führte. Insgesamt liefert diese Studie eine Referenz für den gezielten Einsatz der Oberflächenfunktionalisierung zur präzisen Kontrolle der Nanodrahtverteilung in dreidimensionalen porösen Matrizen.

Aufbauend auf der Bedeutung der Grenzflächenkontrolle konzentriert sich die zweite Studie auf die Verbesserung der mechanischen Stabilität und die Erweiterung funktionaler

Eigenschaften durch eine Oberflächenmodifikation. Hier wurden AgNWs und Silicafasern mit einer durch Hydrolyse und Kondensation von TEOS erzeugten Polysiloxan-Schicht ummantelt. Diese Beschichtung bildete ein kontinuierliches Polysiloxan-Netzwerk, das das poröse Gerüst effektiv verstärkte und die in der PEI-modifizierten AgNW/SiO_2-Struktur verringerte mechanische Robustheit deutlich verbesserte. Gleichzeitig erzeugten die eingebetteten AgNWs verlängerte Phononstreupfade, was die Wärmeleitfähigkeit reduzierte und die Wärmedämmeigenschaften verbesserte. Darüber hinaus bot das organische Segment des Polysiloxans neue Grenzflächeninteraktionsstellen, die hydrophobe sowie π–π-Wechselwirkungen mit Farbstoffmolekülen wie Methylenblau ermöglichten und so die Adsorptionsleistung erhöhten. Diese Studie zeigt, dass Oberflächenmodifikation nicht nur der Steuerung der Nanodrahtdispersion dient, sondern eine vielseitige Strategie zur maßgeschneiderten Einstellung der Grenzflächenchemie und zur Kombination mechanischer, thermischer und adsorptiver Funktionalitäten darstellt.

Die dritte Studie verschiebt den Schwerpunkt der Oberflächenmodifikation auf die molekulare Skala und untersucht, wie organische Liganden die Metallnukleation, das Wachstum und die Legierungsbildung in Nanostrukturen steuern. PVP-beschichtete AgNWs dienten hierbei als opfernde Templates zur Synthese von PtAg-Legierungen, wodurch der Einfluss von Ligandenabdeckung, Koordinationsstellen und Bindungsstärke auf Morphologie- und Zusammensetzungsentwicklung direkt studiert werden konnte. Die Ergebnisse zeigten, dass PVP ein bevorzugtes Wachstum entlang der (111)-Fläche induzierte, die Pt-Keimbildung kontrollierte und den galvanischen Austausch zwischen Pt-Ionen und AgNWs regulierte. Bei PVP-Abdeckungen unter 1,84 Gew.-% gingen diese regulierenden Effekte verloren, was zu Änderungen im Legierungsgrad, der Partikelgröße und den Oberflächenstrukturen führte und letztlich die katalytische Leistung bei der Methanoloxidation beeinflusste.

Zusammenfassend etabliert diese Arbeit ein kohärentes Rahmenkonzept, in dem die Oberflächenmodifikation als zentrales Gestaltungsprinzip die Mikrostruktur, die Grenzflächenentwicklung und die funktionalen Eigenschaften miteinander verknüpft. Durch die schrittweise Erweiterung der Kontrolle von der Nanodrahtverteilung in porösen Netzwerken, über die Stabilisierung der Verbundschnittstellen bis hin zur ligandengesteuerten Legierungsbildung wird gezeigt, wie hierarchische Oberflächenmodifikation zur strukturellen Präzision und Leistungsoptimierung genutzt werden kann.

Chapter 1

INTRODUCTION

The rational design and exploration of new materials with targeted functionalities constitute a key pathway through which materials science addresses societal development demands, as suggested by previous studies. Surface modification is a widely used technique that impacts desirable short-term or long-term properties to materials, thereby enhancing their functionality. By modifying the surface, material performance can be significantly enhanced in terms of electrical conductivity, thermal conductivity, catalysis, and dye adsorption, while the application scope can be broadened to enable operation under more diverse conditions. Among various surface modification strategies, polymers are particularly attractive due to their rich functional groups, flexible molecular chain structures, and highly tunable physical and chemical properties, allowing effective interaction with material surfaces through chemical reactions or physical adsorption.

Due to the unique structures and properties of porous and nanomaterials, they have garnered considerable attention in fields such as adsorption, catalysis, biomedicine, sensors, and energy. Polymer surface modification techniques can further enhance the functionality, stability, and application scope of these materials. For example, silica sponges, typical three-dimensional porous materials, have a high specific surface area and adjustable pore structure, making them widely used in adsorption, filtration, and catalysis. Silica sponges are often used as a base structure in composite materials, and through polymer surface modification, new surface characteristics can be introduced to further enhance their physical and chemical properties. Among various nanomaterials, Silver nanowires(AgNWs) have attracted increasing attention. AgNWs are one-dimensional silver nanostructures with diameters typically ranging from 10-200 nm and lengths from 5-100 μm. Due to their high electrical conductivity, AgNWs have great potential in electrical applications.

In this thesis, my research focuses on modulating the properties of materials while maintaining the inherent chemical structure of polymers, utilizing various methods to achieve this modulation. The study offers some reference for several key challenges in surface

modification techniques. First, I explored how to precisely control the internal morphology distribution of composite materials to achieve high accuracy and controllability in surface modification. Second, I investigated the possibility of introducing multifunctional applications to composite materials through surface modification, including improvements in mechanical properties, thermal stability, and other combined performance attributes. Furthermore, I conducted detailed studies on achieving nanoscale precision control at the molecular level through surface modification techniques. Such nanoscale control is crucial for adjusting material microstructures, thereby significantly enhancing the application potential of the samples in specific fields. In the following sections, I will introduce the background knowledge related to the polymers used in this research (such as PEI, polysiloxane, and PVP), as well as porous materials and nanomaterials. Additionally, I will discuss the preparation methods, including electrospinning and freeze-drying, along with the applications of the samples in electrical conductivity, thermal insulation, dye adsorption, and electrochemical catalytic oxidation. These topics are closely related to the work presented in this thesis and will be elaborated in the subsequent chapters. The schematic diagram shown in Figure 1.1 provides an overview of the overall research work.

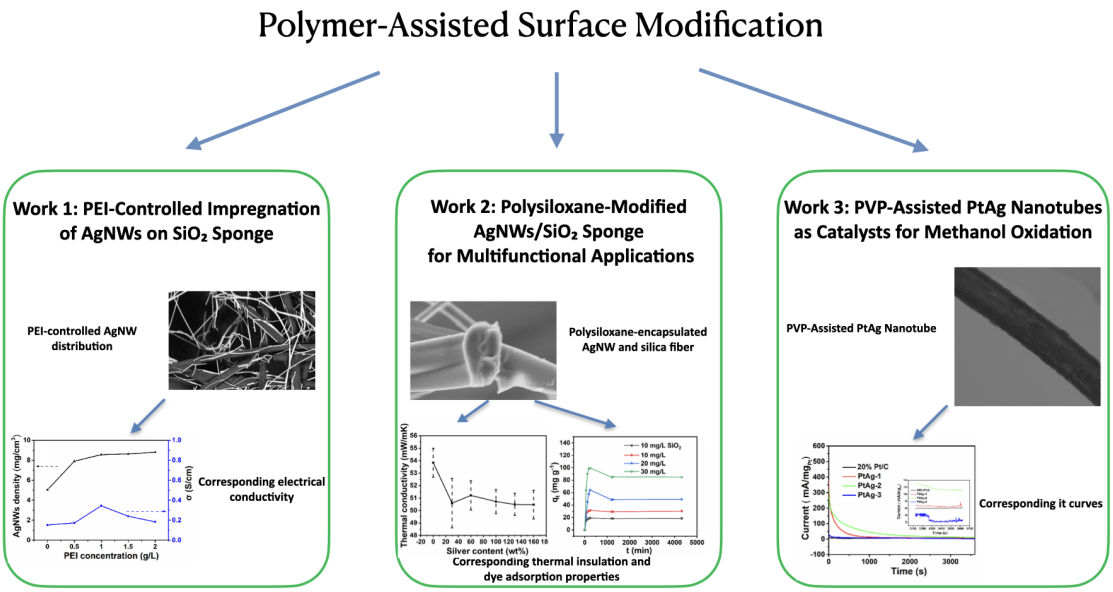

Figure 1.1: Polymer-assisted surface modification strategies illustrated through three research works: (1) PEI-controlled impregnation of AgNWs on SiO_2 sponge, (2) Polysiloxane-modified AgNWs/SiO_2 sponge for multifunctional applications, and (3) PVP-assisted PtAg nanotubes as catalysts for methanol oxidation.

Chapter 2

THEORETICAL BACKGROUND

2.1 SURFACE MODIFICATION

Surface modification refers to the introduction of specific chemical or physical changes on the surface of a material to alter its chemical composition, surface morphology, and functional properties [1–5]. The nanomaterials mentioned above are often modified by polymers to obtain high-performance composite materials that meet more usage requirements. For example, surface modification can change the chemical composition of nanomaterials, improve their stability to extend their service life, regulate their distribution to affect electrical/thermal properties, and adjust the electronic surface structure to enhance catalytic performance, improve chemical reaction rates and selectivity, or alter biocompatibility and biological activity to control drug release. composition through coating, impregnation, deposition, sol–gel processes, and related approaches; physical treatment modifies the surface morphology and structure via electrophoresis, spraying, low-energy plasma beam irradiation, and plasma treatment; and structural modification changes the geometric form and micro-/nanoscale architectures to regulate surface performance. Higher requirements of surface modification technology for practical applications, inevitably lead to new demand for the development of surface modification technology.

2.1.1 POLYETHYLEIMINE

The precision and control of surface modification are beneficial for targeting and functionalization in the preparation of nanomaterials in composites. Polyethyleimine (PEI) is a soluble, functionalized polymer that contains an amine group and it has two common structures: linear and branched. The branched PEI is synthesized by the cationic polymerization with the aziridine under basic or acidic conditions (Figure 2.1). The average molecular weight of branched PEI remains within a certain range between 20,000 g/mol

and 50,000 g/mol. If we want to get high molecular weight branched PEI during the synthesis process, we can use the bifunctional connecting agents, such as dichloroethane and epichlorohydrin derivatives [6].

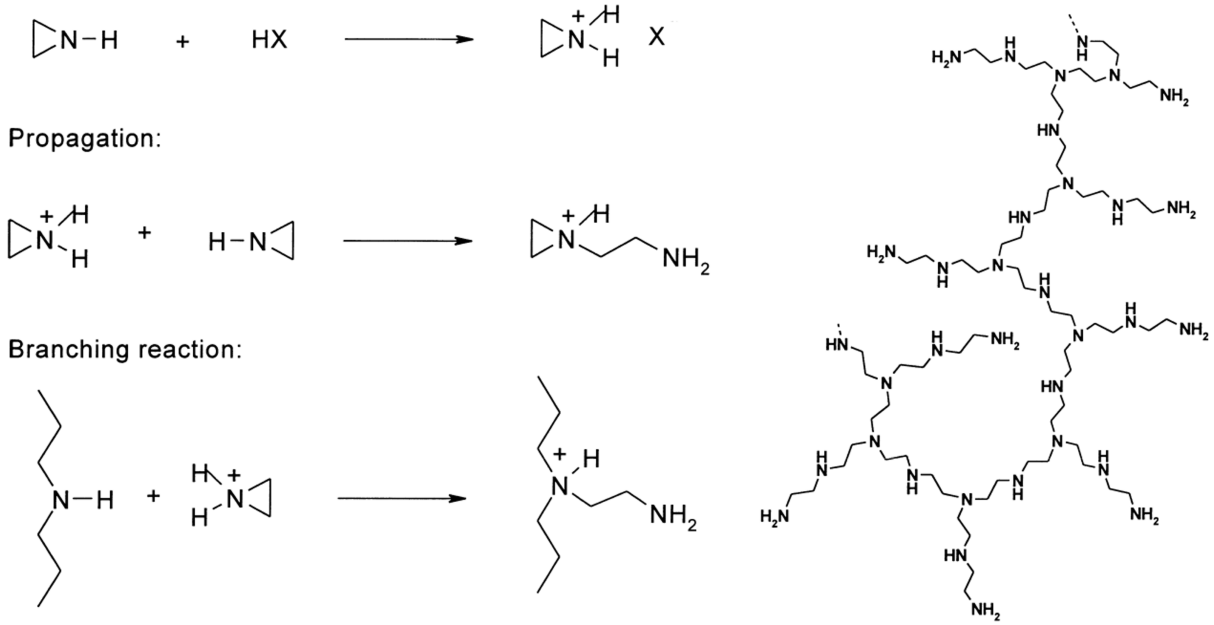

Figure 2.1: Mechanism of acid catalysed polymerization of ethylene imine in aqueous solution (here: X=Cl).

PEI is often used in inks, coatings, and adhesives, among other applications. The coexistence of polar amine groups and hydrophobic vinyl groups in PEI allows it to effectively interact with diverse substances through both chemical and physical interactions. PEI frequently exists as a polycation in aqueous solutions and is used to adsorb anions and chelate heavy metal ions. Due to its structure, which contains highly reactive primary and secondary amines, PEI can react with aldehydes, isocryanate compounds, and acid gases. This makes it useful as an expoxy resin modifier, aldehyde adsorbent, and dye fixing agent.

By studying the complexation of PEI with divalent copper ions, researchers have investigated the relationship between the steric coordination of metal ions and nitrogen atoms in PEI, the degree of branching, and the molecular weight of PEI [7–9]. Huang et al. also explored the application of PEI in wastewater treatment by reducing cationic PEI caged platinum nanomaterials in-situ onto a bacterial cellulose substrate to prepare a multifunctional biosorbent (PEI-Pt@BC membrane) [10]. It was confirmed that the PEI-Pt@BC membrane has a higher adsorption capacity for anionic dyes compared to cationic dyes due to the positively charged PEI. The interaction between PEI and silver nanoparticles is particularly fascinating and has attracted significant attention [11–14]. For example, Beuggen et al. stabilized silver nanoparticles on the surface of a polydopamine-coated composite membrane using superhydrophilic titanium dioxide and polyethyleneimine through vacuum fil-

tration. This combination of organic and inorganic hybrid coatings endowed the composite membranes with excellent isolation properties. The in-situ formation of silver nanoparticles on the composite membranes resulted in high antibacterial activity, producing a membrane material with excellent dye-blocking capabilities and a high bacterial inhibition rate. Some scientists have also synthesized PEI-functionalized silver nanoparticles directly using hydrothermal methods to study their antimicrobial properties [15]. In addition to investigating the antimicrobial and dye adsorption properties of PEI and Ag composites, researchers have extensively studied the electrical conductivity of these composites, given that silver nanowires possess ultra-high electrical conductivity [16–19]. For instance, Heung et al. create composites of Poly(3,4-ethylenedioxythiophene)(styrenesulfonate) (PEDOT:PSS) and silver nanowires(AgNWs) using a layer-by-layer assembly method with counterionic compounds, including econometric tris(2-aminoethyl)amine, chitosan, and PEI [20]. These composites are characterized by strong electrostatic interactions between the materials and PEDOT:PSS, forming reliable interfaces during the layer-by-layer process. This results in composites with low contact resistance of 5 ohms and strong mechanical durability, suitable for applications in electrospun fabrics and 3D electronics based on aqueous tutored soldering and transfer technology. Kimitaka et al. investigated partially branching PEI into PEG chains, utilizing the amine sites in PEI-mPEG to adsorb anionic blue dye. They explored how the branching rate of PEG chains on PEI affected ligand exchange behavior and the dispersive stability of the AgNWs [21]. This work successfully tuned the color of the AgNWs films while maintaining their electrical and optical properties. In our group previous work, we used PEI as a binder to disperse the AgNWs on the porous polyimide sponge, resulting in a high-potential application candidate as a pressure sensor. In this thesis, my research investigates the adsorption of AgNWs on branched PEI, by examining the different spatial arrangements of AgNWs within the 3D porous structure and their resulting effects on the composite properties [22].

2.1.2 POLYSILOXANE

Surface modification by polymers not only allows for precise control of the location and quality of nanomaterial loading but also enables surface multifunctionalization.

Polysiloxane is unique among inorganic and semi-inorganic polymers due to its interesting properties imparted by Si-O alkanes. The Si-O bond length is 1.64 Å, which is greater than the 1.53 Å bond length of C-C in typical organic structures [23]. The oxygen backbone atoms are not bound by side groups, are as small as possible, and have the divalency required for a continuous chain structure. These characteristics contribute to polysiloxane's ultra-high thermal stability, making it suitable as a heat transfer agent and a high-performance elastomer. Additionally, the bonding nature and the chemical

characteristics of typical side groups result in low surface free energy, providing desirable surface properties. Consequently, polysiloxanes are used in mold-release agents, waterproof sprays, and biomedical materials [24–27].

Structural changes in the polysiloxane chain can lead to variations in physical properties, which are of interest to scientists [28]. For instance, the difference in size between substituted Si and unsubstituted O atoms leads to an uneven cross-section of the chain, affecting the chain stacking pattern and explaining the compressibility. The bond angle around the oxygen atom (Si-O-Si is 143° compared to 110° for the usual tetrahedral bonding) also makes the siloxane chain exhibit useful conformational features impacting its applications [29]. Moreover, the sol-gel method can convert silicon-containing materials to polymer-modified ceramics, while pyrolysis can form high-performance fibers [30–33].

For the preparation of polysiloxanes, silicon is first prepared at high temperatures by the reduction reaction of natural silica with carbon. Chlorine gas is then passed to convert silicon directly into tetrachlorosilane, which can be used to form organosilane. Using basic catalysts and higher temperatures helps form high molecular weight linear polymers, whereas acidic catalysts tend to form cyclic small fractions or low molecular weight polymers [34]. Besides hydrolysis, polysiloxanes can also be prepared by ring-opening reactions [35]. Atomic transfer radical polymerization can control the spatial structure of polysiloxanes, and the template method can synthesize ladder-like siloxane structures and explore the placement of silsesquioxane units in the siloxane skeleton [36]. Mixing two siloxane monomers formed during polymerization can result in random copolymers, which are chemically irregular and hardly crystalline. The chemical structure of polysiloxanes affects surface hydrophilicity [37]. Siloxanes with simple aliphatic or aromatic side groups are hydrophobic. One drawback is that polysiloxanes degrade under acidic or alkaline conditions. However, here comes the reversal: If the surface is damaged, the hydrophobic surface can be regenerated by the flexibility of the polysiloxane chain, promoting rearrangement so that hydrophobic groups like methyl can cover the surface again, restoring water repellency. Young-Wook Kim et al. chose fumed silica as the matrix material and reinforced it with polysiloxane-derived silica to improve mechanical strength and thermal conductivity [38]. Zhang et al. controlled the chain length of hydroxyl-terminated polydimethylsiloxane to enhance the insulation and stability of polysiloxane foams. They prepared a series of polydimethylsiloxane foams with different crosslinking densities, observing that changes in cell size and cell density resulted in variations in thermal conductivity through the free movement rate of polysiloxane chains and the crosslinking density of the polysiloxane network [39]. In addition, polysiloxane, which serving as a role in the in-situ bond for the preparation of silica sponges, is an investigated material in the film area. For example, Suo et al. prepared elastomeric siloxanes as thin films by controlling

the degree of hydrolysis and condensation, ensuring that the hydrogels remain non-boiling at high temperatures [40].

It is hypothesized that the integration of polysiloxane with nanomaterials can significantly modify or enhance the properties of nanomaterial-based composites. Therefore, the second part of this thesis focuses on a detailed investigation of this potential application.

2.1.3 POLYVINYLPYRROLIDONE

Referring to the nanomaterials, the incorporation of polymers in the synthesis process enables precise construction of material surfaces, achieving nanometer-level precision control at the molecular scale. This approach is pivotal for achieving desired performance and represents a significant development direction in surface modification techniques.

Among the syntheses of metallic nanomaterials, polyvinylpyrrolidone (PVP) serves as a common stabilizer, dispersant, and soft template. It controls the growth rate and morphology of metal nanoparticles, facilitating the formation of spherical and rod-like shapes [41].

The free radical polymerization of PVP typically utilizes vinylpyrrolidone (VP) monomer as the raw material, with an initiator added to generate free radicals that initiate the polymerization reaction. Commonly used initiators include hydrogen peroxide, diisopropyl peroxide, and dibutyl peroxide. These initiators release free radicals during the reaction, facilitating the polymerization of VP monomers. The free radicals react with the double bonds in VP monomers to form polymer chains. During polymerization, the vinyl groups in VP monomers extend into polymer chains through carbon-carbon bonding connections. This free radical polymerization reaction typically occurs in aqueous solutions due to PVP's good solubility in water. The polar pyrrole ring and vinyl structure within the PVP molecular chain impart a wide range of properties to PVP, including biocompatibility, surface activity, solvency, and complexation abilities [26, 42–44].

Extensive research has been conducted on the influence of PVP on the structural characteristics of nanomaterials synthesized. For instance, Fichthorn et al. used the growth of silver nanocubes mediated by PVP as an example to investigate how directing agents control the shape of nanocrystals [45]. The authors concluded that PVP's shape selectivity in nanomaterials primarily results from enhanced trapping of incoming silver atoms on longer PVP films on Ag(111), increased trapping on wider PVP films on Ag(111), and reduced free energy barriers for silver atom entry onto the surface in lower-density films on Ag(111). Alam et al. prepared icosahedral Au@Ag core-shells by PVP-assisted N,N-dimethylformamide reduction and investigated the crystal structure and growth mechanism of Au/Ag binanocrystals [46]. Wang et al. utilized cytosine-assisted aqueous-

phase synthesis to create AgPt hollow alloy nanostructures, which serve as highly active electrocatalysts for ethylene glycol oxidation and hydrogen evolution [47]. Wang et al. synthesized Pt-Ag alloy octahedral nanocrystals as electrocatalysts for the methanol oxidation reaction in the presence of PVP as a stabilizer [48]. Camargo et al. investigated the catalytic properties of AgPt nanoshells electrochemically, focusing on the effect of size wherein larger outer diameters exhibited superior performance. They also employed silver nanoparticles as hard templates, with PVP serving as a surfactant in the experimental procedure [49]. In the process of preparing alloy catalysts using silver as a template through methods such as electrochemical corrosion, the presence of PVP on the silver surface is often overlooked. Whether the presence of PVP on silver nanowires affects the platinum atom trapping behavior during alloy formation, thereby influencing the utilization efficiency of the platinum precursor, remains unclear. Furthermore, whether the structure of PVP changes during the alloy formation process is an interesting question that could significantly impact the electrocatalytic performance of the final catalyst and the assembly of devices.

Building up on our established AgNWs synthesis technology, we have expanded the application scope of AgNWs. Specifically, we have focused on the influence of PVP on the surface of AgNWs in the formation of PtAg alloys and the subsequent catalyst performance and cell applications. This constitutes the third component of this thesis.

As previously mentioned, surface modification involves altering the surface of a material to meet specific usage requirements. The choice of materials plays a crucial role in this process. In my thesis, my research primarily focuses on porous materials and nanomaterials.

2.2 POROUS MATERIAL

Porous structures are widely encountered in our daily life, such as wooden structures, honeycomb structures, butterfly wings, plant leaves, coral, the reticulated porous bone of whales, and even in the simplest porous marine organisms. Porous materials are characterized by the presence of abundant internal pore structures, whose pore size, shape, porosity, and connectivity can be tuned over a wide range. The introduction of pores significantly enhances the specific surface area and mass transport capability of the materials, while endowing them with distinctive structural features and physicochemical properties. According to the connectivity of the pores, porous materials are generally classified into open-cell and closed-cell structures. In open-cell materials, the pores are interconnected, forming continuous channels throughout the material, which facilitate mass diffusion and transport and improve interfacial utilization efficiency. In contrast, closed-cell materials

possess isolated and enclosed pores, resulting in higher structural stability and mechanical integrity. Therefore, regulating the open- or closed-cell nature and structural characteristics of porous materials enables an effective balance between structural stability and functional performance, thereby broadening their potential applications in areas such as biomaterials, sensing, adsorption, thermal insulation, and catalysis. [50].

From another standpoint, depending on the raw materials utilized, porous materials can be categorized into polymer foams, porous ceramics, and porous metals, each possessing unique properties tailored for specific applications across various fields. These categories will be briefly described below.

2.2.1 POLYMER FOAM

For polymer foam, high molecular weight polymers such as PS, PP, PVC, ABS, PU, phenolic resin, and urea-formaldehyde resin, along with various additives such as glass, calcium carbonate, carbon black, barium sulfate, silicate wood powder, or metal powder, are typically mixed together through a straightforward preparation process to obtain polymer foam for various applications [51–54].

A common preparation method involves the use of supercritical CO_2 as a foaming agent. This method circumvents issues associated with inorganic fillers, which tend to agglomerate and degrade thermal and structural properties when dispersed and sintered within organic materials, resulting in poor performance.

The foaming process for thermoplastic materials presents a complex thermodynamic and kinetic challenge. Depending on the specific foaming technique—whether extrusion foaming, molding foaming, kettle pressure foaming, or injection molding foaming—the process generally involves four fundamental steps: a. Blowing Agent Dissolution: The blowing agent dissolves in the polymer matrix, forming a homogeneous gas-polymer system under specific temperature and pressure conditions; b. Thermodynamic Instability: A sudden pressure drop or temperature rise induces thermodynamic instability, causing the polymer-gas saturated system to become supersaturated. This leads to the formation of tiny bubbles within the polymer melt, initiating bubble nucleation; c. Bubble Nucleus Growth: Gas molecules continue to diffuse into the bubble nuclei, promoting their growth. This phase includes phase separation and a gradual decrease in system free energy; d. Stabilization and Curing: As vesicles stabilize, gas diffusion into the bubbles decreases, halting their growth. The polymer matrix then cures and solidifies, shaping the foam structure. Polymer foaming materials are classified based on the connectivity of their vesicles: open-cell foams, where most vesicles are interconnected, and closed-cell foams, where vesicles are mostly isolated. In applications where foam is exposed to long-

term flammable environments, most polymer porous materials are unsuitable due to their flammability. Porous ceramic materials, however, meet stringent fire safety requirements and are preferred for such applications

2.2.2 POROUS CERAMIC

The chemical properties of ceramic materials are primarily manifested in their high temperature stability, resistance to oxidation, and excellent resistance to acids and alkalis. Ceramic materials are categorized into two main types: oxide ceramics such as Al_2O_3, ZrO_2, MgO, CaO, BeO, and other; Non-oxide ceramics such as carbides, borides, nitrides, and silicides. Materials like silicates, aluminosilicates, diatomite, corundum, and adamantine are commonly used for making porous ceramics. Here, I focus on silicon dioxide (SiO_2) ceramic materials prepared from silicates [55–57].

For porous SiO_2 materials, there are mainly two forms: silica aerogels and silica sponges [58–62]. Silica aerogel, prepared via the sol-gel method, exhibits superb thermal insulation properties. SiO_2, being non-toxic, odorless, and non-polluting, offers excellent temperature and corrosion resistance. The network structure within silica aerogel restricts gas molecule movement due to its fine nanopore size (50 nm), enhancing its thermal insulation efficiency by limiting heat conduction and convection. However, its brittleness is a significant drawback due to weak connections. To address this, silica aerogel is often combined with organic or inorganic materials to form composites. For instance, introducing silica sol into electrospun silica fibers can dramatically improve mechanical properties by enhancing bonding between components. Porous silica materials prepared using the sol-gel method combined with electrospinning technology have been widely studied. For example, research by Ding's group has explored various applications of silica materials [63–70]. They used electrospun SiO_2 nanofibers to create honeycomb structures, incorporating SiO_2 nano-aerogels for improved performance in silica sponge structures. Further advancements include replacing silica gel with aluminum borosilicate to enhance mechanical and fire-resistant properties, using silica-calcium oxide fibers and chitosan for 3D scaffolds in bone regeneration, and employing silica fiber membranes filled with poly(ethylene oxide) for solid-state batteries to achieve high-capacity and long-cycle stability. Additionally, combining silica materials with AgNWs enhances antimicrobial properties, making them suitable for various applications including batteries and biomedical fields. In addition to these applications, SiO_2 finds widespread applications in thermal insulation, exemplified by coating technology and finishing processes utilizing tetraethoxysilane as the precursor, polyimide (PI) powder as a reinforcing agent, and nonwoven melamine foam as the substrate [71–73]. This results in composite fabrics with excellent thermal insulation properties. SiO_2 sponges prepared via electrospun fibers also exhibit a high

density of gas gaps. For cellular monolith structures of porous materials, thermal conductivity is influenced by thermal convection, solid conduction, gas phase conduction, and radiative heat transfer. Thermal convection in cellular frameworks is significantly limited due to air confinement within individual micro-pores. Thermal conduction through the gas phase in pores depends on gas pressure and pore size relative to the mean free path of gas molecules, typically resulting in lower thermal conductivity. Increasing the porosity of ordered porous systems can reduce overall thermal conductivity and improve insulation performance. Based on this principle, structural design, surface modification, and doping of silica fibers are employed to enhance the thermal insulation properties of composite materials. For instance, durable rabbit-like SiO_2/PI composite nanofibers are prepared using simple electrospinning and impregnation processes. These composite nanofibers embed hollow silica microspheres and bamboo-like hollow structures, providing excellent thermal insulation. Additionally, a polyimide thin layer on the surface offers high strength without compromising thermal stability. Moreover, low-dimensional building blocks such as nanowires within lamellar walls introduce sub-micrometer pores, leading to the Smoluchowski effect where pore size matches the free path of gas molecules [74–77]. Multiscale porous scaffolds exhibit superior thermal insulation compared to single-scale materials, providing a promising design for thermal materials.

Apart from thermal insulation applications, composite materials incorporating silica find extensive use in the field of conductivity [78–80]. While pure SiO_2 is an atomic crystal lacking ionic bonds, it becomes conductive when impurities create defects and holes within its structure. Studies in semiconductor domains focus on hydrogen detrapping from SiO_2-Si interface trap centers, variations in interface trap density, hole trapping at SiO_2-Si interfaces, and radiation damage within SiO_2-Si systems, analyzed via positron annihilation spectroscopy. Moreover, The properties of silica can be improved by fabricating composite materials on a silica-based substrate. For example, varying sizes (60 nm, 2 µm, and 25 µm) of SiO_2 particles added to epoxy resin and micron-scale silicon carbide yield composite materials with different nonlinear conductive properties [81]. Larger SiO_2 particles exhibit reduced current density under high field strengths, attributed to the introduction of deep traps by nanoscale SiO_2, contrasting with increased shallow traps in micron-scale SiO_2. Incorporating nanoscale SiO_2 within composites enhances intermolecular interactions due to its smaller size and higher surface area, altering carrier transport within the composite medium. Furthermore, nanofiber-based sponge structures have been utilized in conductive applications. By dispersing AgNWs within a 3D porous sponge structure using a polymer as a binder, their application as pressure sensors has been explored.

In conclusion, SiO_2 stands as a material with exceptional performance, and the preceding sections of this thesis have further investigated advancements based on silica fiber foundations.

2.2.3 POROUS METAL

Metallic porous materials are characterized by numerous directional or randomly distributed pores within the metal, with pore diameters ranging from about 2 micrometers to 3 millimeters. These pores can be categorized based on morphology into independent pore types and continuous cavity types. Among them, porous metal scaffolds, particularly titanium scaffolds, are crucial in biomedical applications aimed at developing implant matrices that facilitate bone tissue in growth, thereby enhancing stability within the body. The porosity and elastic modulus of these porous materials are designed to minimize issues related to stress shielding while facilitating the transport of body fluids to promote bone growth. Additionally, porous metals find significant applications in the energy sector, such as nickel foam-based materials [82–84].

Moreover, porous metallic materials can also exist at the nanoscale, offering great potential for applications in catalysis, a topic that will be further explored in the Nanomaterials section.

2.3 NANOMATERIAL

2.3.1 BACKGROUND ON NANOMATERIAL

Nanomaterials refer to materials where at least one dimension is in the nanoscale range (1-100 nm), or materials composed of these nanoscale units, which are approximately 10-1000 atoms arranged closely together in three-dimensional space. The concept of nanomaterials was first proposed by Richard Feynman in 1959 in his famous lecture "There's Plenty of Room at the Bottom" [85].

At the nanoscale, nanomaterials exhibit discontinuous changes in energy, resulting in novel electronic and band structures. Due to the relatively large surface area per unit volume, nanomaterials possess enhanced chemical reactivity, making them widely applicable in fields such as electrocatalysis. Synthesis of nanomaterials can generally be classified into two categories: top-down and bottom-up approaches [86–88]. The top-down approach involves reducing the size of a bulk material using physical or chemical methods to achieve nanoscale dimensions. The bottom-up approach, on the other hand, involves building up materials from atomic or molecular levels to create materials in the nanoscale range

using physical and chemical methods. Both crystal growth modes can occur in liquid phases, and liquid-phase synthesis is one of the commonly used methods for synthesizing nanomaterials [89]. Numerous empirical rules and reaction systems have been developed, such as mechanisms based on the traditional Lamer model, classical nucleation theory, and oriented attachment mechanism[[90–94]. In addition to the nanometal materials I used, one of the latest research hotspots in the field of nanomaterials is artificial enzymes based on nanomaterials, called nanozymes [95]. They have the advantages of low cost, easy synthesis, high stability, and adjustable activity. Nanozymes are expected to become an alternative and effective choice for therapeutic diagnostics. Back to my nanometal materials, I will introduce the synthesis of nanometal materials in the next section.

2.3.2 SYNTHESIS OF NANOMATERIALS

The synthesis of materials is inseparable from thermodynamics and kinetics. Thermodynamics determines whether a reaction can occur, and kinetics determines the rate and path of the reaction. In the scope of kinetics, I try to understand the rate-controlling steps and their variables in the entire reaction. To meet this requirement, the diffusion process and the formation process of new phases are a process that needs to be understood. For example, in the application of materials, I need to understand the thermal diffusion and electron-transfer processes so that I can better design materials and interpret experimental data. Similarly, in the synthesis process of nanometal materials, I focus on the mass diffusion and the formation process of new phases in the synthesis process of nanomaterials.

Our understanding of the formation of new phases is based on the Lamer model [96–99]. The Lamer model is the basic model of nanocrystal growth, which divides the crystal growth process into three aspects: monomer aggregation, nucleation stage, and growth stage. In the monomer aggregation stage, the monomer concentration increases with the addition of the precursor solution and gradually exceeds the saturation concentration to reach the critical nucleation concentration. When the monomer concentration is greater than the high saturation concentration and lower than the minimum nucleation concentration and the critical nucleation concentration, there is no crystal nucleus and no particles are precipitated, forming molecular aggregates, resulting in an increase in Gibbs free energy. With the increase in free energy, the aggregates formed can be redispersed into a molecular state, and no crystal nucleus is formed. In the nucleation stage, when the monomer concentration exceeds the minimum nucleation concentration, crystal nuclei are generated rapidly and in large quantities. At the same time, the crystal nucleus grows, the concentration of monomer molecules in the solution decreases, and there is always crystal nucleus formation and crystal nucleus growth, even when the reaction rate is 0. The

main obstacle in the nucleation stage comes from the interface energy between the newly formed phase and the liquid phase, and the new phase in free energy. In this process, if we need to obtain uniform and monodispersed nanocrystals, we need to obtain explosive nucleation and slow growth. Scientists can use the method of hot injection, by selecting unstable precursors and using very high nucleation temperatures. After the precursor is injected, the reaction temperature will decrease to inhibit nucleation, allowing the nuclei to enter the growth process to obtain uniform monodisperse particles.

For heterogeneous nucleation, the activation energy required for the reaction can be reduced by adding certain crystal seeds, hard templates, and other ions to the reaction system before nucleation occurs, so that the reaction can be rapidly nucleated (as we used this principle to control the uniformity of the nuclei in our third work). For the newly formed nuclei, it is a thermodynamically stable phase, and the free energy of the system is reduced. In the growth stage, the formation and growth of the nuclei will lead to a decrease in the monomer concentration. The low-concentration monomers diffuse to the surface of the nuclei and continue to grow. The growth process consumes monomer molecules, causing their concentration to further decrease. No new nuclei will be formed unless monomers exceeding the monomer concentration are added. After the formation of the new phase, a phase interface appears. As the crystal grows, the interface area increases, which increases the free energy of the system. When the surface energy of the particle controls the growth of the crystal surface of the particle, it tends to minimize the surface energy of the particle and the particle size tends to be larger. If the particle dynamics dominate, the particle morphology depends on the different growth rates of different crystal faces. In this process, due to the high solubility and surface free energy of small nuclei, small nuclei will sacrifice dissolution during the growth process, while larger nuclei will continue to grow. As time goes on, the average radius of the nuclei increases and the number of nuclei decreases. This process is called Ostwald ripening. In the process of preparing nanomaterials, the drop acceleration of the precursor solution will affect the morphology of the final grains. When the drop acceleration is too slow, the particles obtained after Ostwald ripenning will be uneven in size. When the drop acceleration is too fast, secondary nucleation will occur. The particle size is uneven, and the secondary nucleation phenomenon can be inhibited by adding surfactants or metal chelators.

For homogeneous nucleation, nucleation can be achieved by changing the concentration, temperature, pH value of the reaction system and adding some surfactants or chelating agents. Heterogeneous nucleation is achieved by adding a new phase to the reaction system, thereby reducing the activation energy required for nucleation. At the same time, the surface free energy of each crystal face of the nucleus is different, and the crystal face with low free energy grows first. In order to obtain nanocrystals with uniform size distribution, we control the nucleation time to be shorter relative to the growth time,

and the size of the obtained nanomaterials will be more uniform. The mass diffusion process affects the growth rate of the crystal. If the diffusion rate of monomer ions in the solution is faster, the size of the obtained nanomaterials will be more uneven. In addition to these, the Kirkendall effect can be used to utilize the different diffusion rates of different elements under thermal activation conditions to control atoms to enter the particles of another element to form a pore structure. The growth theory of traditional crystals refers to nucleation phenomena and atom deposition driven by supersaturation as the core processes of crystal growth. The classical theory of crystal growth is based on the Lamer model, characterized by explosive nucleation, diffusion-controlled growth, and Ostwald ripening. This theory effectively explains the growth process of nanocrystals in dilute solutions. In concentrated solutions, nanoparticles may undergo rearrangement or mesoscopic transfer and aggregation with other particles, preferably combining with smaller, unstable crystal nuclei through oriented attachment or mesoscopic connections. During this process, if nanocrystal surfaces are enveloped by certain organic compounds, they can form ordered or disordered mesoporous structures via mesoscopic connections.

Oriented attachment refers to the growth of larger crystals by directly connecting nanocrystals through the same crystal planes. Connections between crystal planes can be achieved through the balanced Brownian motion of nanocrystals in the system (particles moving in a dilute solution) or through the rotational assembly of nanocrystals with dislocation connections to construct interface energy units. The formation of nanowires goes through the process of nucleation-oriented connection-crystallization growth. 0-dimensional grains are formed in the precursor solution reaction system. Based on the small grain size, the interconnection between 0-dimensional grains can form one-dimensional nanowires. In this process, the driving force mainly comes from the dipole-dipole interaction between ligands. The dipole-dipole interaction between ligands is affected by the dielectric constant of the solvent and is inversely proportional to it.

In this entire process of nanowire formation, Ostwald ripening accompanies crystal growth [100–102]. The formation of porous structures in one-dimensional nanomaterials can also be explained by the theory of Ostwald ripening, Kirkendall effect, and oriented attachment. For example, Yu et al. successfully synthesized quasi-2D nanofilms by directional adsorption of 1D nanoparticles on the liquid interface through an interfacial self-assembly inducing interfacial synthesis strategy, effectively realizing anisotropic electrical, thermal, and optical conduction. However, the limitations of crystal orientation and uniformity on the application of ordered films remain to be resolved.

The synthesis of metal nanomaterials can also be classified into solvent thermal methods and template methods [103–106]. Hydrothermal method refers to the synthesis reaction of chemical substances in solution at a certain temperature and pressure. Generally, the reaction is carried out in a high-pressure reactor. Template method is mainly through

the preparation of templates, based on the directional synthesis of templates and the three steps of template removal. In the template method, it is generally divided into soft templating and hard templating. Soft templating refers to the formation of specific shapes of templates under certain conditions, including various ordered aggregates formed by amphiphilic molecules in the reaction, such as LB membranes, microemulsions, and clusters. Hard templating is a rigid template maintained by covalent bonds, and materials with specific morphologies of micro-nano structures are prepared by chemical and electrochemical methods. It can be a porous anodic oxide film.

In the specific experimental procedures, solvent thermal synthesis is a common method used for the synthesis of nanomaterials. Solvent thermal methods for preparing nanomaterials provide an example where nanoparticles tend to aggregate and thus require various methods to transition to a stable state. This includes the addition of organic protecting agents or placement in inert environments containing polymer solutions. Interactions between nanoparticles and these capping groups or solvents counteract Van der Waals Forces or energy barriers within magnetic materials, achieving stable dispersion. For one-dimensional metallic nanowires, the atomic forces between atoms are metallic bonds. Polymer-based one-dimensional nanomaterials exhibit high flexibility due to the low energy barriers for C-C bond rotation within chain segments, allowing them to entangle and produce unique rheological properties. This structural property leads to many complex nanomaterial's structures. Changes in the concentration of nanowire bundles in solution can result in three-dimensional assemblies of irregular pores,ranging from random to ordered to collapsed structures. Alternatively, adding a poor solvent to the existing solution system can form nanowire bundles.

The morphology and structure of nanometals are controlled during this reaction process. Porous nanomaterials, in particular, have received extensive study due to their high surface area and numerous active sites. To achieve a higher surface area, nanomaterials are designed with a hollow structure. "Hollow" means having a hole or empty space inside. It is well known that the properties of materials are mainly determined by their structure. Due to the presence of cavities, hollow structures have a much larger surface area and lower density than solid structures of the same composition and size. Their ultra-large surface area, low density, and high loading capacity give them potential applications in various fields. The template method is also widely used in this thesis experiments for the synthesis of metal nanomaterials. To prepare the structure of nanomaterials with high uniformity and well-controlled morphology in a reproducible, scalable, and cost-effective manner, there are three major synthesis methods: hard templating, soft templating, and self-templating. For hard templating, typically, prepare the hard template first, then cover the shell material on the outer surface of the hard template, and then remove the hard template. In this process, the size and shape of the cavity depend on the size and shape of

the template, while the shell thickness is mainly determined by the coating process. This template can be completely removed or partially retained in the porous material. The key to removing the hard template can be achieved by chemical etching, thermal treatment or calcination, or simply dissolving in a particular solvent. Initially, Caruso and co-workers removed silica templates by adsorbing PS onto the surface of silica particles, then removing silica templates through THF or calcination. Alternatively, Silica spheres prepared by the Stober method can also serve as the basis, and Silica spheres with sizes ranging from 50 nm to 2 μm can be prepared by hydrolyzing alkylsilicates in a water-alcohol mixture in the presence of ammonia solution. Metal materials such as Pd or Sb are functionalized by different polymers such as mercaptopropyltrimethoxysilane or cetyltrimethylammonium bromide-functionalized silica spheres on the surface. The etchant is removed to obtain a hollow structure through 10 M HF or NaOH. The key to removing the template is to use the different stability of chemical etching of internal and external components to obtain a hollow structure.

For soft templating, unlike hard templates, soft templates only exist in the coating process, and it is not necessary to remove the template, but the uniformity of the soft templating method in controlling the morphology of nanomaterials is weak, but it can adjust the internal and external structures of nanomaterials to provide more possibilities and easy to scale up.

For the self-templating method, it can be used to directly synthesize a hollow structure without the need for additional templates. This method is the most suitable for practical applications because of its simple synthesis process, significantly reducing production costs, and ease of scaling up. However, forming a hollow structure requires specific compositions, limiting its applications. In some cases, it can also be referred to as hard templating.

The synthesis of noble metals and their alloys can be classified into hydrophobic and hydrophilic systems based on the reaction solvent. In hydrophobic systems, typically, metal precursors (metal-metallic deep carbonyl compounds, alcohol salts, nitrates, etc.), hydrophobic solvents (toluene, tetrahydrofuran, N,N-dimethylformamide.), surface ligands (oil amines), and morphology regulation (formaldehyde, aniline, benzaldehyde, etc.) are used to achieve reactions under appropriate conditions. The nanomaterials synthesized in hydrophobic systems have advantages such as good dispersibility, rich surface chemistry, and ease of functionalization. Common systems include the toluene-oil amine-formaldehyde synthesis system and the oil amine-octene synthesis system. The octadecyl amine synthesis system, for example, uses silver stearate as a metal precursor to prepare monodisperse silver nanoparticles by heating reaction in a mixed solvent of stearic acid and dodecyl amine, obtaining different sizes of silver nanoparticles at different reaction temperatures, while the nano silver is encapsulated by the long-chain alkyl chain of oil

amine and dodecyl amine. The increasing concentration of samples can also make nano silver self-assemble into oriented rod-like superstructures. In the process of synthesizing alloys, it can be judged whether the alloy can be synthesized in the octadecyl amine system based on the effective electronegativity rule. For the hydrophilic synthesis system, similar to the hydrophobic synthesis system, the four elements are metal precursors (inorganic salts), hydrophilic solvents (water or alcohols), water-soluble surface ligands (polyvinylpyrrolidone or hexadecyltrimethylammonium bromide, etc.), and water-soluble morphology control agents (inorganic small molecules). Based on the PVP-based synthesis system, it can be divided into high boiling point alcohol-benzene derivatives-PVP synthesis system, benzyl alcohol-PVP synthesis system, and PVP synthesis system.

In my first and second works, the synthesis of nanowires was based on the hydrophilic system's hydrothermal synthesis of AgNWs. The platinum-silver nanotubes in the third work were synthesized by the chemical hard templating method in the hydrophobic system.

2.3.3 SILVER NANOWIRES

AgNWs, referred to as one-dimensional silver nanostructures, have diameters ranging from 10 to 200 nm and lengths between 5 to 200 µm. The unique optical properties of metal structures are attributed to their distinctive plasmonic behavior, arising from interactions between light and the loosely bound electrons within the particles. In simple terms, when electromagnetic radiation (light) reaches noble metal nanoparticles with diameters close to or smaller than the wavelength of light, it induces polarization of the conduction electrons of the nanoparticles, leading to charge separation and electron oscillation. When the wavelength of these oscillations matches the wavelength of the incident light, surface plasmon resonance occurs. This resonance, along with surface-enhanced Raman scattering behavior, is influenced by the morphology of metal structures, and characterization of optical properties can be used to determine the structural morphology of AgNWs [107]. For instance, we use UV-Vis spectroscopy to measure the length and diameter of nanowires [108]. Additionally, the crystal surface structure of AgNWs plays an important role in catalytic applications and other fields.

For the synthesis of AgNWs, based on our previous introduction to metallic nanomaterials, we employ the PVP system soft-template method [109–111]. Common surfactants used include cetyltrimethylammonium bromide, polyvinyl alcohol, polyethylene oxide, and hydrophilic block copolymers, which serve as soft templates for the synthesis of AgNWs. However, these templates often suffer from low yield and irregular morphology issues. The polyol method is a highly mature approach for achieving high-yield and high-quality AgNWs. The basic mechanism for the synthesis of nanowires via the polyol method is well understood: silver ions are reduced to silver atoms, and when the concentration of

silver atoms reaches the nucleation threshold, they begin nucleating and growing into nanoparticles. PVP acts as a capping agent adsorbed on the surface of particles, and the presence of Cl ions provides electrostatic stability. With the assistance of the capping agent, particles continue to grow from smaller particles into nanowires. The structure of silver nanowires begins with twinned particles having icosahedral shapes as seeds. The twinned boundaries of these multiplex twinned particles extend outward with fivefold symmetry, and their surfaces consist of ten (111) crystal planes. The twin boundaries have the highest energy on the MTP surface, attracting silver atoms during the Ostwald ripening process. As a result, silver atoms selectively crystallize from the twin boundaries to form multiplex twins along the twin boundaries, producing one-dimensional nanowire structures with five (100) facets on the side.

This reaction primarily involves the heating of metal salt precursors through the polyol reduction method, where PVP serves as a capping agent and prevents nanoparticle aggregation. In this process, the injection rate of the metal salt precursor solution and the molar ratio of PVP to metal salt significantly impact the morphology of nanowires. Regarding temperature, the reduction capability of the system increases with increasing temperature, as ethylene glycol oxidizes to glycolaldehyde. Lower reaction temperatures favor the formation of longer nanowires. Longer reaction times lead to longer nanowires. The effectiveness of PVP is mainly attributed to its nitrogen and oxygen atoms, which adsorb on the surface of silver seeds or particles. For example, a PVP to $AgNO_3$ ratio of 1.5:1 yields nanowires with an aspect ratio of 1000, while ratios of 6:1 yield only short nanowires or nanoparticles. A ratio of 15:1 results in only 20 nm diameter silver nanoparticles, and a ratio of 0.6:1 yields thicker and shorter nanowires [112–114]. The molecular weight of PVP also affects the Ag crystal surface structure. A degree of polymerization of 1 results in irregular shapes and forms of silver nanoparticles, whereas a degree of polymerization of 90 forms rod-shaped nanoparticles. A degree of polymerization of 11,700 forms uniform nanowires. In this study, PVP with a molecular weight of 130,000 and a polymerization of 11,700 were used. Longer chain lengths of PVP yield AgNWs with larger aspect ratios. Keeping other conditions constant, the diameter of nanowires ranges from 142 nm to 290 nm with increasing $AgNO_3$ concentration from 0.1 M to 0.6 M, while their length decreases from 14.3 µm to 7.8 µm. The highest nanowire yield is obtained at 0.1 M, and increasing the concentration of $AgNO_3$ while keeping PVP content constant reduces the PVP-to-$AgNO_3$ ratio, resulting in longer nanowires with smaller diameters. Foreign species can also be used as nucleation agents or seeds to control the final morphology of nanowires. These foreign species can include platinum nanoparticles, silver nanotubes, silver chloride, chloride ions, and bromide ions. Generally, increasing the amount of nucleating agent reduces the diameter of the nanowires produced. In our experiments, the presence of chloride ions can coordinate with silver nuclei, stabilizing

them and preventing their aggregation, promoting anisotropic growth and nanowire formation. Chloride ions also lower the concentration of free cations in the solution, and the formation of silver chloride prevents the accumulation of high concentrations of silver cations and seeds, ensuring gradual release of silver cations during subsequent stages of nanoscale growth. In addition to these influencing factors, factors such as stirring rate, length of stirring rod, and method of adding reactants also affect the final morphology of the product.

The mature fabrication process of AgNWs enables their wide application in various fields, such as biomedicine, conductive sensors, and thermal management applications. Silver, as a highly conductive material, is extensively studied in nanowire form for applications in flexible, stretchable electrodes and pressure sensors [115–117]. Researchers have conducted significant research on the conductivity of silver, for instance, Steffen et al. have adjusted the wet-laid process of nanowires on nonwoven fabrics to ensure uniform distribution, exceeding the critical point for nanowire content, achieving a conductivity of up to 750,000 S/m in polyacrylonitrile nonwoven fabrics, improving it by 7 orders of magnitude, and allowing rapid heating and cooling within minutes under a voltage of 1.1V. The materials also maintain breathability and flexibility without compromising their conductivity [19]. Gao et al. have used PI electrospun nonwoven fabrics and double-sided nonwoven fabrics composed of AgNWs networks to show significant differences in physical, electrical, and thermal properties on both sides, achieving low resistance and superior infrared reflectivity of over 80%, which can be used in smart textiles to evade infrared detection [118]. Alternatively, sandwich-like conductive sponge materials with extremely low resistance have been prepared using nanowire networks sandwiched between two layers of porous electrospun TPU nonwovens, with PCL short fibers acting as glue, providing a strong interface between the three layers to ensure good gas diffusion and low thermal diffusion performance, suitable for integration into smart wearable devices and for collecting body motion signals [119]. Seulah Lee et al. have prepared highly stretchable conductive fibers embedded with silver nanowires and nanoparticles in an elastomeric matrix of styrene-butadiene-styrene through wet spinning, demonstrating the formation of embedded silver nanowires in SBS fibers through the repeated absorption and reduction of silver precursors, forming on the fiber surface and inside nanowires, and the composite fibers exhibit strain-induced strain-sensing functionality, sensing human movement [115]. Li et al. have prepared stretchable conductors by uniformly distributing silver nanowires on the surface of a porous structure, showing sensitive responses to various stimuli such as force/strain and temperature, and can be used for absorbing oils and organic solvents, and other performance [120]. Jiang et al. have prepared 3D sponges with stress-responsive properties, high flexibility, and breathability, with a conductivity of 1.7-166.6 S/cm, which varies with applied stress, reaching the highest temperature during electrical heating depends

on the compression state, opening up new directions for new conductive devices based on this work [25].

AgNWs have high thermal conductivity and are mixed with organic phase change materials, polymer phase materials, etc., to improve the thermal conductivity of materials [121]. Zeng et al. use the high aspect ratio of AgNWs, fewer thermal interface and higher interface thermal conductivity coefficients, allowing organic phase change materials to maintain high enthalpy while improving their thermal conductivity [122]. Han et al. have prepared thermal and electromagnetic shielding composite films with Jannus structure (BNNS/ANF)-(AgNWs/ANF) using solvent-thermal and in-situ growth methods, with the presence of AgNWs giving the film structure insulation on one side and conductivity on the other side, and good temperature-voltage response characteristics [123]. Han et al. have prepared thermal conductive composite films with "fungus tree"-like heterogeneous structure of AgNWs @ boron nitride nanosheets and obtained conductive composite films through self-assembly and hot pressing [124]. Meanwhile, Feng et al. have improved the dispersion and bridging effect of AgNWs by adding GP-DOPO, with high flame-retardant quality and excellent compatibility of GO-DOPO catalyzing carbonization of EP matrix, and further forming a strong protective carbon layer by combining AgNWs and graphene networks to enhance flame retardancy [125]. These materials have wide potential applications in 5G electronic devices.

The aforementioned silica materials can also be applied in thermal management with AgNWs. Chao et al. dispersed uniformly sized silica particles to modify epoxy resin, facilitating the dispersion of AgNWs within the epoxy matrix. The strong interaction between silica particles and silver nanowires effectively mitigates the modulus mismatch issue between rigid AgNWs and the epoxy matrix, while enhancing the material's thermal conductivity [126]. AgNWs are crucial materials widely commercialized for various applications in daily work and life. They are utilized extensively as conductive adhesives, thermal pastes, and are employed on a large scale in flexible foldable devices, transparent LED films, capacitive screens, photovoltaic cells, perovskite solar cells, artificial skin, blood testing, and antibacterial gloves/fabrics, among other fields.

2.3.4 PLATINUM/SILVER NANOTUBES

Platinum/Silver (PtAg) catalysts are among the most effective catalysts for small molecules such as methanol, ethanol, and formic acid [127–129]. However, the scarcity and cost of Pt, along with its CO poisoning effect, have spurred extensive research into Pt-based alloy catalysts and non-Pt catalysts. Typically, Pt-based catalysts incorporate Pt with small amounts of noble metals such as Au, Ag, Cu, Ni, and Co. Among these, silver, renowned

for its excellent electrical conductivity, has garnered significant attention in PtAg alloy material research, aiming to serve as a substitute for Pt catalysts.

PtAg alloys can manifest in various morphologies, including nanoparticles, nanowires, and nanotubes. Song et al. demonstrated the synthesis of Pt-Ag NPs ranging in size from 7.5 to 15.0 nm by varying the amount of chlorinated glucose in the reaction. Leveraging unique size effects, rich surface active sites, and synergistic electronic effects between Pt and Ag, these catalysts exhibit excellent catalytic activity [130]. Furui et al. fabricated PtAgNWs via a template-free, high-pressure autoclave method, leveraging self-catalysis and directed attachment growth mechanisms, achieving lower methanol molecule dissociation adsorption barriers and CO oxidation barriers compared to PtNWs.

Beyond altering PtAg alloy morphologies, researchers have further designed nanostructures with porous characteristics. Elok et al. reduced Pt loading and enhanced Pt utilization by creating porous structures, resulting in high catalytic activity for oxygen reduction reactions, while exploring the influence of porous material diameter on catalytic performance [131]. Electrochemical methods have also been extensively studied for the synthesis of Pt-based nano catalysts, alongside conventional wet chemistry approaches.

In addition to synthesizing pure PtAg nanowires, scientists have explored composite materials by combining PtAg nanowires with other metals or conductive substances like gold or graphene to achieve superior catalyst performance. Ammar et al. employed a simple wet chemical reduction method to deposit highly dispersed PtAg metal alloy catalysts on reduced graphene oxide, varying the atomic ratio of PtAg, thereby enhancing catalyst activity and durability through synergistic PtAg particle interactions and enhanced electron transfer effects of graphene oxide sheets [132]. Liu et al. directly prepared PtAg aerogels with layered porous networks and high porosity, exhibiting highly active catalytic performance in formic acid oxidation [133].

PtAg nanomaterials play a crucial role as catalysts in low-temperature fuel cell devices, driving extensive research efforts [134]. Methods for synthesizing nanomaterial alloys include solvothermal and hard templating methods. Solvent thermal methods involve co-reducing PtAg alloy precursors using chemical methods to synthesize PtAg nanowires of varying compositions, which effectively reduces exposed surface area and minimizes interfacial matching energies, albeit typically requiring high temperature and pressure conditions. Another common approach involves templating, using templates similar to those employed in our previous two works, namely silver nanowires.

The chemical materials utilized throughout this thesis have been introduced. However, the preparation methods of these materials significantly impact their final properties and applications, exemplified by the previously mentioned silica aerogel and silica sponge.

In the subsequent section, we will delve into the key techniques employed for material preparation in this thesis.

2.4 TECHNIQUES

2.4.1 FIBER PREPARATION

Electrospinning is a technology for preparing continuous, nano-scale fiber for a variety of potential applications [135–140]. Electrospinning technology uses a high-voltage electrostatic field to charge the polymer solution or melt to form pendant cone-shaped droplets at the end of the nozzle. When the charge repulsion on the droplet surface exceeds its surface tension, a tiny stream of polymer liquid will be ejected from the droplet surface, it is referred to as a jet. These jets are stretched at high speed by electric field force over a short distance, the solvent evaporates and solidifies, and is finally deposited on the receiving plate. These jets are stretched at high speed by electric field force over a short distance, the solvent evaporates and solidifies, and is finally deposited on the receiving plate (Figure 2.2a). a typical electrospining equipment mainly consist of a high voltage power supply, a liquid supply device and a receiving device. Taylor determined the half angle degree of the Taylor cone when the jet developed to be 49.3 degrees in the 1960s by analyzing the effects of liquid feeding rate, voltage, and distance on the jet stability in the dynamic process of charge-induced splitting of drops with a given viscosity. The jet released from the tip of the Taylor cone had a critical voltage, and its calculation formula was:

$$V_c^2 = \frac{4H^2}{h^2}\left(\ln\frac{2h}{R} - \frac{3}{2}\right)(1.30\,\pi RT)\,(0.09) \tag{2.1}$$

where H is the working distance between the spinneret and the collector, h is the length of the jet, R is the radius of the nozzle, and T is the surface tension of the solution.

Polyvinyl alcohol (PVA) and PVP are widely utilized as spinning aids in the production of fibers [141–143]. The PVA model frequently employed for spinning is designated as 1788, characterized by an alcoholysis degree of 88%. Higher PVA content facilitates ionization, leading to the formation of small aggregates at the needle tips. Consequently, the 1788 model is typically recommended for spinning applications, using a 10% pure PVA aqueous solution. For electrospinning processes, the commonly used PVP model is K90. During electrospinning, suboptimal conditions such as low voltage and high flow rates can result in the formation of droplets. Additionally, overly dilute solutions can cause the appearance of beads on the fibers. To achieve smaller fiber diameters, one can adjust parameters by increasing the voltage, extending the receiving distance, and reducing the solution concentration. In scenarios where fibers adhere to the collection device, employing release

paper can mitigate adhesion issues with nanofibers. Fiber stickiness, which may arise due to factors such as high humidity in the spinning environment, high solvent boiling points, or incomplete solvent evaporation, can be ameliorated by controlling the temperature and humidity within the spinning space.

Apart from single-axis electrospinning, there are also coaxial electrospinning and centrifugal electrospinning [144–148]. One advantage of coaxial electrospinning over single-axis electrospinning is its ability to easily control the internal structure of nanofibers. Nanofiber structures can include hollow fibers, fibers within tubes, nested tubes, fibers within fibers, and porous tubular structures. For instance, in the case of silica fibers, the preparation of simple continuous hollow fibers involves careful adjustment of the injection speed ratio of core-shell solutions based on the viscosity of different solutions. Generally, the outer solution flow rate needs to be higher than the inner solution flow rate to facilitate the formation of a coating structure.

The immiscibility of solvents in the inner and outer layers can form structures such as water-in-oil or oil-in-water, necessary for coaxial fibers. For example, in the preparation of hollow silica fibers, mineral oil serves as the sacrificial inner layer material(Figure 2.2b). After electrospinning, it is removed by soaking in octane solvent or using a similar solvent to achieve well-bonded coaxial fibers. This can be followed by calcination or extraction to remove one of the materials. The difference in needle sharpness between the inner and outer layers needs to be set to a certain length difference to favor the formation of Taylor cones. Coaxial electrospinning allows for the incorporation of various functional materials into the inner or outer spinning solution, resulting in composite materials for different applications. Alternatively, continuous hollow fiber materials can be prepared by combining air flow spinning technology with atomic deposition.

However, for single-axis electrospinning solutions, an excessive amount of spinning aids can lead to lower fiber yield and longer processing times. Moreover, the production rate of coaxial electrospinning technology is relatively lower compared to single-axis electrospinning. To overcome this drawback, improvements have been made in electrospinning technology, such as the centrifugal multispinning system. This system divides the rotating disk into three parts and can produce gram-scale fiber products (Figure 2.2c). It allows for the use of different components, controlling the contact angle and static charge of multi-component nanofiber networks by adjusting the relative amounts of different polymers. The system also offers the possibility to control particle capture efficiency, hydrophilic-hydrophobic properties, and other multifunctional applications by adjusting the components and their distribution in the membrane material.

Nanofibers prepared through electrospinning can be cut into short fibers, which can then be dispersed to serve as the fiber basis for sponge structures. Using short fibers as the

fundamental building units, as opposed to directly using electrospun fibers, facilitates easier storage and transportation, while also reducing the demands on experimental equipment [149]. The porosity of the sponge prepared from silica fibers, which are derived from short fibers produced by electrospinning, is calculated using the following formula:

$$V = \frac{4\pi r^3}{3} + \pi L r^2 \tag{2.2}$$

$$V_{\mathrm{ex}} = \frac{32\pi r^3}{3} + 8\pi L r^2 + \pi (rL)^2 \tag{2.3}$$

$$\Phi_{\mathrm{c}} = \frac{V}{V_{\mathrm{ex}}} \tag{2.4}$$

$$P\ (\%) = \left(1 - \frac{\rho_{\mathrm{SG}}}{\rho_{\mathrm{bulk}}}\right) \times 100 \tag{2.5}$$

Here, Φ_{c}, V_{ex}, V, ρ_{SG}, and ρ_{bulk} are the volume fraction of short fibers, the excluded volume of a short fiber, the bulk volume of a short fiber, the density of the electrospun fiber, and the bulk density of the material for sponge preparation, respectively.

One of the latest research efforts in the field of electrospinning focuses on preparing electrospun polymer fiber membranes semi-embedded with liquid metal particles for the fabrication of stretchable electronic devices. Yan et al. demonstrated that liquid metal particles in the fiber mesh break under pressure, filling the gaps to form conductive areas. They used a circuit pattern stamp to produce circuits with high resolution (50 microns) and stability, which can be used in bioelectric signal monitoring sensors. Additionally, the fiber membrane can be separated into individual components and recycled [150]. You et al. proposed an ion chelation strategy to continuously produce electromagnetic fibers with magnetic liquid metal as the core and elastic polyester as the shell in the room temperature water phase [151]. The material shell is used in conductive stability wires, sensors, drive devices, and electromagnetic shielding fields. Electrospinning technology is also attracting significant attention in the preparation of triboelectric materials. For example, Li et al. used electrospinning technology to prepare PAN/$BaTiO_3$/MXene nanofiber membranes with high piezoelectric properties and photothermal conversion efficiency. By combining these membranes with nickel-copper conductive fabrics, they constructed piezoelectric-triboelectric hybrid nanogenerators with enhanced electrical properties, which can be used in the field of human motion monitoring [152].

With continuous technological advancements and increasing application demands, electrospinning technology is poised for greater breakthroughs and innovations in the future,

benefiting fields such as biomedical sciences, high-performance composite materials, analytical chemistry, soft robotics and beyond.

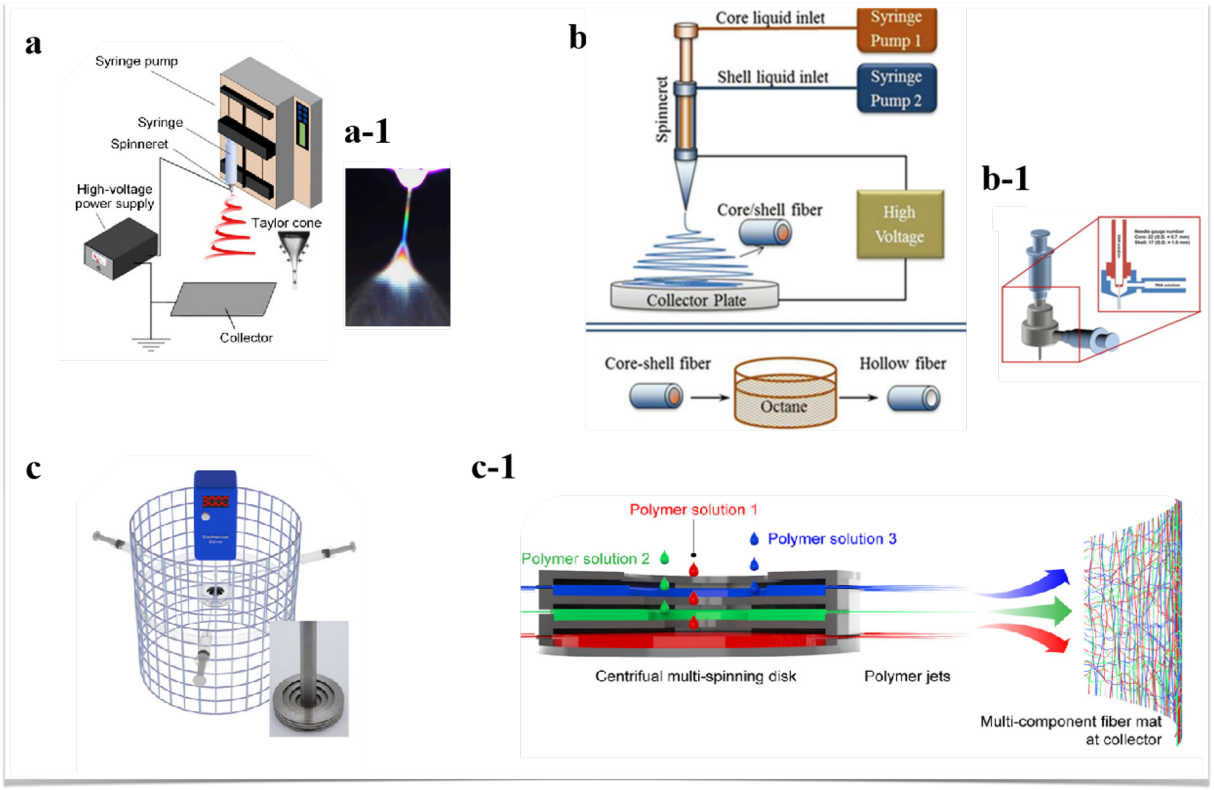

Figure 2.2: a. Schematic diagram of a typical electrospinning device; a-1 image of the straight section of the jet illuminated by white light [153]; Adapted with permission from 153. Copyright © 2024 American Chemical Society. b. Schematic diagram of the setup for coaxial electrospinning and core extraction. b-1.Experimental setup for coaxial electrospinning [154].Copyright from Springer Nature and Copyright Clearance Center. c. Experimental setup and the centrifugal multispinning disk. c-1. Schematic illustration of centrifugal multispinning using three different polymersolutions [155]. Adapted with permission from 155. Copyright © 2024 American Chemical Society.

2.4.2 FREEZE-DRYING TECHNOLOGY

For porous materials, there are several processes for their preparation, including leaching of particles, emulsion templating, phase separation, three-dimensional printing, electrochemistry, and ice-templating technology. In my experiment, I chose the ice-templating technology, also known as freeze-casting or freeze-drying, which creates porous structures through the solidification of a solvent [156–159]. The basic process of freeze-drying involves freezing a solution in a cold bath and then removing the frozen solvent by sublimation under vacuum, followed by densification through post-treatment to form a porous structure.

During the entire experimental process, changes in experimental conditions greatly influence the final structure. By controlling experimental variables, various internal structures

such as lamellar, honeycomb, cellular, and radial can be obtained. The cooling rate of the liquid, the type of solvent, and the sublimation speed can all affect the final material's structure and performance.

The cooling rate is the main factor controlling ice crystal growth and the size of the ice template [157]. Generally, the faster the cooling rate, the smaller the pore size. Besides the cooling rate, the temperature gradient and the presence of additives also control ice growth. By placing samples on a pre-frozen metal plate, a typical cooling rate of 0.1-10℃/min can be achieved, with a rate above 0.5 ℃/min being preferred. Direct freezing in liquid nitrogen can achieve rates as high as 20 ℃/min, but this method might result in a gradient distribution of pore sizes for larger samples. For our fiber and nanowire suspensions, the freeze-drying rate should be controlled between 1-5 ℃/min. The molds,I used, need to be rigid and non-sticky, typically made from PTFE or silica resin. In my experiment, I used transparent silica glass to better observe the segregation at the interface and to easily track the interface position, avoiding a gradient in pore size.

For the suspension solution used to prepare porous materials, the components of solids, suspension media, and additives are fundamental to achieving scaffold structures. Additionally, the nature of these building blocks affects freezing behavior, and surfactants modify interparticle forces, governing force balance as described by equation. When assembling building blocks into three-dimensional structures, surface grafting and functionalization, as well as polymeric additives, are often used as dispersants and binders to form an open network. The pore structure is also influenced by the solvent properties, with water, camphene, camphor-naphthalene, and tert-butyl alcohol imparting lamellar, cellular, dendritic, and prismatic pore morphologies, respectively. The final pore morphologies can be tailored by using ice structuring agents such as ethanol or salt to control crystallization. During the solidification process, factors such as the solidification rate at the two-phase interface, temperature, direction, and additional external force fields can influence scaffold wall thickness. We achieve micro-scale crystallization oriented along the freezing direction and the resulting multi-domain lamellar scaffold structure through unidirectional freezing, which induces arbitrary ice crystal nucleation processes [160, 161]. Alternatively, we control ice crystal growth in vertical and parallel directions using two temperature gradients, resulting in large-scale single-domain (centimeter-level) aligned lamellar structures. By replacing molds and controlling the two temperature gradients, we can obtain highly optimized fluid transport structures for oil-water separation, resembling the cellular tracheal structure in trees. Besides temperature, external magnetic fields, electric fields, acoustic fields, and light also influence the pore structure of porous materials (Figure 2.3). Light, a novel method, drives reactions and rearrangements between polymer structural units under frozen conditions, offering exciting research potential from molecular unit structure design.

Freeze-drying technology can also be combined with other material processing methods, such as electrospinning and electrospraying, to prepare porous materials with special structures.

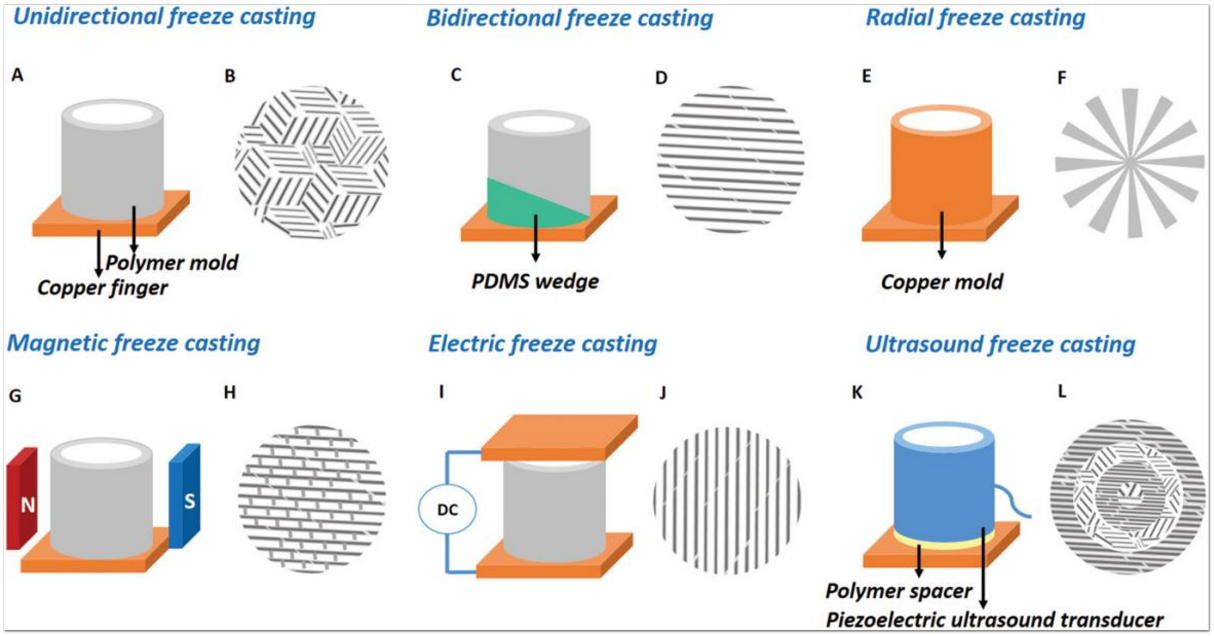

Figure 2.3: Schematics of freeze casting techniques and corresponding top-view microstructures of resulting scaffolds. a-b. unidirectional, c-d. bidirectional, e-f. radial, g-h. magnetic, i-j. electric and k-l. ultrasound freeze casting[154]. Copyright from John Wiley and Sons and Copyright Clearance Center.

The benefits of freeze-drying include a wide range of applicable materials and the ability to influence final pore morphology, porosity, and micro-/macrostructure scaffold geometries through changes in experimental conditions, thereby affecting the composite materials' applications. Existing experimental data on freeze-casting, such as the relationship between volume fraction and porosity, can be found on the FreezeCasting.net website. Besides controlling the final sample morphology through the aforementioned freezing experimental conditions, spray-freezing and directional freezing techniques have been developed to form porous particles and aligned porous materials. There are two methods for solvent removal: ambient pressure drying and freeze-drying. For ambient pressure drying, the wet gel often needs solvent exchange. For instance, if the solvent in the wet gel is water (surface tension $72.75 \times 10^{-3}\,\mathrm{N\,m^{-1}}$), it needs to be immersed in ethanol (surface tension $22.32 \times 10^{-3}\,\mathrm{N\,m^{-1}}$) to replace the water with ethanol, and then similarly, ethanol is replaced with hexane (surface tension $17.89 \times 10^{-3}\,\mathrm{N\,m^{-1}}$), followed by evaporation of hexane. This process reduces the surface tension's destructive effect on the network structure. Although ambient pressure drying is not limited by equipment, it consumes a large amount of solvent and takes a long time for solvent exchange, posing certain limitations for industrial production.

In this section, the fundamentals of freeze-drying and freezing theory are first introduced. Subsequently, the fabrication process based on controlled freezing and freeze-drying for constructing porous structures is discussed. The objective is to elucidate the structural formation mechanisms and to investigate how processing parameters influence the resulting microstructure. Following sample preparation, the thermal and electrical properties of the samples will be systematically evaluated.

2.4.3 EXPLORING THERMAL PROPERTIES IN MATERIALS

For thermal conduction and diffusion measurements, there are two main categories: steady-state techniques and transient techniques.

Before we mentioned about the thermal conductivity, the temperature and heat definition is must to clear to do the thermal research. Temperature is a measurable, standardized thermodynamic function used to characterize the difference in energy of a substance at the atomic level-such as electronic, vibrational, and rotational states-under conditions of local equilibrium. The energy exchange by a particle (atom, molecule, electron) transferring from a region of higher temperature (large thermodynamic energy function) to a region of lower temperature is called heat. Heat transfer from a substance can be conceptualized through conduction, convention, and radiation. Conduction occurs in solids or stationary liquids due to the exchange of energy resulting from temperature differences within the material. The thermal transfer ability of a material is typically measured through the physical quantity known as thermal conductivity. Metallic materials typically exhibit high thermal conductivity compared to other substances. The high thermal conductivity of metals is mainly due to two factors, the electrons and the crystal lattice. Metals have a higher electron conductivity than other materials and have a well-arranged crystal lattice structure. For instance, gold boasts a thermal conductivity of 317 W/mK, while silver surpasses it with 429 W/mK due to the ability of the well-ordered crystal lattice to transmit thermal energy via vibrational quanta called phonons, and copper follows closedly at 400 W/mK. These metals find widespread use in applications such as heat exchangers and heat sinks.

Common glass materials typically have a thermal conductivity range of 0.2 W/mK to 3.0 W/mK. Optical glass can exhibit a thermal conductivity as low as 0.2 W/mK, while laminated glass can reach values as high as 3.0 W/mK. The thermal conductivity of plastic materials varies between 0.2 W/mK and 0.43 W/mK, with ABS plastic at 0.2 W/mK and HDPE at 0.43 W/mK. Rubber has a coefficient of thermal conductivity ranging from 0.01 W/mK to 0.5 W/mK. Additionally, liquid and gaseous materials are utilized in thermal insulation and heating shielding technologies. The thermal conductivity of liquids is generally much lower compared to metal materials, with exceptions such as mercury. For

example, the thermal conductivity of water at 30 degrees celsius is 0.62 W/mK, whereas that of benzene at the same temperature is 0.16 W/mK. Gases are also commonly employed in thermal insulation materials due to their low thermal conductivity, typically between 0.015 W/mK and 0.025 W/mK. Air commonly exhibits a thermal conductivity of 0.026, while krypton and hydrogen have values of 0.0088 W/mK and 0.18 W/mK, respectively. For most pure metals, thermal conductivity decreases with increasing temperature, while for gases, it increases. Generally, the thermal conductivity of insulation materials gradually increases with temperature. At very low temperatures, thermal conductivity decreases linearly due to the dominance of defect carrier scattering.

For homogeneous and isotropic solids, the Flourier's law [162]:

$$q''(\hat{r}, t) = -k\nabla T(\hat{r}, t) \quad (\mathrm{W/m^2}) \tag{2.6}$$

The laws of heat conduction are mainly influenced by the medium as a function of space ($\hat{r}$) and time (t). The formulation of flow of heat is constrained by boundary and initial conditions. Before dealing with the boundary condition, we need to understand radiation (Stefan-Boltzmann) and convection heat transfer (Newton's law of cooling). Heat radiation is the transfer of energy (interconversion between thermal and radiant energy) from electromagnetic waves, and it can propagate in a vacuum. If a material is warmer than the ambient temperature, a significant amount of net energy is transferred from its surface by radiation. The Stefan-Boltzmann law which states that total power radiated per unit area of the surface of a blackbody (the radiance or energy flux density of the object) is proportional to fourth power of the thermodynamic temperature. The Stefan-Boltzmann law is shown below [163]:

$$j^* = \varepsilon\sigma T^4 \tag{2.7}$$

The emissivity of the blackbody (ε) for an ideal blackbody is 1. The scaling factor (σ) is known as the Stefan–Boltzmann constant.

Thermal convection is the process of heat transfer between a solid and a fluid when the fluid flows past the surface of the solid, which has a different temperature. For this phenomenon, we have empirical formulas, often referred to as Newton's law of cooling, which describe the rate at which an object loses heat as being directly proportional to the temperature difference between the object and its surroundings under neglecting surface area and changes in the nature and temperature of the external medium. Specific formulas are shown below.

$$\ln(T - C) = -kt + B, \quad T - C = e^{-kt+B} \tag{2.8}$$

where k is the rate constant, t is the reaction time, and B and C are fitting parameters. For porous materials, the boundary condition we can calculate should belong to the inter-

face boundary condition, where solid-solid contact exists only in a small portion, and most of the space is filled by air. Common boundary conditions include temperature, heat flow rate, heat flow density, convective density, and thermal radiation. Most of these boundary conditions are likely to be nonlinear due to temperature changes. Additionally, the contact conductance of solid-solid contact at the interface can be affected by factors such as surface roughness, interface contact pressure, temperature, thermal conductivities of the contacting solids, and the type of fluid in the gap. Samples with flat surfaces will have lower contact conductivities. To address the variations induced by waviness, we assume that the conservation of energy at boundary surfaces results in no energy accumulation at infinitely thin surface, between the materials to mitigate the adverse effects caused by waviness. For example, in LFA measurement,we spray graphite and PDMS on the surface of sample to minimize the effects of waviness [164]. The contact thermal conductivity decreases as the ambient air pressure decreases because the thermal conductivity of the gases trapped in the interface decreases. Besides thermal conductivity, thermal diffusivity also represents a thermophysical property of the medium. Thermal conductivity is associated with the speed of heat propagation into the solid during temperature changes. It is also affected by the density and specific heat capacity. For the same material, in the absence of phase change and chemical changes under the premise of a certain amount of homogeneous material temperature increase of 1K the amount of heat required is the same, but with the improvement of the porosity of the insulation material or density reduction, the thermal conductivity is reduced, when the density is less than a critical value, the air in the voids began to produce convection, radiant heat conduction is also strengthened accordingly, the material's thermal conductivity will increase instead. This time the thermal conductivity of the material will increase. The relationship between the physical properties of insulation materials is shown below [165–167]:

$$\lambda = \alpha c \rho \tag{2.9}$$

$$\alpha c = \frac{\lambda}{\rho} = \frac{\lambda d}{\rho d} = \frac{d}{\rho R} \tag{2.10}$$

where λ is the thermal conductivity, α is the thermal diffusivity, ρ is the density, c is the specific heat capacity, d is the thickness, and R is defined as the density factor.

For porous sponge materials, the low bulk density and the synergistic interaction between the pore structures lead to desirable barrier properties. Ding et al. designed and synthesized silica nanofiber aerogels with hierarchical honeycomb structure by taking electrospun silica fibers and silica nanoparticle aerogels as the matrix and silica sol as the high temperature nanogel, to obtain silica sponges with ultra-low density and ultra-low thermal conductivity, and adapted to a wide range of temperature changes[35]. they had done a lot of work on the structural design strategy, controlled synthesis and multifunc-

tional application of nanofibers, and explored new application directions such as sound absorption, oil-water seperation, thermal insulation and so on. In our work,the addition of AgNWs led to a decrease in the thermal conductivity of the composite sponges, which could be attributed to the change in the frequency of collisions of molecules with the solid network structure, resulting in a decrease in the thermal conductivity of the material.

2.4.4 ELECTRICAL CONDUCTIVITY

In addition to the mass diffusion process in nanosynthesis and the thermal diffusion process in thermal properties research, which we discussed in our previous introduction, understanding the electrical diffusion process is also crucial for this thesis. In our first work, electrical diffusion refers to the movement of electrons under the influence of electric field forces. In a third work, this concept expands to include the movement of charged particles under the combined influence of electric field (migration) and concentration gradient (diffusion). When the effects of the electric field and diffusion reach equilibrium, the migration driven by the electric field and the diffusion driven by the concentration gradient offset each other, resulting in a stable current. This process is essential for understanding the polarization curve presented in our third study. The polarization curve is influenced by three primary factors: the diffusion of solutes in the solvent, the inherent resistance of the material, and the ability of mass diffusion to keep pace. These factors collectively determine the behavior of the polarization curve, which is a critical aspect of the cell's performance. The fundamental equation describing electrical diffusion is the Nernst-Planck equation, which integrates the effects of electric field-driven migration and concentration gradient-driven diffusion [168–170].

$$J = -D\nabla c + \mu c E \tag{2.11}$$

where J is the flux, D is the diffusion coefficient, ∇c represents the concentration gradient, μ is the mobility, c is the concentration, and E is the electric field strength. n the first work, we ignored the effect of concentration. The electrical conductivity value was tested by Four-Point Probes with homemade molds containing two parallel copper plates (1 mm thickness). Electrical conductivity is calculated using the following formula:

$$R = \rho\frac{L}{S}, \tag{2.12}$$

$$\rho = R\frac{S}{L}, \tag{2.13}$$

$$\sigma = \frac{1}{\rho} = \frac{L}{RS} \tag{2.14}$$

where R is the electrical resistance, ρ is the resistivity, σ is the electrical conductivity, L is the length of the conductor, and S is the cross-sectional area. In the percolation zone, the data is fitted by a power law following the below equation:

$$\sigma = \sigma_0 \left[P - P_0\right]^t \tag{2.15}$$

where σ is the electrical conductivity of the composite, σ_0 is the intrinsic conductivity, P is the porosity, P_0 is the critical porosity, and t is the fitting exponent. For two and three-dimensional networking, the t is 1.1-1.3 and 1.6-2 respectively [170–173]. The porosity value is calculated according to the following formula:

$$\text{vol\%(Ag)} = \frac{V_{\text{Ag}}}{V_{\text{sponge}}} = \frac{\dfrac{m_{\text{Ag}}}{\rho_{\text{Ag}}}}{\dfrac{m_{\text{Ag}}}{\rho_{\text{Ag}}} + \dfrac{m_{\text{SiO}_2}}{\rho_{\text{SiO}_2}}} \tag{2.16}$$

where m_{Ag} and m_{SiO_2} are the masses of silver and silica, respectively, and ρ_{Ag} and ρ_{SiO_2} are their corresponding densities.

2.4.5 DYE ADSORPTION

The increasing use of dyes in various industries, including textiles, paper, and plastics, has led to significant water pollution, necessitating effective methods for dye removal from waste. Dye contamination is present not only in aqueous solutions but also in organic solvents. Porous structured materials are one of the common options used for dye removal [174–176]. The adsorption capacity of dyes on porous structures is a direct performance parameter. To quantify the adsorption of methylene blue (MB), the equilibrium adsorption capacity (qe) was calculated using the following equation:

$$q_e = \frac{V(C_0 - C_e)}{m} \tag{2.17}$$

Here, V (L) is the volume of the MB solution, and m (g) is the mass of the SiO_2 sponge or SiO_2/Ag sponge. C_0 (mg/L) and C_e (mg/L) represent the initial and equilibrium concentrations of the MB solution, respectively. When C_t is used instead of C_e, it denotes the adsorption capacity at time t.For the dye adsorption kinetic equation, the pseudo-first-order and pseudo-second-order were discussed.

$$\ln(q_e - q_t) = \ln q_e - k_1 t \tag{2.18}$$

$$\frac{t}{q_t} = \frac{1}{k_2 q_e^2} + \frac{t}{q_e} \tag{2.19}$$

Where V (L) is the volume of the MB solution, m (g) is the weight of the SiO_2 sponge or Ag/SiO_2 sponge, and q_t ($mg{\cdot}g^{-1}$) is the adsorption capacity at time t. The concentration of the MB solution at the beginning stage is C_0 ($mg{\cdot}L^{-1}$), and at any time t is C_t ($mg{\cdot}L^{-1}$), respectively. The pseudo-first-order and pseudo-second-order rate constants are k_1 (h^{-1}) and k_2 ($g{\cdot}mg^{-1}{\cdot}h^{-1}$), respectively. The adsorption isotherm is used to describe the interaction of MB with sponges. Langmuir and Freundlich models were established below:

Langmuir model:

$$\frac{C_e}{q_e} = \frac{1}{K_l q_m} + \frac{C_e}{q_m} \tag{2.20}$$

Freundlich model:

$$\ln q_e = \ln K_F + \frac{1}{n} \ln C_e \tag{2.21}$$

In this case, the concentration at adsorption equilibrium is C_e ($mg{\cdot}L^{-1}$). The computed theoretical maximum adsorption capacity is q_m ($mg{\cdot}g^{-1}$), and the equilibrium adsorption capacity is denoted by q_e ($mg{\cdot}g^{-1}$). Furthermore, the pertinent equilibrium constants for the Freundlich and Langmuir models are K_F and K_L, respectively. The Freundlich constant related to sorption intensity is represented by n.

2.4.6 CATALYTIC OXIDATION OF METHANOL

To explore the influence of polymers on the precise construction of material surfaces during synthesis and to achieve nanoscale precision control at the molecular level, PtAg nanomaterials were selected as the research focus. By designing an experimental system containing only the PVP polymer, the adsorption behavior of PVP toward Pt atoms was systematically investigated. This study aimed to clarify how PVP regulates the nanotube wall thickness, Pt–Ag bond length, exposed crystalline facets, and ultimately the catalytic performance toward methanol oxidation.

In acidic solution, the desired methanol oxidation reaction (MOR) proceeds through the direct oxidation of methanol to CO_2 via the transfer of six electrons and six protons. However, in practical systems, CO_{ads} species inevitably form as intermediates, which can occupy active sites, deteriorate catalyst performance, and hinder the overall reaction process. Therefore, the rate-limiting step of MOR on Pt-based catalysts lies in the removal of CO_{ads}, which has a decisive effect on MOR activity. During the reaction, CO_{ads} and OH_{ads} species on the Pt surface participate in the Gilman dual-molecule adsorption mechanism (Langmuir–Hinshelwood process), eventually generating CO_2 and H_2O. The adsorption strength of CO_{ads} strongly influences the MOR activity, and effective removal requires sufficient OH_{ads} concentration. However, an excessive amount of OH_{ads} can suppress MOR activity and reduce the overall efficiency of direct methanol fuel cells (DMFCs). Hence,

maintaining an optimal OH_{ads} concentration is crucial to balance catalytic activity and energy efficiency [177–179].

The incorporation of Ag into Pt-based catalysts effectively reduces platinum consumption while introducing synergistic effects that enhance catalytic activity and durability. With the increasing performance requirements for MOR catalysts, new synthetic strategies are needed to enable large-scale, controllable preparation. Meanwhile, the influence of nanostructure on the catalytic performance must be carefully considered. For instance, in nanosheet metal structures, the utilization efficiency of noble metals decreases as the number of atomic layers increases. It has been reported that the optimal thickness of two-dimensional nanosheets should not exceed approximately 14 layers; beyond seven layers, the strain and ligand effects gradually diminish, weakening the catalytic performance.

In this work, I focused on how the residual PVP layer thickness on the metal surface and its interaction with Pt atoms affect the catalytic properties. Interestingly, our results revealed that the solvent content in the PtAg nanomaterial system plays a critical role in catalytic oxidation. The solvent appears to stabilize the nanostructure, and a higher methanol concentration is required to trigger optimal catalytic activity.

Chapter 3

AIM AND CONCEPT

This thesis focuses on the polymer-mediated regulation of AgNW-based materials for electrical, thermal conductivity, dye adsorption, and energy transformation, in which branched polyethylenimine (PEI), polysiloxane, and polyvinylpyrrolidone (PVP) are employed as key functional polymers to achieve controlled interfacial interactions and structural organization. Firstly, the effect of branched PEI concentration on the spatial distribution of AgNWs within composite sponges was systematically examined, revealing that PEI-mediated network regulation directly governs the electrical behavior of the materials. Secondly, the influence of polysiloxane-modified AgNWs and fibers on the conductive pathways and thermal dissipation efficiency and dye adsorption of the composite sponge was explored, further demonstrating the importance of polymer-assisted interfacial engineering. Finally, the role of PVP in tailoring the surface morphology of PtAg nanotubes was investigated, where PVP-directed nanoscale structuring enhanced catalytic performance toward methanol oxidation. This thesis is therefore organized into three corresponding parts, in which the experimental results and underlying mechanisms are presented and discussed in detail.

Proven research has concluded that incorporating conductive AgNWs into low-conductivity polymer sponges can enhance the electrical conductivity of composite sponge materials. However, the distribution of AgNWs within the porous sponge has not been thoroughly studied. It is a reasonable assumption that changes in polymer concentration would impact the distribution behavior of AgNWs within the porous SiO_2 sponge structure, resulting in alterations to electrical conductivity. Therefore, the goal of this part of the work is to delve deeper into how polymer concentration affects the distribution of nanomaterials in a 3D porous material by impregnation method, consequently influencing the electrical conductivity. This exploration aims to provide insights into accurately controlling the electrical conductivity of the porous material.

The second part of this thesis was conducted as a continuation of the first study. In the first work of this thesis, I explored the enhancement of electrical conductivity in porous materials through the incorporation of AgNWs facilitated by PEI. Despite some improvements, the experimental outcomes suggested that the developed material still has significant potential for further enhancement, particularly regarding its mechanical properties. Consequently, in the second work, I integrated AgNWs with short electrospun silica fibers, encapsulated within polysiloxane, to form a three-dimensional porous sponge structure aimed at optimizing the material's overall properties. Building upon the findings from the first work, I conducted a comprehensive investigation into various properties of the composite sponge, including thermal conductivity and dye adsorption capabilities. This research offers valuable insights into the application of polymer-coated AgNWs as fillers in porous materials, highlighting their potential for multifunctional applications.

In the third part of this study, I focused on AgNWs as a basis for the preparation of metal alloys, specifically platinum-silver (PtAg) alloys, which have broad application potential. One approach to synthesizing PtAg alloys is using AgNWs as a template, followed by the deposition of platinum onto the silver surface. From a polymer chemistry perspective, I investigated the role of PVP throughout the alloy preparation process. It has been hypothesized that the concentration of PVP influences the deposition behavior of Pt on the Ag surface, thereby affecting the exposed crystal facets and the formation of crystal structures, ultimately impacting the catalytic activity. Given the high cost and limited availability of Pt, the objective was also to improve Pt utilization efficiency. By assessing the methanol oxidation performance of the alloy, it has been determined the optimal range of PVP concentration for enhancing catalytic efficiency. This work provides a reference for the synthesis of PtAg catalysts using AgNWs templates, based on my investigation of the effect of PVP content on alloy structure.

Chapter 4

RESULTS AND DISCUSSION

4.1 POLYETHYLENEIMINE CONTROLLED IMPREGNATION OF SILVER NANOWIRES ON ELECTROSPUN SiO_2 SPONGES

This study aims to investigate the influence of polyethylenimine (PEI) concentration on the distribution of AgNWs within SiO_2 sponges and its impact on electrical conductivity. AgNWs possess very high electrical conductivity and are often used as fillers to prepare composite materials in order to enhance their electrical conductivity. Based on the excellent electrical conductivity of silver, AgNWs were incorporated into the impregnation process to enhance the conductivity of the originally poorly conductive silica sponges. In this system, PEI functions as a key dispersant to ensure homogeneous distribution of nanowires within the composite structure. The interaction between the functional groups of PEI and the AgNWs governs the macroscopic dispersion state of the nanomaterials, and consequently determines the final properties of the composite sponge. It has been reported that dispersing AgNWs into polyimide (PI) sponges results in composite sponges with electrical conductivity that changes as a function of the compression ratio [180]. However, these studies did not investigate how polymer concentration affects the distribution morphology of AgNWs. In this study, the concentration of PEI is proposed to regulate the spatial dispersion of AgNWs within the three-dimensional framework. Therefore, the influence of PEI concentration on AgNWs distribution in electrospun sponges and the resulting electrical conductivity of the composite materials was systematically examined. AgNWs and silica fibers were synthesized and characterized, and the modulation of conductivity was analyzed in relation to the morphology of AgNWs distribution under different PEI concentrations.

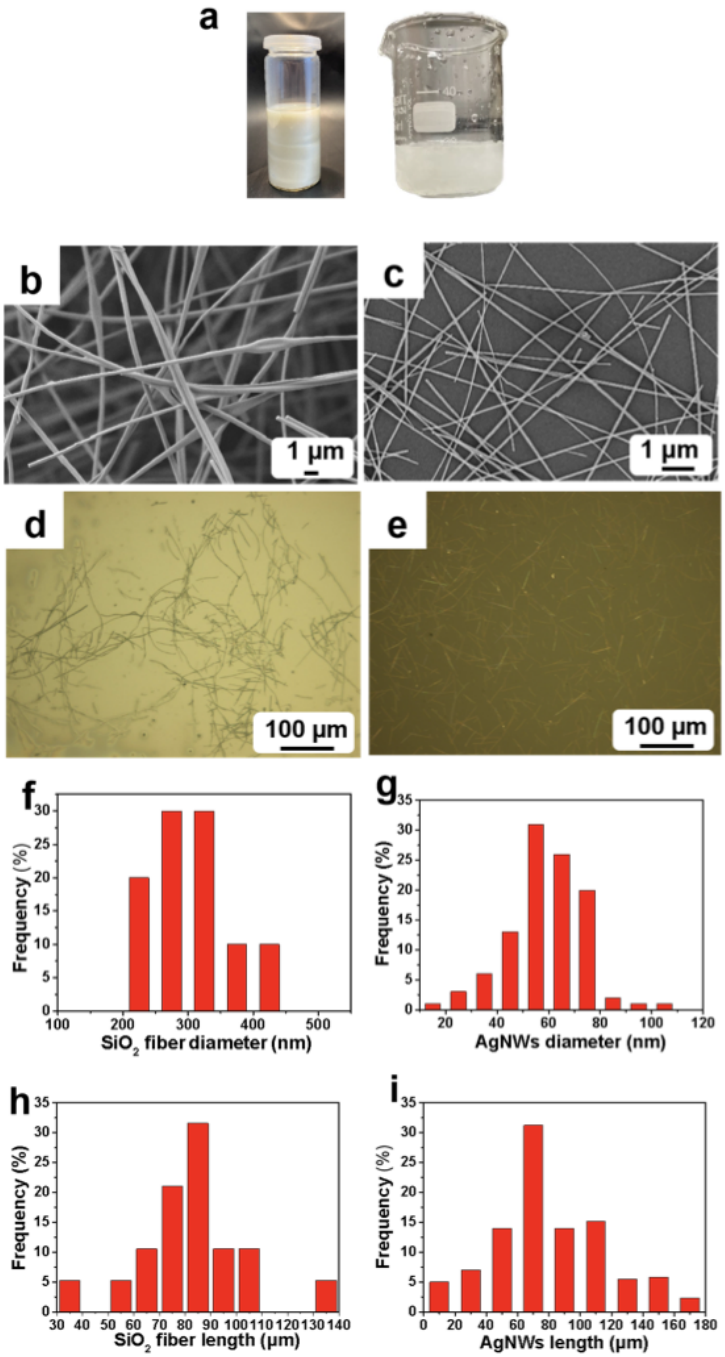

Figure 4.1: Basic physical information of AgNWs and SiO_2 fibers. a. Optical photographs showing metallic-luster AgNWs dispersed in water and SiO_2 fibrous membranes cut into short fibers by ultrasonication. b. SEM image showing that the diameters of SiO_2 fibers are mainly distributed in the range of 200–350 nm. c. SEM image showing that the diameters of AgNWs are mainly distributed in the range of 50–80 nm. d. Optical microscope image of SiO_2 fibers with lengths mainly distributed in the range of 70–90 μm. e. Optical microscope image of AgNWs with lengths mainly distributed in the range of 60–120 μm. f. Histogram of SiO_2 fiber diameter distribution. g. Histogram of AgNWs diameter distribution. h. Histogram of SiO_2 fiber length distribution. i. Histogram of AgNWs length distribution.

4.1.1 PREPARATION OF AgNWs, SIO_2 SPONGE AND COMPOSITE SPONGES

AgNWs are synthesized in solution via the polyol method, which operates under a soft-template mechanism. In this process, elemental silver atoms are generated through the reduction of $AgNO_3$. When the concentration of silver atoms exceeds the supersaturation threshold, nucleation is initiated, resulting in the formation and subsequent growth of nanoparticles. Both twinned and single-crystalline silver seeds can form during the homogeneous nucleation stage; however, twinned seeds are thermodynamically favored due to their relatively lower surface energies.

Aggregation of the initially formed nanoparticles is effectively suppressed. This stabilization arises from multiple mechanisms: (i) PVP macromolecules adsorb onto particle surfaces, serving as capping agents; (ii) chloride ions contribute additional electrostatic stabilization; and (iii) the reduction rate influences the dynamic balance between particle growth and coalescence. During the reflux stage, Ostwald ripening causes larger particles to grow at the expense of smaller ones. These enlarged silver seeds are subsequently guided by PVP to grow anisotropically, first forming nanorods and then extending into nanowires.

Throughout this process, PVP plays a decisive role in directing AgNW morphology. The strong affinity of PVP, derived from its oxygen and nitrogen functional groups, enables selective adsorption on the {100} facets of silver seeds, thereby promoting growth along the {111} direction. PVP preferentially adsorbs on the {100} facets rather than the {111} facets because the {100} facets have higher surface energy and more undercoordinated surface atoms, which enables stronger coordination between the carbonyl groups of PVP and metal atoms. The degree of polymerization of PVP influences the final wire geometry; higher molecular weights facilitate the formation of AgNWs with higher aspect ratios. Moreover, mixtures of PVP with different molecular weights can enhance selective passivation, thereby reducing wire diameter. The concentration of $AgNO_3$ also affects the nanowire dimensions, with higher precursor concentrations producing thicker nanowires. Additionally, chloride ions regulate the population of free Ag^+ ions, assist in stabilizing intermediate nuclei, and promote anisotropic crystal growth, collectively facilitating nanowire formation. Temperature serves as another key parameter, as elevated reaction temperatures generally lead to increased nanowire diameters. The representation of the performance of the AgNWs used in this experiment is shown in Figure 4.2.

In this chapter, silica sponges are prepared via a combination of electrospinning and the sol–gel method at room temperature. In this process, electrospun silica fiber membranes are first cut into short fibers and then ultrasonically dispersed in water, followed by impregnation into a silica sol. The resulting composite precursor undergoes gelation

and is subsequently freeze-dried to obtain porous silica sponges. During freeze-drying, ice crystals sublimate and leave behind interconnected cellular pores (20–500 µm). The pore size can be controlled by regulating ice crystal growth, such as by lowering the freezing temperature to reduce ice crystal dimensions, increasing the fiber concentration, or introducing ice crystal growth inhibitors.

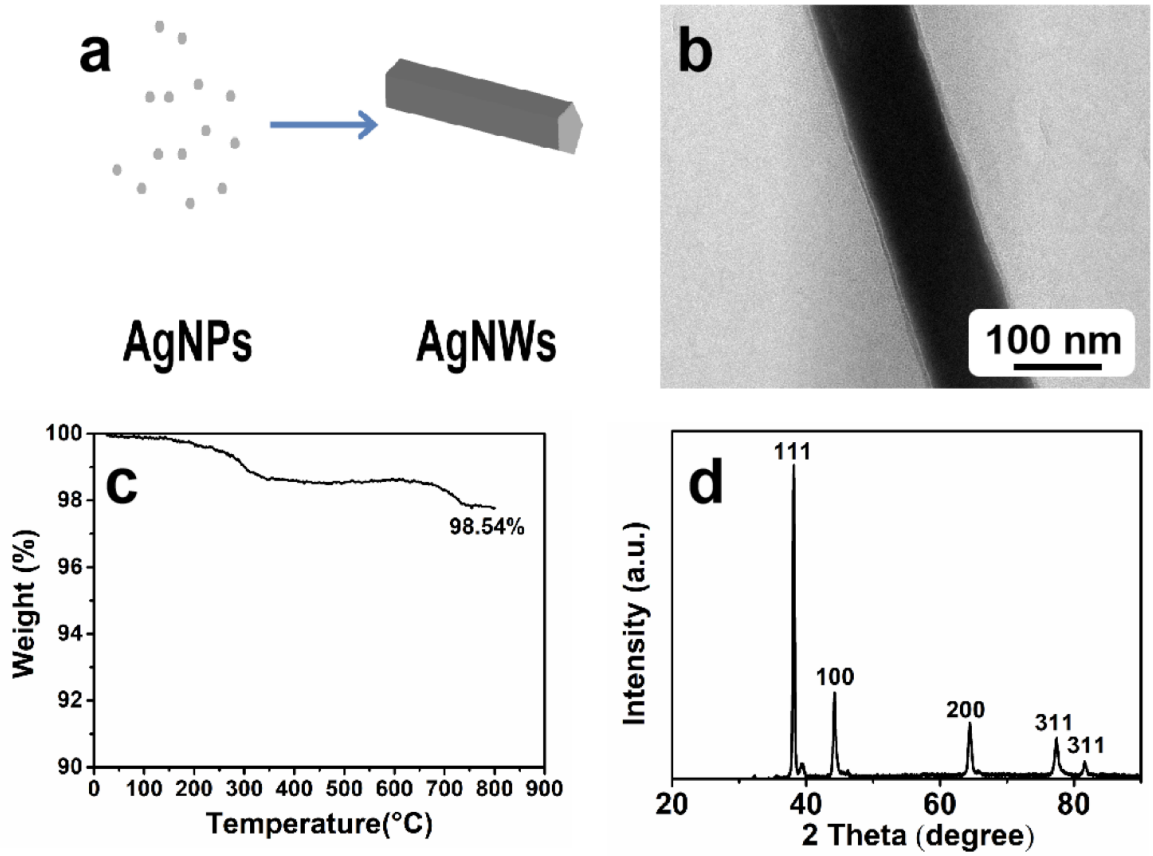

Figure 4.2: a. Schematic diagram illustrating the straightforward formation process of AgNWs. b. TEM image showcasing a singular AgNW. c. Thermal weight loss curve depicting the characteristics of AgNWs. d. XRD analysis presenting the distribution of the crystalline surface structure in AgNWs.

Additionally, within the sponge walls, a secondary pore structure (1–5 µm) is formed due to the packing and rearrangement of fibers during the ice crystal growth process. This finer pore network can be tuned by adjusting the fiber diameter and fiber concentration. After sublimation, the intertwined fibers form the structural walls of the sponge cavities. The nanoscale SiO_2 skeleton, elastic fibrous support framework, and hierarchical porous network collectively endow the material with excellent mechanical resilience and thermal insulation properties.

SiO_2 is an atomic crystal composed of covalently bonded silicon and oxygen atoms, without ionic or metallic bonding, rendering it intrinsically non-conductive. This characteristic is particularly advantageous for the subsequent experiments in this work, as it enables the systematic investigation of how PEI concentration influences the electrical conduc-

tivity of the composite, without interference from the silica scaffold itself. The following details the basic properties of the silica sponge utilized in the course of this experiment (Figure 4.3.).

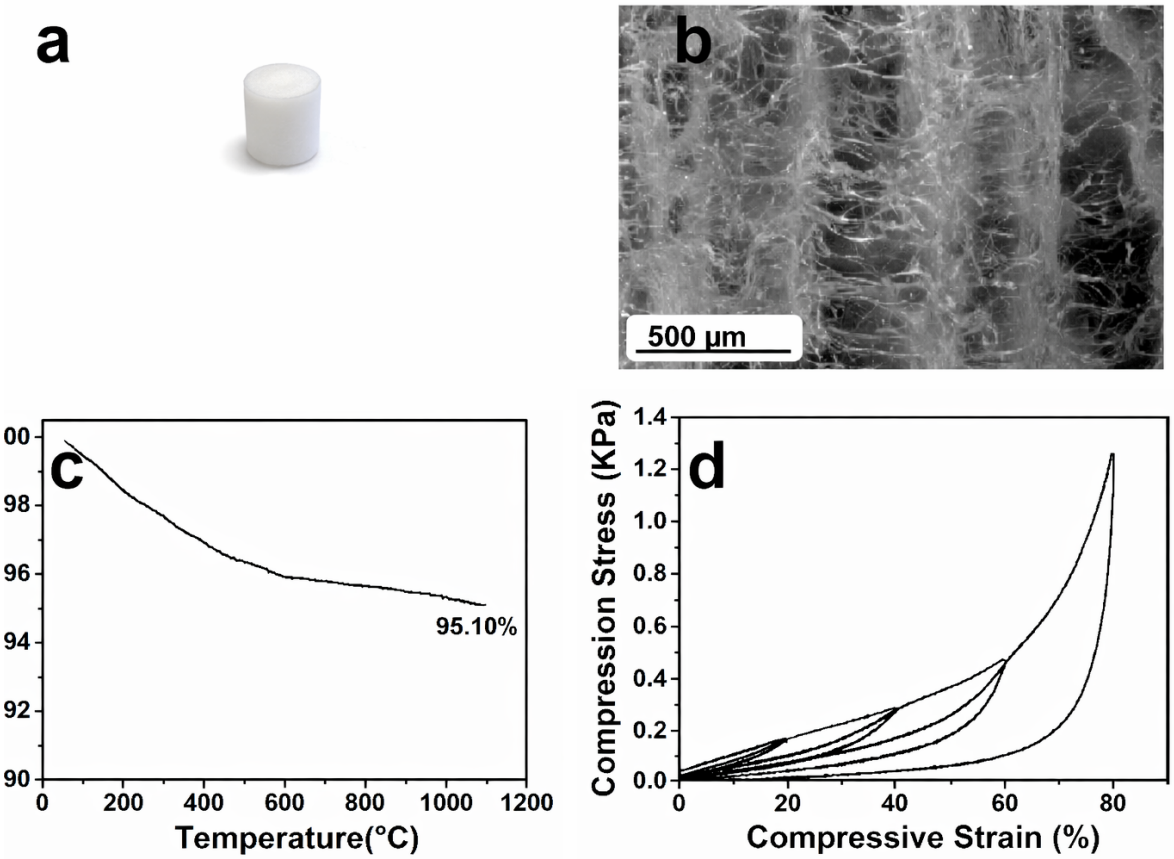

Figure 4.3: Characterization of SiO_2 sponge properties. a. Optical photograph of the SiO_2 sponge placed on filter paper, showing its white appearance. b. Cross-sectional optical microscope image illustrating the internal layered structure of the SiO_2 sponge, where the layers are supported by interconnected fibers. c. TGA curve of the SiO_2 sponge demonstrating its thermal stability. d. Compression stress–strain test showing the excellent compressive resilience of the SiO_2 sponge.

The thermogravimetric analysis (TGA) curve of the SiO_2 fiber sponge exhibits a total weight loss of approximately 4.9%, with a final residue of 95.10%, indicating thermal stability of the silica framework. The initial weight loss at low temperatures is attributed to the removal of physically adsorbed water and residual solvent trapped within the porous structure of the sponge. The subsequent weight loss observed in the intermediate temperature range is mainly associated with the thermal decomposition and oxidation of residual organic species originating from the sol–gel process, such as ethoxy groups remaining from the incomplete hydrolysis and condensation of tetraethyl orthosilicate (TEOS). At higher temperatures, the gradual weight loss can be ascribed to the dehydroxylation of surface silanol groups (Si–OH), which condense to form Si–O–Si bonds accompanied by the release of water. Overall, the limited mass loss and high residual weight confirm the thermal

stability of the SiO_2 fiber sponge. AgNWs@PEI_x@SiO_2 composite sponges were obtained through the wet impregnation method, wherein silica sponges were immersed in PEI solutions of varying concentrations and silver nanowire solutions of identical concentrations.

4.1.2 DISPERSION BEHAVIOR STUDY OF PEI TO CONTROLLING AGNWS ON THE POROUS SIO_2 SPONGE

To investigate the distribution of PEI within the SiO_2 sponge, Congo Red dye was employed as a visual indicator. Congo Red, an anionic amino naphthalene sulfonic dye, undergoes electrostatic interactions with PEI, a cationic polyamine, thereby enabling qualitative visualization of PEI through color contrast. The sponges were soaked in Congo Red solutions containing different concentrations of PEI and subsequently freeze-dried. Optical microscopy with a coaxial light source was then used to observe the resulting color variations. The pure SiO_2 sponge fibers appear white (Figure 4.4a). After immersion in Congo Red solution without PEI, the sponge exhibits a light gray coloration (Figure 4.4b). In the presence of PEI, the fibers turn red owing to electrostatic adsorption of the dye. Moreover, the intensity of the red coloration increases progressively with increasing PEI concentration, indicating higher levels of Congo Red uptake (Figure 4.4c–4.4f). These observations clearly demonstrate that the dye affinity of the PEI-modified SiO_2 sponge increases with increasing PEI content. The intensified red coloration directly reflects strengthened electrostatic interactions between Congo Red and PEI, confirming progressively greater incorporation of PEI into the sponge framework at higher PEI concentrations. This graded PEI distribution is expected to subsequently influence the anchoring, dispersion, and network formation of AgNWs within the composite system.

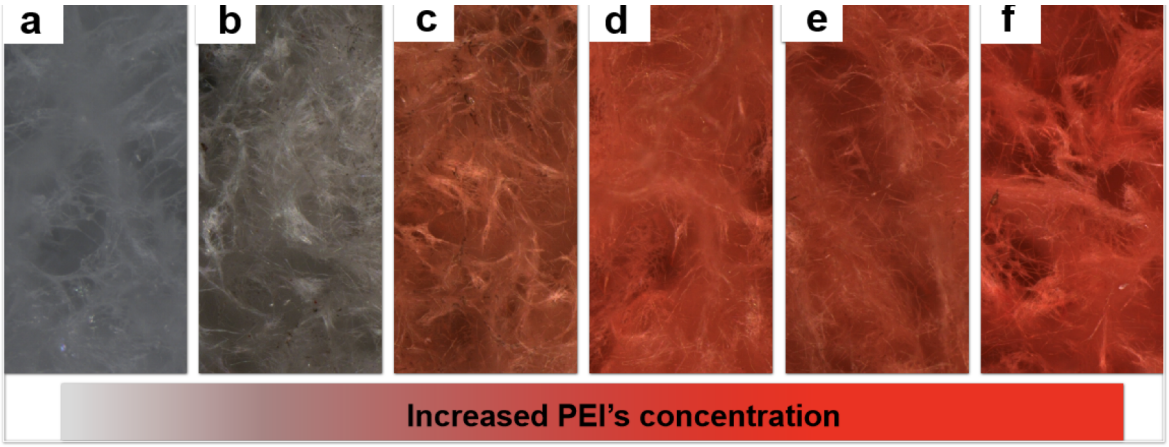

Figure 4.4: SiO_2 sponge fiber colors. a. Pure SiO_2 sponge. b. Dye@SiO_2 sponge. c–f. dye@PEI@SiO_2 sponges with different PEI concentrations (0.5, 1.0, 1.5, and 2.0 g/L), showing a progressively deepened red coloration as the PEI concentration increases.

Contact-angle-based wettability measurements confirm that PEI is uniformly distributed throughout the SiO_2 sponge network. Notably, the introduction of PEI does not alter the intrinsic hydrophilicity of the sponge (Figure 4.5), thereby ensuring effective interfacial compatibility with AgNWs dispersed in aqueous media. In addition, Raman spectroscopy was performed to further verify the presence and successful incorporation of PEI within the SiO_2 framework.

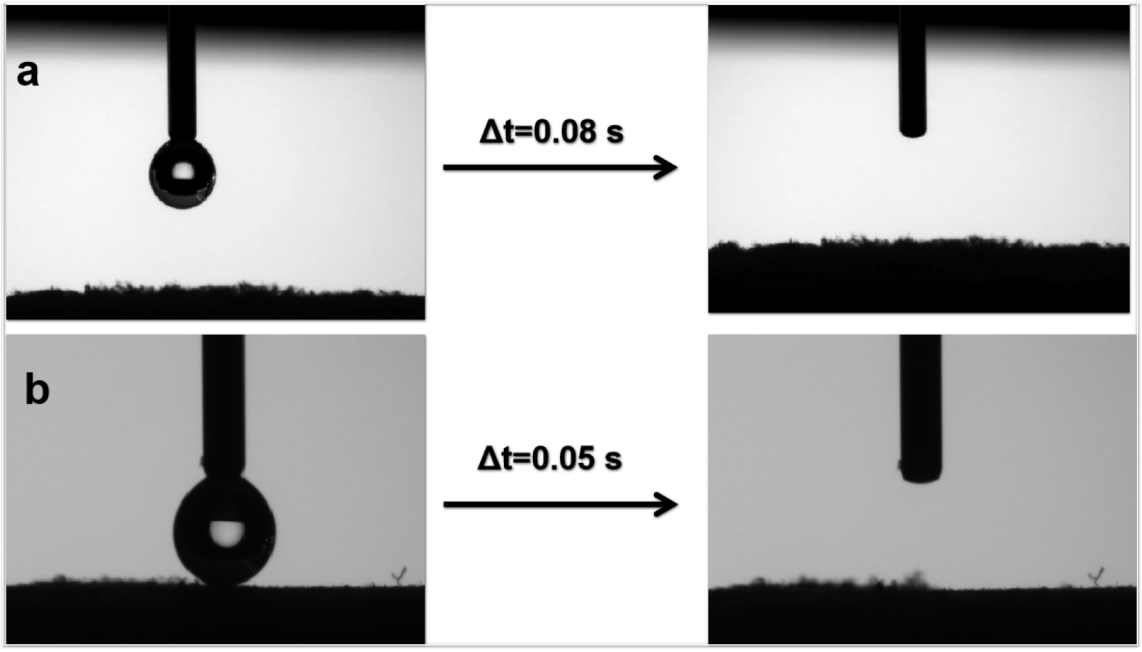

Figure 4.5: a. SiO_2 sponge. b. AgNWs@PEI_1@SiO_2 sponge contact angle, showing that the hydrophilicity of the sponge remains unchanged after PEI modification.

The Raman spectra of the PEI@SiO_2 sponges with different PEI concentrations are shown in Figure 4.6. In the Raman spectrum of the pure SiO_2 sponge, the dominant band at 496 cm^{-1} corresponds to the characteristic vibration of SiO_2. Upon PEI modification, several additional peaks appear. The peak at 1457 cm^{-1} is assigned to the $–CH_2–$ stretching vibration. The peak at 1117 cm^{-1} corresponds to the C–N stretching mode in the $–CH_2–NH–CH_2–$ group, while the peak at 1047 cm^{-1} is attributed to the C–N stretching vibration in the $–N(CH_2)_3–$ group. The peak at 875 cm^{-1} arises from the out-of-plane bending vibration of the N–H bond in the $–CNH_2$ group, and the peak at 784 cm^{-1} is associated with the skeletal rocking vibration of the C–C bond in the $–(CH_2)_n–$ chain.

The presence of these characteristic PEI vibrational bands confirms the successful incorporation of PEI on the surface of the SiO_2 sponge. Moreover, Raman spectroscopy enables semi-quantitative assessment of PEI content. A comparison of samples prepared with 0.5 g/L and 2 g/L PEI solutions shows significantly increased peak intensities at higher PEI concentration, indicating that PEI content on the SiO_2 surface increases proportionally with the concentration of PEI used during modification.

Having verified the distribution of PEI through both qualitative (colorimetric) and semi-quantitative (Raman) analyses, the next step is to examine the distribution and spatial organization of AgNWs within the composite sponge network.

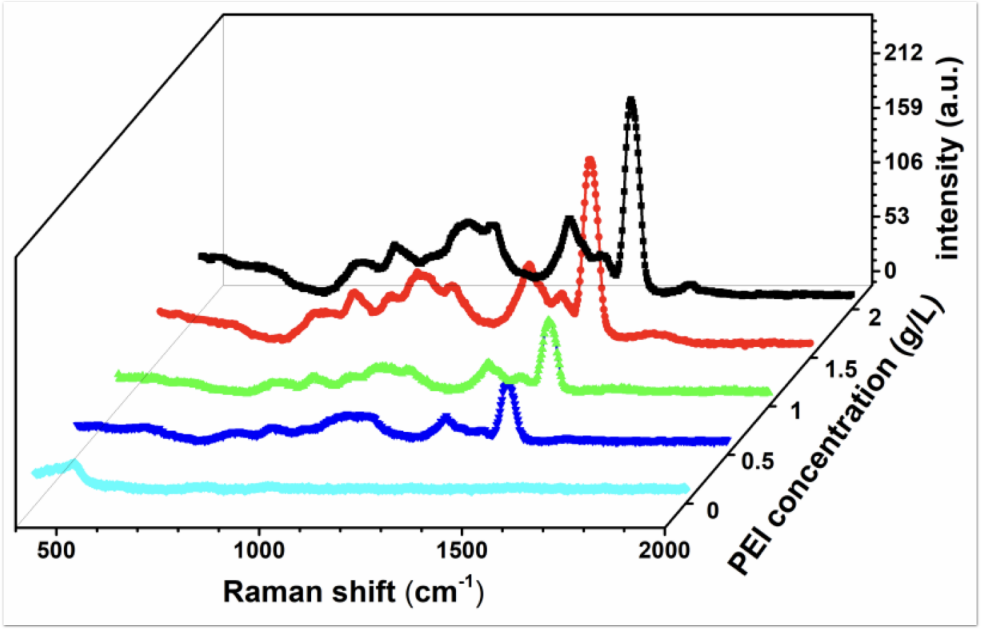

Figure 4.6: Raman spectra of PEI@SiO_2 sponges with different PEI concentrations, confirming the successful adsorption of PEI on the SiO_2 fiber surfaces and demonstrating that the amount of PEI adsorbed increases with increasing PEI concentration.

The distribution of AgNWs within the SiO_2 sponge was examined using backscattered electron (BSE) imaging, where brightness contrast arises from differences in atomic number. Owing to the higher atomic number of silver relative to silicon and oxygen, AgNWs appear as bright regions in the BSE images (Figure 4.7b–f). For reference, the pure SiO_2 sponge (Figure 4.7a) exhibits a three-dimensional porous network composed of stacked microfiber layers, characterized by relatively large interlayer pores and smaller intralayer gaps among the SiO_2 fibers.

In the AgNWs@PEI_0@SiO_2 sponge (Figure 4.7b), only a small amount of AgNWs is deposited on the fiber surfaces, and some fibers remain uncoated, indicating limited adsorption in the absence of PEI. In the AgNWs@$PEI_{0.5}$@SiO_2 sponge (Figure 4.7c), the amount of AgNWs increases and the fibers are more uniformly decorated. When the PEI concentration reaches 1.0, 1.5, and 2.0 g/L (Figure 4.7d–f), the AgNWs gradually interconnect across the three-dimensional SiO_2 framework to form a secondary conductive network, resulting in a double-network structure comprising the original SiO_2 scaffold and the AgNWs network. With increasing PEI concentration, the AgNW network becomes denser, the effective pore size of the newly formed conductive network decreases, and more of the SiO_2 fiber surface becomes covered.

These results indicate that PEI promotes both the adsorption and spatial dispersion of AgNWs along the sponge framework, enhancing network continuity. A higher PEI concentration leads to greater AgNW loading and a higher density of conductive pathways. To further evaluate the spatial distribution of AgNWs, energy-dispersive X-ray spectroscopy (EDS) was conducted to analyze Ag content at different locations within the sponge.

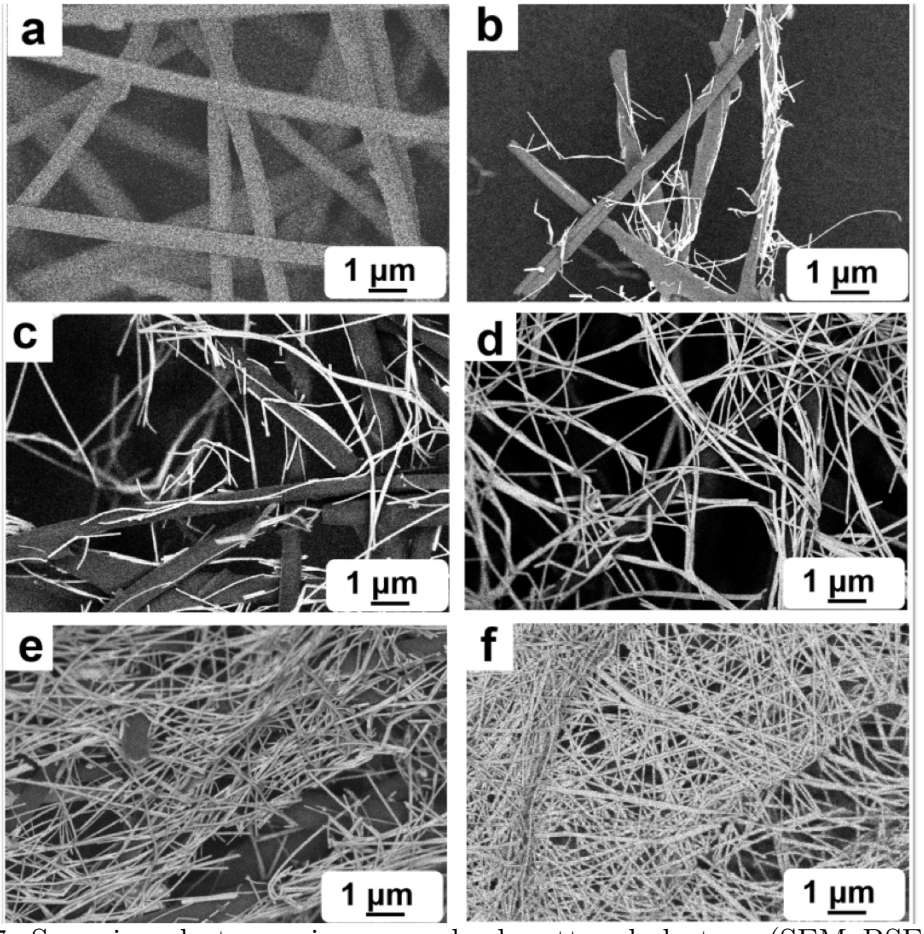

Figure 4.7: Scanning electron microscopy–backscattered electron (SEM–BSE) images of sponges: a. pure SiO_2 sponge. b. AgNWs@SiO_2 sponge. c–f. AgNWs@PEI@SiO_2 sponges with different PEI concentrations (0.5, 1.0, 1.5, and 2.0 g/L), demonstrating that both the adsorption amount and distribution density of AgNWs within the SiO_2 fiber network increase with increasing PEI concentration.

To evaluate the internal distribution of AgNWs, EDX analysis was performed at three representative locations within the composite sponge: the top, middle, and bottom regions. Figures 4.8a, 4.8f, and 4.8h show the SEM images corresponding to the top, middle, and bottom layers of the sponge, respectively. Figures 4.8b–4.8e present the elemental mapping of Si, O, Ag, and their composite overlay for the top region. The Ag elemental distributions at the middle and bottom regions are shown in Figures 4.8g and 4.8i.

A comparison of the Ag mapping (Figure 4.8d, 4.8g, and 4.8i) indicates that the AgNW content in the middle region is significantly higher than in the top or bottom regions.

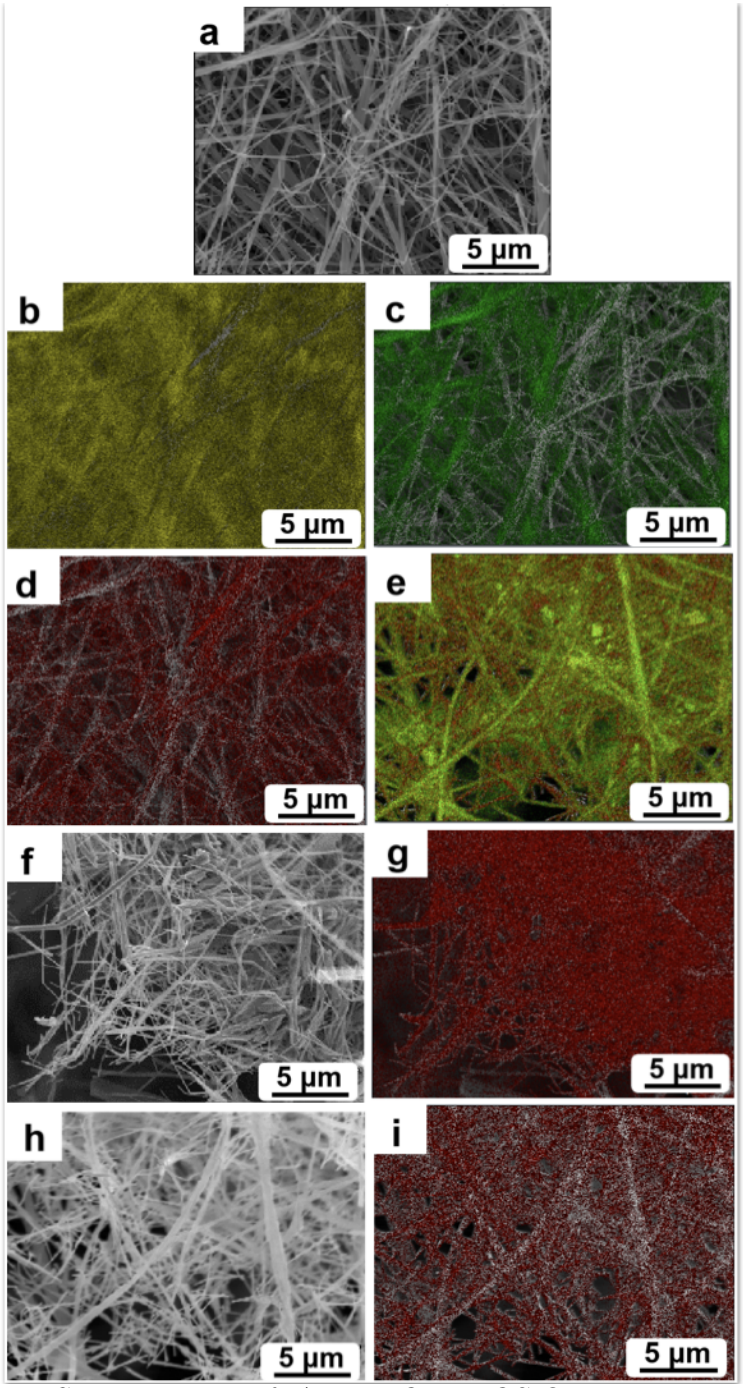

Figure 4.8: a–e. SEM images of AgNWs@PEI_1@SiO_2 sponge in the top position and corresponding element mappings (Si, O, Ag, and overlay). f–g. SEM images of AgNWs@PEI_1@SiO_2 sponge in the middle position and Ag element mapping. h–i. SEM images of AgNWs@PEI_1@SiO_2 sponge in the bottom position and Ag element mapping, showing the dispersion of AgNWs within the three-dimensional SiO_2 sponge.

This observation is further supported by quantitative EDX analysis (Figure 4.9), in which the Ag content (wt%) at the top and bottom surfaces is 53.5% and 53.8%, respectively, while the middle region exhibits a substantially higher value of 88.2%.

This distribution pattern corresponds to a sandwich-like AgNW concentration profile within the SiO_2 sponge, where AgNWs are more densely concentrated in the internal layers than at the surfaces. Such spatial variation in AgNW loading directly influences the formation and continuity of conductive pathways, thereby impacting the electrical conductivity and overall functional performance of the composite sponge.

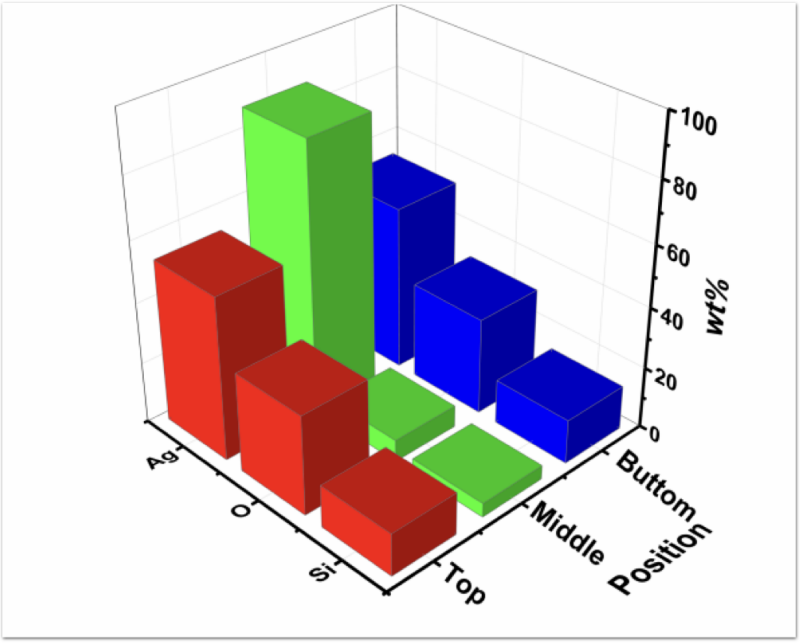

Figure 4.9: the quantitative amounts (wt%) of the elements Si, O, and Ag from corresponding EDS spectra.

4.1.3 CHARACTERIZATION OF THE COMPOSITE SPONGE

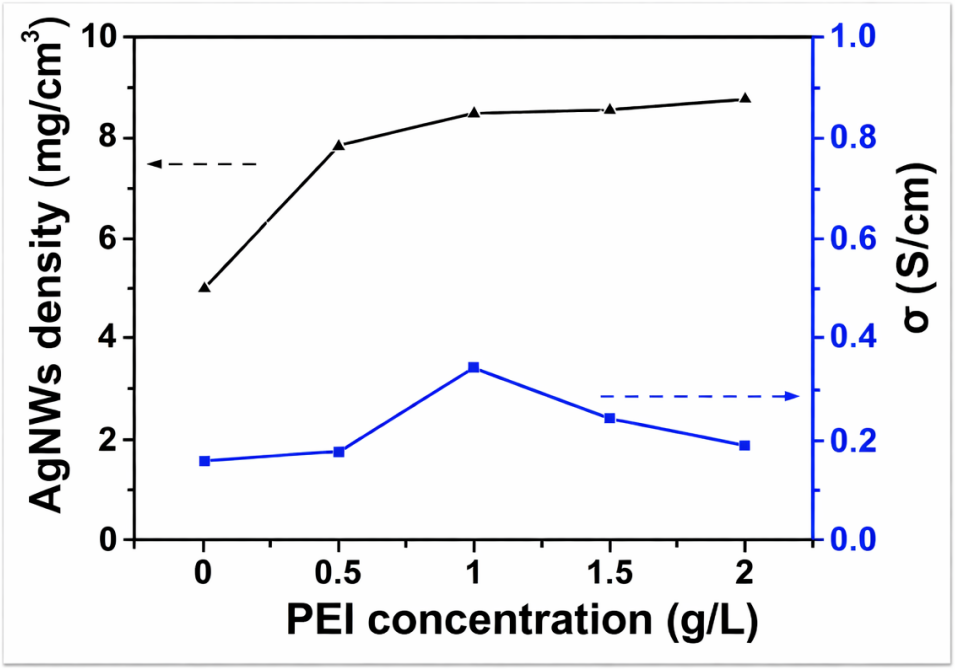

Figure 4.10: Relationship between PEI concentration, AgNWs loading density, and the electrical conductivity of the AgNWs@PEI_x@SiO_2 sponges.

In the composite sponges, AgNWs establish conductive networks that endow the material with electrical conductivity. Increasing the PEI concentration enhances the distribution and loading efficiency of AgNWs, resulting in a corresponding improvement in the electrical conductivity of the composites (Figure 4.10). The interconnections among the AgNWs establish a conductive network that enables electron transport throughout the composite sponge. In this system, electrical conduction is dominated by direct mechanical contact between neighboring AgNWs rather than by electron tunneling. As the PEI concentration increases, the electrical conductivity of the composite sponge initially rises and then declines. This trend is attributed to the aggregation observed in the AgNWs@$PEI_{1.5}$@SiO_2 and AgNWs@PEI_2@SiO_2 sponges, which increases the junction resistance within the AgNW network and consequently reduces conductivity. The elevated junction resistance results from the formation of thickened AgNW network domains within the SiO_2 sponge, which disrupts continuous charge transport pathways.

At higher PEI concentrations (1.5 g/L and 2 g/L), the AgNWs exhibit pronounced aggregation, forming layered network domains that align along the lamellar framework of the SiO_2 sponge. These AgNW layers are anchored to the SiO_2 architecture, where the fibers act as structural supports and contact points for the conductive framework. However, the development of such clustered AgNW domains compromises the uniform connectivity of

the conductive network and deteriorates the mechanical compressibility of the composite sponges(Figure 4.7).

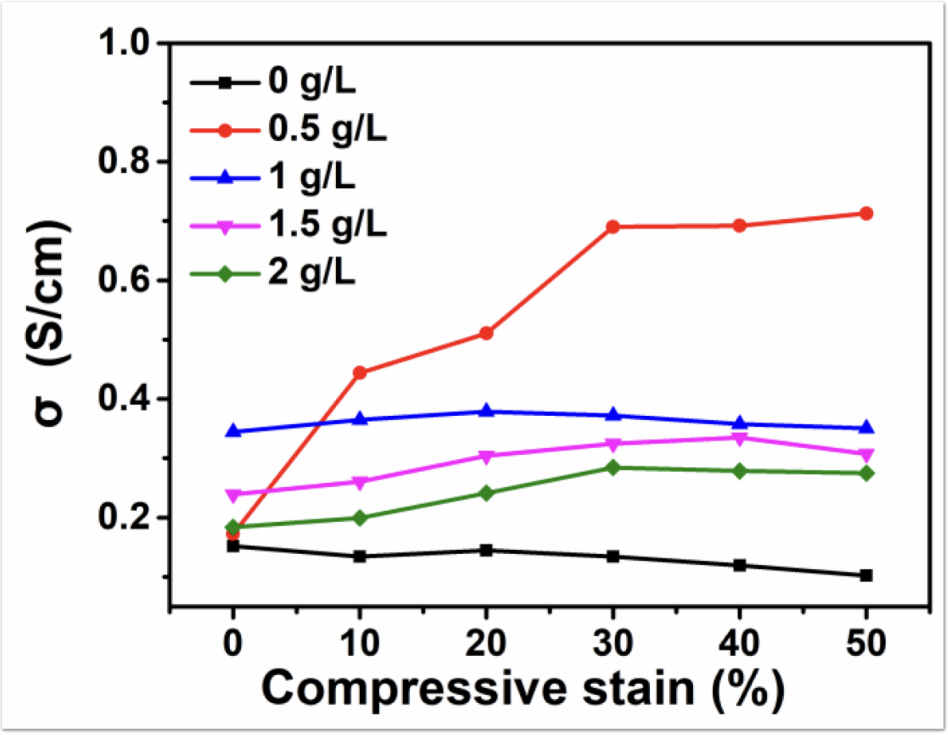

Figure 4.11: Electrical conductivity of AgNWs@PEI$_x$@SiO$_2$ sponges at different compressive strains, showing distinct variation trends among samples with different PEI concentrations. [181].

Electrical conductivity measurements were performed on the AgNWs@PEI$_x$@SiO$_2$ sponges at compression ratios of 10%–50% (Figure 4.11).

For AgNWs@PEI$_0$@SiO$_2$, the electrical conductivity decreases from 0.15 S/cm to 0.10 S/cm as the compression ratio increases. In the absence of PEI, the AgNW loading is insufficient to establish a stable conductive network. Upon compression, relative movement between AgNWs and SiO$_2$ fibers disrupts interwire contacts, resulting in increased contact resistance and reduced conductivity.

For AgNWs@PEI$_{0.5}$@SiO$_2$, the electrical conductivity increases from 0.17 S/cm to 0.71 S/cm with increasing compression ratio. Here, the AgNW content exceeds the percolation threshold and forms a partially continuous conductive network. Compression reduces the electron transport distance and enhances interwire contact density, thereby decreasing junction resistance and significantly improving conductivity.

In AgNWs@PEI$_1$@SiO$_2$, conductivity remains nearly constant across all compression ratios. At this PEI concentration, AgNWs are uniformly dispersed and form a well-

interconnected conductive network throughout the sponge. That's because network connectivity is already maximized, additional compression does not substantially alter the charge transport pathways.

For AgNWs@$PEI_{1.5}$@SiO_2 and AgNWs@PEI_2@SiO_2, only a slight increase in conductivity is observed upon compression. At higher PEI concentrations, excessive AgNW–AgNW interactions induce local aggregation, forming thickened layered network domains. Although compression increases the physical contact area within these aggregated domains, the presence of non-uniform conductive clusters increases junction resistance and limits the overall conductivity enhancement.

This behavior can be explained by the evolution of the conductive network under compression. When the AgNWs distribution is uniform and below the aggregation threshold, compression promotes conductive percolation by increasing interwire contacts. However, once AgNWs clustering occurs, network tortuosity and internal junction resistance dominate, limiting conductivity despite increased compression. Therefore, achieving an optimal balance between AgNW loading and dispersion is critical for maximizing the compression-responsive conductivity of the composite sponge.

When AgNWs are homogeneously dispersed, compression increases conductive connectivity (percolation enhancement). In contrast, when AgNWs aggregate, compression amplifies junction resistance within clustered domains (network tortuosity increase), resulting in limited conductivity improvement.

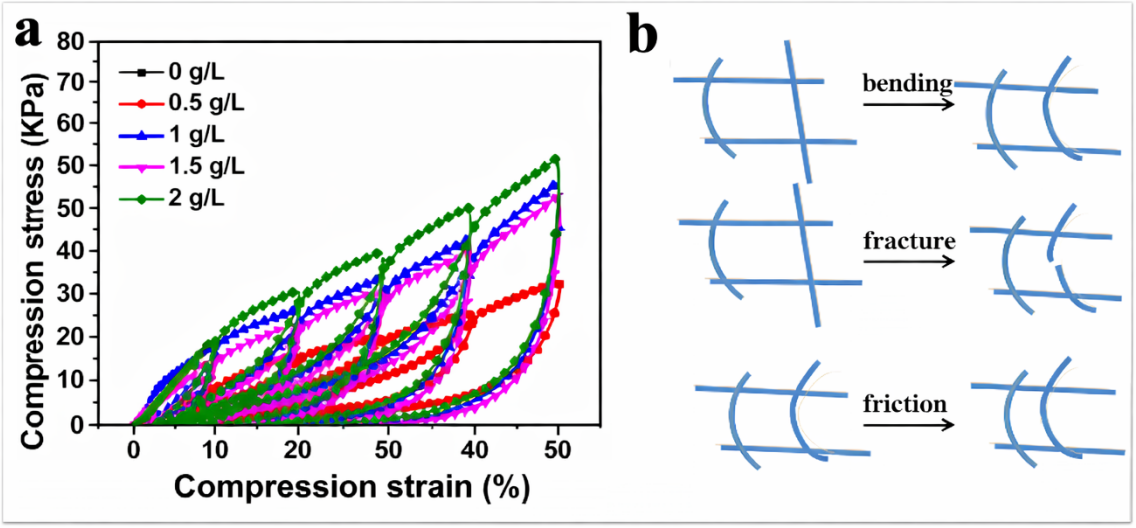

Figure 4.12: a. Typical compressive stress-strain curves of AgNWs@PEI_x@SiO_2 sponge at compression strains as 10%, 20%, 30%, 40% and 50%. b. Bending (the main mechanism, in which the overall structure undergoes bending deformation), Fracture (occurring only under extreme or fatigue compression), and mutual slip friction (the presence of AgNWs reduces but does not eliminate it); these three processes are the primary mechanisms for energy dissipation.

The compression performance of the AgNWs@PEI_x@SiO_2 sponges was evaluated to investigate their mechanical properties. At 50% compressive strain, the composite sponges exhibited compression strengths of 2.12 kPa, 0.99 kPa, 1.20 kPa, 1.13 kPa, and 1.37 kPa as the PEI concentration increased (Figure 4.12a). The variation in compression behavior is closely associated with the microstructural evolution of the composite framework and the spatial distribution of AgNWs within the sponge.

The corresponding deformation mechanisms-elastic bending, frictional sliding, and fracture-are illustrated in Figure 4.12b. During compression, the AgNWs@PEI_x@SiO_2 sponges undergo a bending-dominated deformation mode, in which the interconnected SiO_2 fibers bend elastically and reorganize structurally. Frictional sliding between neighboring fibers contributes to energy dissipation, while fracture occurs only at high strains. Meanwhile, the AgNWs network bridges adjacent SiO_2 fibers to form a secondary conductive framework. During deformation, this AgNWs network deforms cooperatively with the SiO_2 scaffold, maintaining electrical contact and preventing conductive pathway disruption. As a result, the composite sponges are able to withstand compressive deformation while preserving conductivity. At strains below 10%, the structure exhibits nearly complete elastic recovery. As strain increases, fiber bending becomes more pronounced, inter-fiber sliding increases, and limited fiber fracture occurs; however, upon unloading, bent and slipped fibers can largely return to their original configurations, leading to significant elastic recovery and high energy dissipation dominated by bending, friction, and localized fracture.

During sponge fabrication, SiO_2 fibers and SiO_2 sol were compounded *in situ* during the impregnation step, forming a fiber network bonded together by SiO_2 gel. This structure imparts intrinsic compression recovery capabilities. As shown in Figure 4.12, variations in AgNW loading induced by different PEI concentrations significantly influence the compression resilience of the AgNWs@PEI_x@SiO_2 sponges.

When the AgNW content is low (e.g., AgNWs@$PEI_{0.5}$@SiO_2), AgNWs mainly decorate the SiO_2 fibers, exerting minimal influence on the global mechanical framework; therefore, the compression recovery performance remains largely unchanged. As the PEI concentration increases, the distribution of AgNWs becomes altered throughout the SiO_2 network. In samples with higher AgNW loading, the interconnected AgNW domains hinder fiber hinge rotation and bending of the cavity walls during deformation, leading to increased plastic deformation and reduced compressive resilience.

In contrast, the AgNWs@PEI_1@SiO_2 sponge exhibits the best compressive resilience. At this PEI concentration, AgNWs are uniformly dispersed throughout the SiO_2 framework and form a dual-network structure that cooperatively reinforces the original SiO_2 scaffold.

This synergistic structural configuration enhances mechanical stability while maintaining conductive integrity.

4.1.4 CONCLUSION

In this chapter, the distribution pattern of AgNWs within a three-dimensional porous SiO_2 sponge was regulated by varying the concentration of PEI introduced through an impregnation process. A series of composite sponges were prepared to elucidate the conditions required for establishing a continuous conductive network using 80 µm AgNWs within a SiO_2 sponge of 90.35% porosity, modified with branched PEI (molecular weight 10,000) at different concentrations. The influence of AgNW distribution patterns and loading amounts on the compressive recovery behavior of the sponge was also systematically examined.

At a PEI concentration of 0.5 g/L, AgNWs are primarily dispersed on the surfaces of SiO_2 fibers, resulting in a structure suitable for strain-responsive sensing applications due to its compression-dependent conductivity. When the PEI concentration reaches 1.0 g/L, the AgNWs form a continuous interconnected conductive network throughout the SiO_2 framework, enabling stable electrical conductivity while maintaining favorable compressive resilience.

These results provide a reference strategy for controlling the spatial organization of metallic nanowires in three-dimensional porous architectures through polymer-assisted surface modification, offering guidance for the design of conductive, flexible, and structurally adaptable composite materials in diverse application contexts.

4.2 ULTRA-LIGHTWEIGHT POROUS AGNW/SIO_2 SPONGE WITH POLYSILOXANE MODIFICATION FOR MULTIFUNCTIONAL APPLICATIONS

In the previous chapter, silica fibers were surface-modified using the binder PEI, and a composite sponge composed of metal nanowires and silica fibers was fabricated via an impregnation approach. The functional groups of PEI were employed to regulate the spatial distribution of AgNWs, thereby enabling modulation of the electrical conductivity of the composite. However, the resulting composite sponge exhibited poor compressive resistance. The inadequate mechanical performance was attributed to the dispersion state of the nanowires within the sponge, particularly within the lamellar fiber regions. The presence of AgNWs within these fiber layers increased localized stress on the interlayer supporting fibers of the honeycomb-like framework, rendering them more prone to irreversible deformation or collapse under external loading. This structural instability significantly restricted the practical applicability of the composite. Therefore, it is essential to regulate the distribution of AgNWs during the design and fabrication of multifunctional AgNW–nanofiber-based sponges, in order to avoid local load concentration caused by local load concentration, which may otherwise lead to instability of the internal supporting structure during compression.

4.2.1 PREPARATION OF AgNWs, SIO_2 SPONGE AND COMPOSITE SPONGES

Flexible silica nanofibers and AgNWs were employed as the structural building blocks, and a nanowire–nanofiber composite sponge was fabricated through a combination of electrospinning, freeze-drying, and in situ bonding techniques (Figure 4.13). The preparation of AgNWs and silica fibers followed procedures similar to those used in the previous chapter, with minor adjustments to experimental parameters. In the present study, however, a Q-siloxane coupling agent (SiO_2 gel precursor) was introduced into the mixed suspension of silica fibers and AgNWs. Hydrolysis and condensation of the Q-siloxane facilitated the formation of chemical bonds among silica fibers, AgNWs, and their respective surfaces, thereby enhancing structural integration.

The Q-silane coupling agent contains a silicon atom coordinated to four hydrolyzable ethoxy groups (OCH_2CH_3). Upon exposure to water and phosphoric acid, hydrolysis generates silanol groups, which subsequently undergo condensation reactions to form siloxane (Si–O–Si) linkages. During this process, both the silica fibers and AgNWs become coated with the newly formed siloxane network, resulting in the construction of a robust inter-

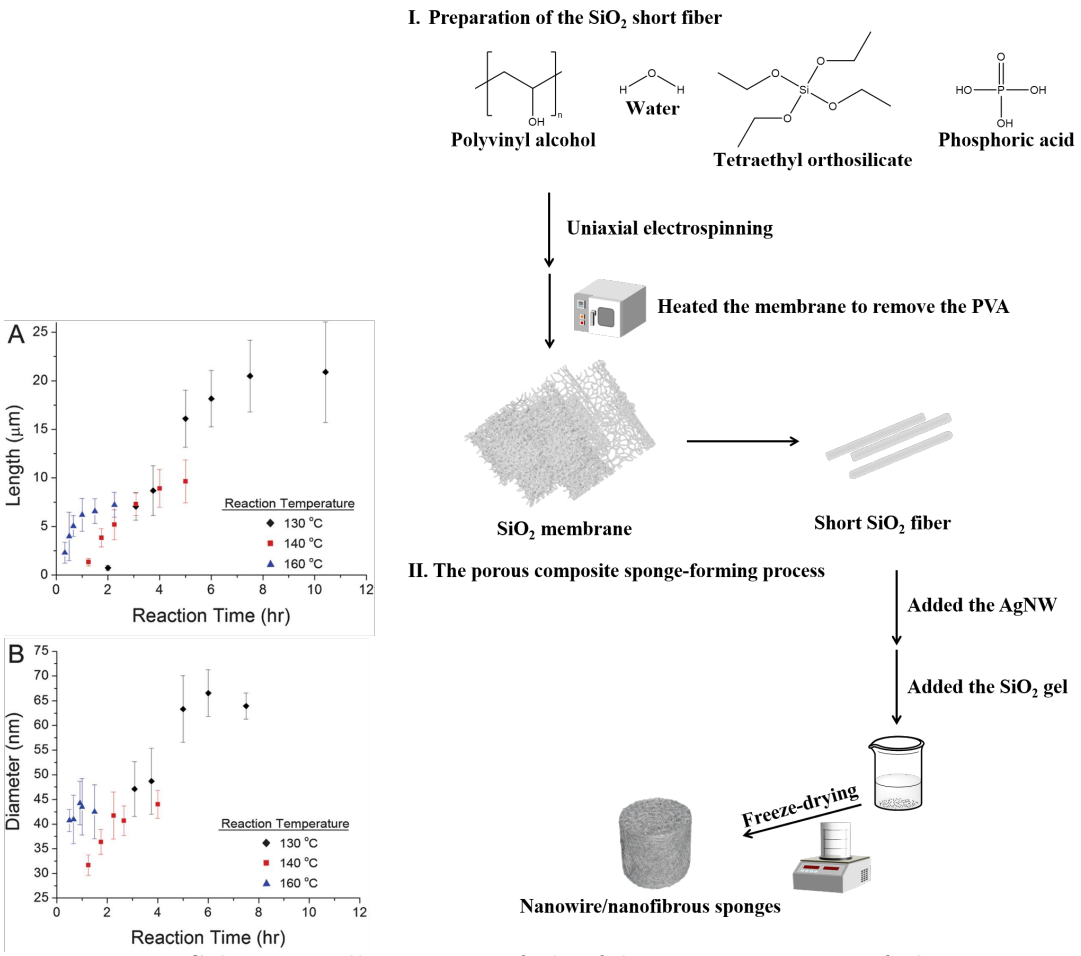

Figure 4.13: Schematic illustration of the fabrication process of the composite sponges from electrospun short silica fiber, AgNWs, and polysiloxane film. The AgNW was prepared based on the previous work in that we controlled the experiment condition to change the diameter and length of AgNWs. The insert Figures A and B are the experiment parameters of the silver nanowire prepared with different diameters and lengths. © 2012 RSC. Used with permission.

connected architecture. Following gelation, the composite was subjected to freeze-drying to remove the solvent while preserving the hierarchical porous structure, yielding the AgNWs/SiO_2 composite sponge. The final macroscopic shape of the sponge can be tailored by mold geometry; in this chapter, cylindrical sponges were selected for systematic investigation. Upon incorporation of AgNWs, the macroscopic appearance of the SiO_2 sponge changes from white to gray, indicating the presence and dispersion of AgNWs within the porous network. The silica fibers exhibit diameters predominantly in the range of 350–500 nm and lengths of 100–200 µm, forming a flexible fibrous framework. The AgNWs possess diameters of approximately 100–180 nm and lengths of 20–60 µm, enabling their effective integration with the silica fiber network. These dimensional characteristics establish the geometric basis for nanowire–nanofiber contact and network formation within the composite structure.

4.2.2 FABRICATION AND MULTI-SCALE STRUCTURE FEATURES OF AGNW/SiO_2 NANOWIRE-NANOFIBROUS SPONGE

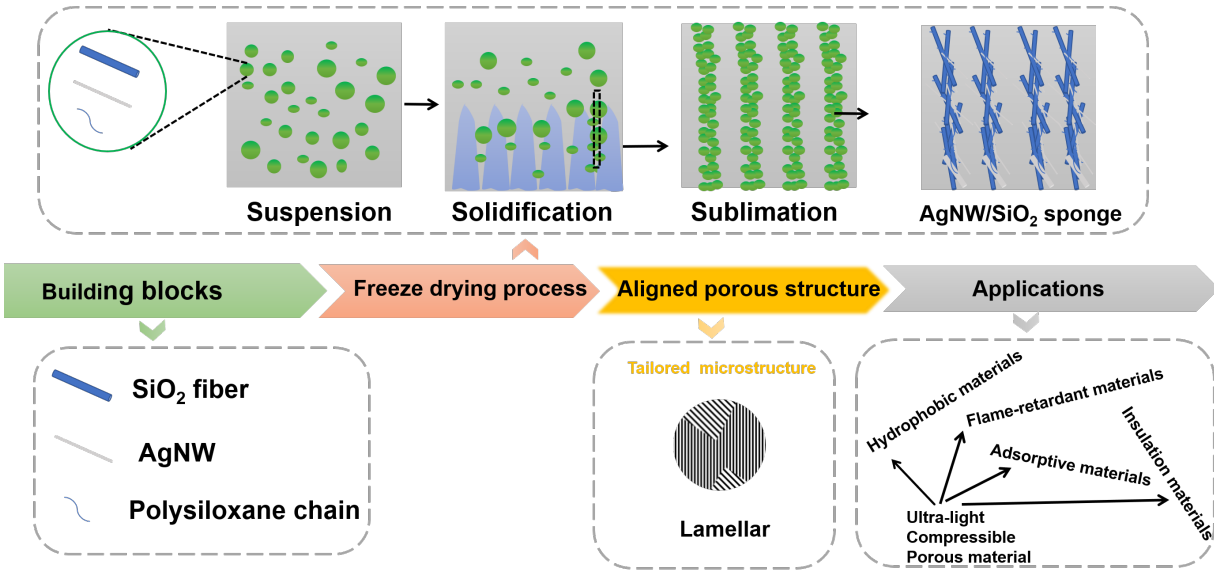

Figure 4.14: Schematic illustrating the fabrication of AgNW/SiO_2 sponges, their internal structure, and potential applications.

AgNWs synthesized via the polyol method and flexible silica nanofibers prepared through electrospinning were selected as the primary structural components. These were combined with a polysiloxane binder, and nanowire–nanofiber composite sponges with a lamellar porous architecture were fabricated using freeze-drying and in situ bonding techniques. During the fabrication process, the polysiloxane (Q-siloxane coupling agent) was generated through the acid-catalyzed hydrolysis of tetraethyl orthosilicate (TEOS) under strongly acidic conditions (pH 1–2), and subsequently adsorbed onto the surfaces of both silica fibers and AgNWs. This in situ formed polysiloxane not only enabled interfacial bonding between the nanowires and nanofibers but also modulated the growth and sublimation of ice crystals during freeze-drying, thereby governing the hierarchical pore structure of the final sponge. As a result, composite sponges with ultralight density and excellent compressive resilience were obtained, demonstrating broad potential for multifunctional applications (Figure 4.14).

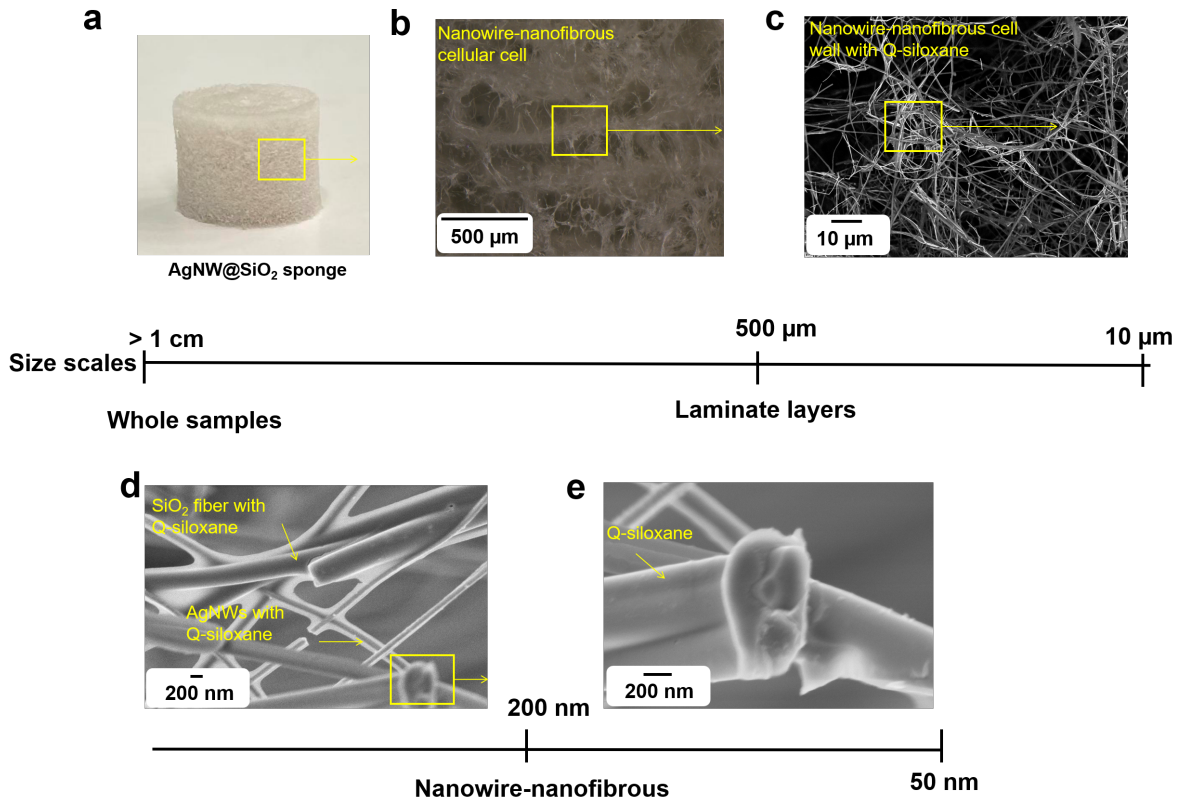

Figure 4.15: a. A hand-drawn photograph of an AgNW/SiO_2 sponge. b-e. Microscopic structures of AgNW/SiO_2 sponge at different magnifications demonstrate the hierarchical architecture. f. the different scale levels of the relevant structure, covering hierarchical structures ranging from the centimeter scale down to the nanometer scale in AgNW/SiO_2 sponge.

To characterize the internal morphology of the AgNW/SiO_2 sponges, microscopic observations were carried out. A schematic representation of the AgNW/SiO_2 sponge is shown in Figure 4.15a, while the corresponding macro- and microstructural features are displayed in Figure 4.15b–e. The composite exhibits an open-cell, lamellar porous architecture composed of silica fibers and AgNWs, both of which are uniformly coated with polysiloxane. The complete encapsulation of silica fibers and AgNWs is attributed to the solvent phase transition during the freeze-drying process. Initially, the silica fibers, AgNWs, and polysiloxane form a homogeneous aqueous dispersion. Upon freezing, advancing ice fronts exclude the solid components, causing them to accumulate within the interstitial regions between growing ice crystals. After full solidification, the silica fibers, AgNWs, and polysiloxane chains become physically entangled and constrained within the frozen matrix. Subsequent freeze-drying removes water through sublimation, preventing capillary-induced collapse and thereby preserving the hierarchical porous structure.

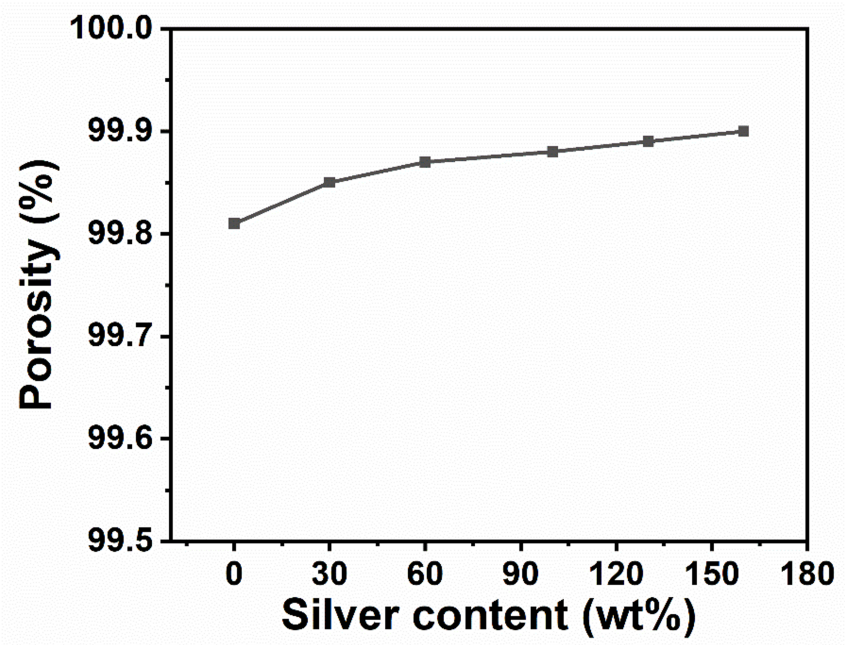

Figure 4.16: Porosity variation of the composite sponge caused by the change in the loading amount of AgNWs in the silica sponge.

The prepared sponge exhibits a highly porous structure (Figure 4.16). As is characteristic of freeze-cast porous materials, the morphology of the ice crystals during freezing directly dictates the pore structure of the final sponge. Structural tunability is therefore achieved by controlling the freezing rate: slower freezing leads to the formation of larger ice crystals, whereas faster freezing produces finer pore structures.

Figure 4.15f illustrates the hierarchical organization of the sponge, which can be decomposed into three characteristic length scales: the macroscopic bulk structure, the lamellar cell walls composed of unit fibrous layers, and the nanoscale fiber network. The clear definition of these structural levels provides a mechanistic basis for understanding the excellent compressive resilience and multifunctional performance demonstrated in subsequent sections.

Unless otherwise specified, the composite sponge is referred to as AgNW/SiO_2 throughout this work, corresponding to a silver nanowire loading level of 100% (i.e., the mass of AgNWs is equal to the mass of silica fibers in the composite). Such hierarchical structuring, combined with the interconnected nanowire–nanofiber framework, is expected to play a critical role in governing the mechanical deformation behavior of the composite sponge.

4.2.3 CHARACTERIZATION OF AGNW/SIO_2 SPONGE

Mechanical performance and analysis

It is well established that sponges constructed from flexible silica fibers exhibit favorable compressive deformability [182]. To evaluate the influence of AgNWs on the mechanical properties of the composite sponges, compression tests were performed using a universal testing machine. The AgNW/SiO_2 sponge demonstrates excellent elasticity and enhanced compressive performance. As shown in Figure 4.17a, the compressive stress of the Ag/SiO_2 sponge reaches 0.47 kPa, representing a 124% increase compared to that of the pure silica sponge (0.21 kPa). After 50 loading–unloading cycles, the stress–strain curves show negligible deviation, and no plastic deformation is observed, indicating outstanding compression fatigue resistance (Figure 4.17b). During a 100-cycle compression test, the compressive stress remains consistently above 0.38 kPa, while the mechanical work gradually increases to 1.31 mJ (Figure 4.17c).

The energy dissipation behavior was evaluated from the hysteresis loops of the loading and unloading curves. The energy loss coefficient stabilizes at approximately 0.041 after 100 cycles, with the energy loss converging to 0.055 mJ after around 30 cycles (Figure 4.17d). These stable cyclic properties confirm that the mechanical reinforcement is structurally inherent rather than transient or defect-derived. The enhanced compressive performance is attributed to the uniform distribution of AgNWs within the SiO_2 framework, where the polysiloxane effectively encapsulates both AgNWs and silica fibers (Figure 4.17e), and no AgNW agglomeration is observed within the sponge (Figure 4.17f).

As a continuous secondary phase, the ultrafine AgNW network winds around the silica fibers at the cell wall junctions, forming a cooperative deformation support system that significantly enhances structural stability under compression. To further elucidate this deformation mechanism, in situ optical observations were conducted during compression and recovery. As the applied strain (ϵ) increases to 50%, the nanofiber unit cavities are gradually compressed, and the interlayer fibers undergo bending and collective tilting. Upon release of the applied load, the elastic potential energy stored in the interconnected solid network is progressively released, enabling the structural components and pore geometry to return to their initial states. No fracture, collapse, or irreversible damage is observed throughout the deformation–recovery cycle (Figure 4.18a–d), confirming that the AgNW/SiO_2 sponge possesses high compressive resilience and ultrahigh elasticity under large deformation.

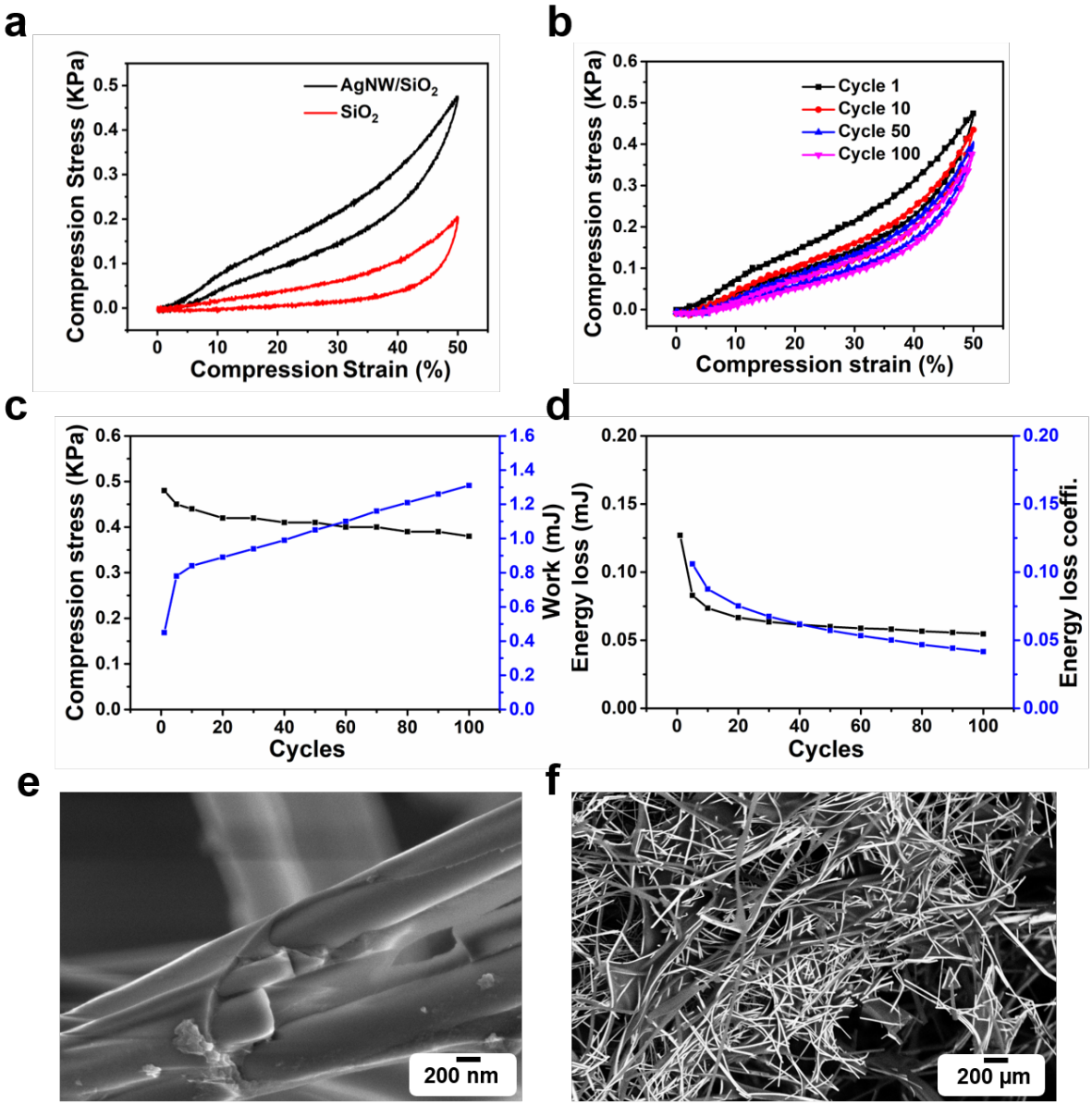

Figure 4.17: Mechanical properties of the AgNW/SiO_2 sponges under compression. a. Compressive stress-strain curves of SiO_2 and AgNW/SiO_2 sponge at 50% strain. b. Compressive stress-strain curves at 50% standard strain and different numbers cycles of AgNW/SiO_2 sponge. c. Stress and work done during 100 cycles at 50% standard strain of AgNW/SiO_2 sponge. d. Energy loss and energy loss coefficient during 100 cycles at 50% standard strain of AgNW/SiO_2 sponge. e. SEM image of silica fibers and Ag encapsulated in polysiloxane. f. SEM-BSE image of AgNW/SiO_2 sponge.

To verify the hypothesis that AgNWs do not undergo aggregation within the composite sponge, EDS measurements were performed at multiple representative locations throughout the material. The elemental spectra of Si, O, and Ag indicate that AgNWs are uniformly distributed along the silica fiber framework, with no evidence of localized Ag clustering (Figure 4.19a–c). Quantitative elemental analysis further confirms that the variation in Ag content across different regions of the sponge is within 5% (Figure 4.19d),

demonstrating that the distribution of AgNWs is spatially homogeneous within the composite.

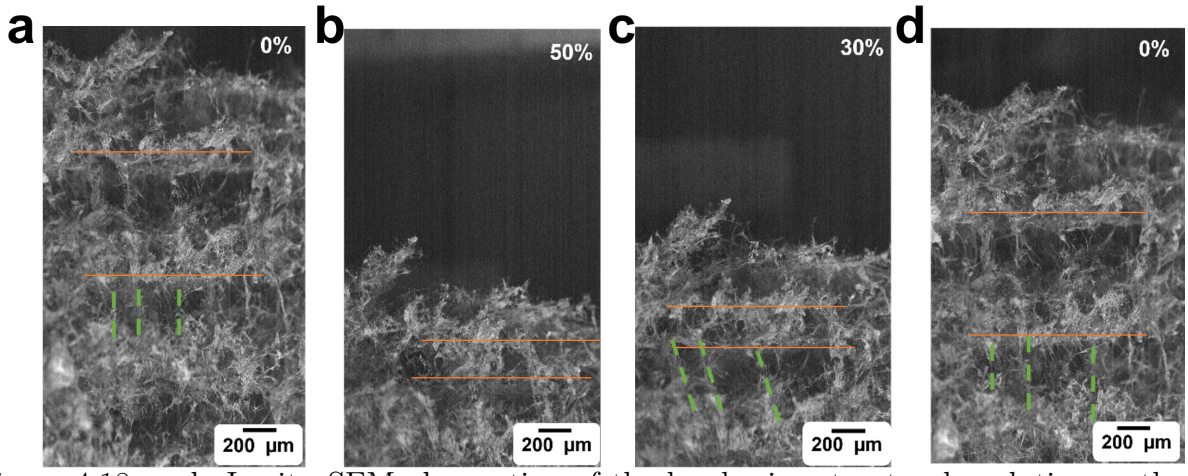

Figure 4.18: a-d. In-situ SEM observation of the local microstructural evolution as the strain increases to 50%, followed by partial recovery to 30% and finally returning to the initial state. The distance between the compared layers (highlighted by the green dashed lines) remains unchanged.

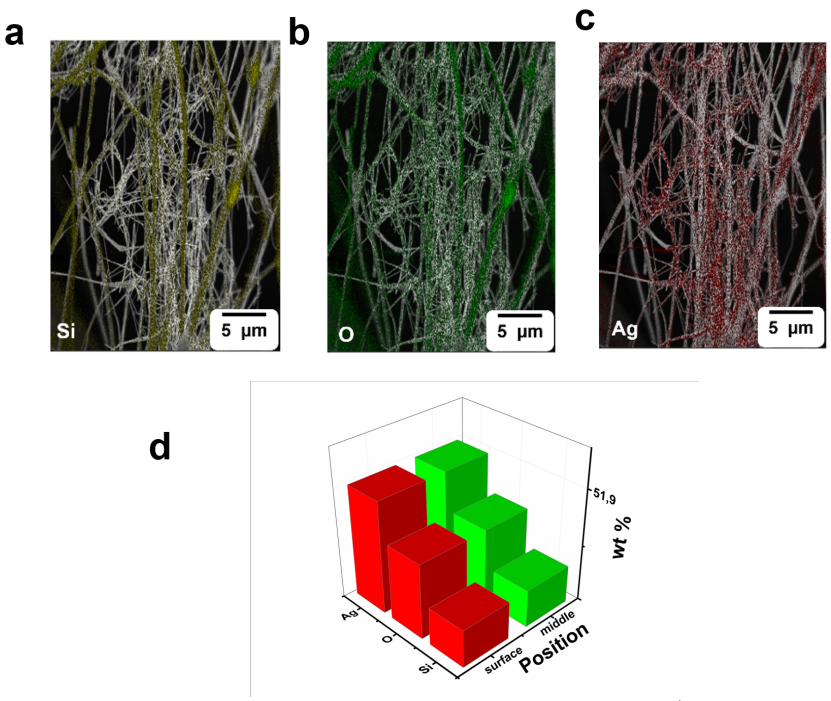

Figure 4.19: a-c. the element mapping of Si, O, Ag in AgNW/SiO_2 sponge. d. Quantitative analysis of the elements shows that the difference in Ag content among different locations in the composite is within 5%

Thermal insulation and flame retard resistance

The dispersion behavior and homogeneity of AgNWs within the silica sponge influence not only the mechanical performance but also the thermal conductivity of the porous

composite. Porous materials function as thermal insulators by suppressing heat transfer driven by temperature gradients. The thermal conductivity of the composite sponges was therefore measured using a Hotdisk thermal constant analyzer. Because the AgNW mass—the primary variable in this study—is on the milligram scale, the instrument was calibrated prior to testing to ensure measurement accuracy.

As shown in Figure 4.20a, the introduction of AgNWs reduces the thermal conductivity of the sponge by 11.17% relative to the pure silica sponge. Furthermore, the AgNW/SiO_2 composite sponge exhibits lower thermal conductivity than pure AgNW foam, pure SiO_2 sponge, and several other reported porous sponge systems (Figure 4.20b) . This reduction in thermal conductivity is attributed to the hierarchical lamellar architecture and composite composition of the sponge, which introduce multiple solid–air interfaces and enhance phonon scattering across the network .

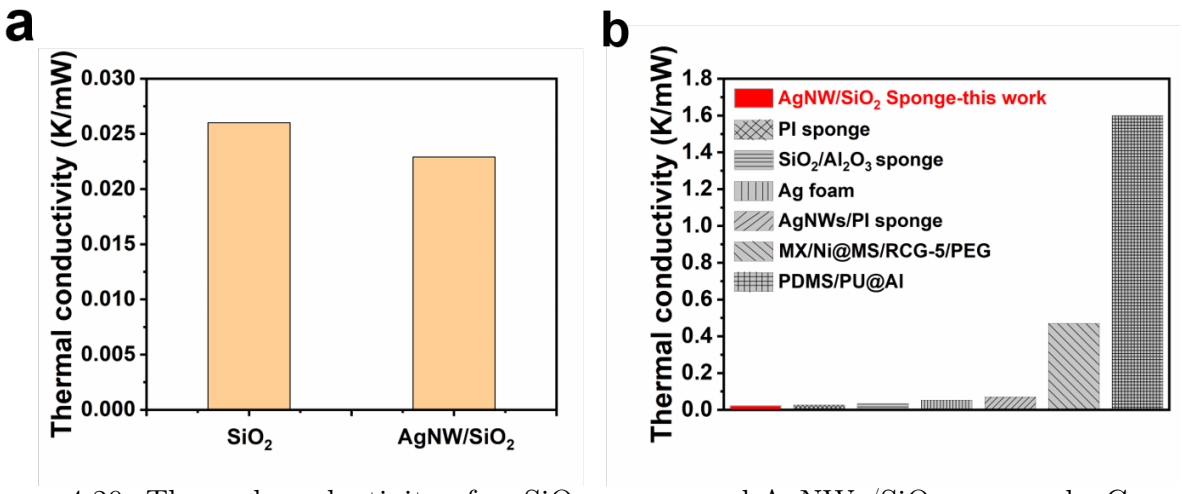

Figure 4.20: Thermal conductivity of a. SiO_2 sponge and AgNW /SiO_2 sponge; b. Comparison of thermal conductivity with PI sponge, SiO_2/Al_2O_3 sponge, Ag foam, AgNWs/PI sponge, MXNi@MS/RCG-5/PEG, and PDMS/PU@Al sponge.

The AgNW/SiO_2 sponge in the solid state achieves a minimum thermal conductivity of 0.0229 $W{\cdot}m^{-1}{\cdot}K^{-1}$, which is lower than that of air (0.0259 $W{\cdot}m^{-1}{\cdot}K^{-1}$) and lower than that of a SiO_2/C sponge (0.0245 $W{\cdot}m^{-1}{\cdot}K^{-1}$) (Figure 4.21a). In addition to the Hotdisk method, thermal conductivity was also evaluated using the transient hot-bridge technique (Figure 4.21b). Although the absolute conductivity values obtained using this technique are higher (e.g., 0.054 $W{\cdot}m^{-1}{\cdot}K^{-1}$ for SiO_2 sponge and 0.050 $W{\cdot}m^{-1}{\cdot}K^{-1}$ for AgNW/SiO_2 sponge at an AgNW loading of 130 wt%), the same trend is observed: the presence of AgNWs consistently reduces the thermal conductivity compared to the pure SiO_2 sponge.

The discrepancy in absolute values between the two techniques can be attributed to differences in interfacial thermal resistance between the sensor and sample, power density, probe penetration depth, and measurement time scales. Nevertheless, across both mea-

surement methods, AgNW/SiO_2 sponges consistently exhibit lower thermal conductivity than pure SiO_2 sponges, indicating that the introduction of AgNWs contributes to enhanced thermal insulation performance.

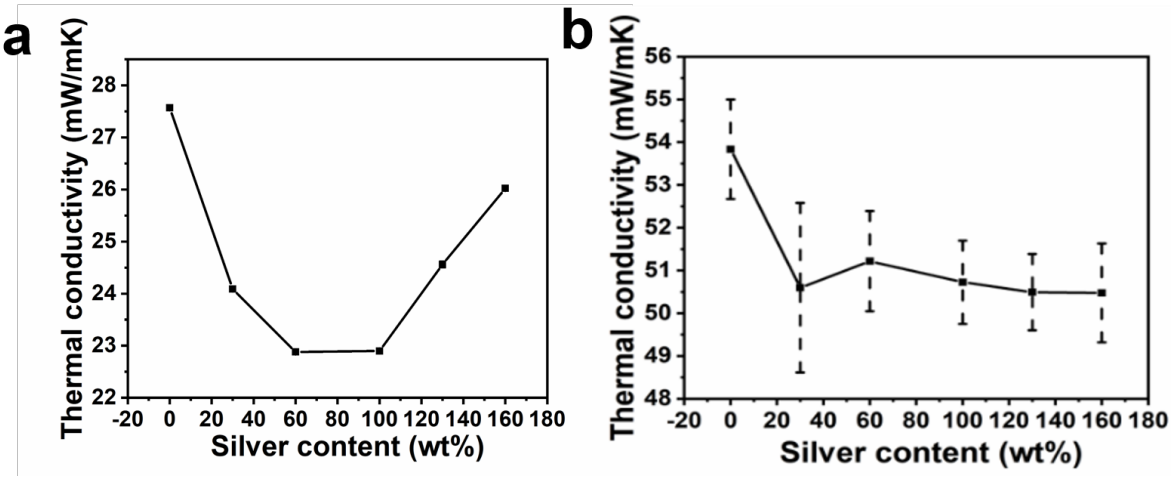

Figure 4.21: a. Thermal conductivity of the composite sponges with varying AgNW contents measured using the HotDisk method. b. Thermal conductivity of the composite sponges with varying AgNW contents measured using the Transient Hot Bridge method.

Since thermal insulation performance is closely associated with electrical insulation, the electrical insulating behavior of the AgNW/SiO_2 sponge was also evaluated and confirmed.

In general, the total thermal conductivity of a composite sponge (λ_{sum}) can be expressed as the sum of its conductive thermal conductivity (λ_{con}), radiative thermal conductivity (λ_{rad}), and gas thermal conductivity (λ_{gas}):

$$\lambda_{sum} = \lambda_{con} + \lambda_{rad} + \lambda_{gas}.$$

At room temperature, λ_{con} is typically the dominant contributor to heat transfer in the AgNW/SiO_2 sponge, and the combined influence of λ_{con} and λ_{gas} largely determines λ_{sum} (Figure 4.22g). During the thermal conductivity measurement, heat propagates from the center of the sponge outward. Owing to the anisotropic lamellar architecture of the sponge, heat transfer can be analyzed along two principal directions.

In the vertical direction (Y–Z plane, Figure 4.22a), the low thermal conductivity is primarily attributed to the honeycomb-like fiber framework and high porosity, which significantly reduce the solid-phase thermal conduction (λ_{con}) through nanofibers oriented out of the lamellar plane. The limited change in thermal conductivity upon AgNW incorporation is explained by the preparation process: only a small amount of AgNW is distributed at the interlayer junctions, exerting negligible influence on the pore geometry (Figure 4.22b–c). Consequently, the overall thermal conductivity remains nearly unchanged in this direction.

In contrast, along the horizontal direction, the Ag loading is considerably higher (Figure 4.22b, positions A and B). Comparison of Figure 4.22e and Figure 4.22f shows that AgNWs form a nanowire–nanofiber hybrid layer within the lamellae. For pure SiO_2 sponges, heat transfer primarily occurs through a single continuous silica fiber network. However, upon the introduction of AgNWs, a secondary conductive phase is added. As a reflective metallic phase, AgNWs scatter and extend the heat transport pathways, thereby increasing phonon scattering and inhibiting directional heat flow.

Furthermore, the incorporation of AgNW reduces the pore aperture within the lamellar plane (Figure 4.22h–i), which suppresses gas-mediated heat transfer (λ_{gas}) and reduces radiative heat exchange (λ_{rad}). This collectively results in a net decrease in thermal conductivity. The slight increase in thermal conductivity observed at higher AgNW loadings may be attributed to the formation of partial percolation between AgNWs and silica fibers. The heterogeneous overlapping of AgNW and SiO_2 fibers creates localized pathways for heat conduction, while interfacial thermal resistance at AgNW–SiO_2 junctions modifies the balance between scattering and conduction.

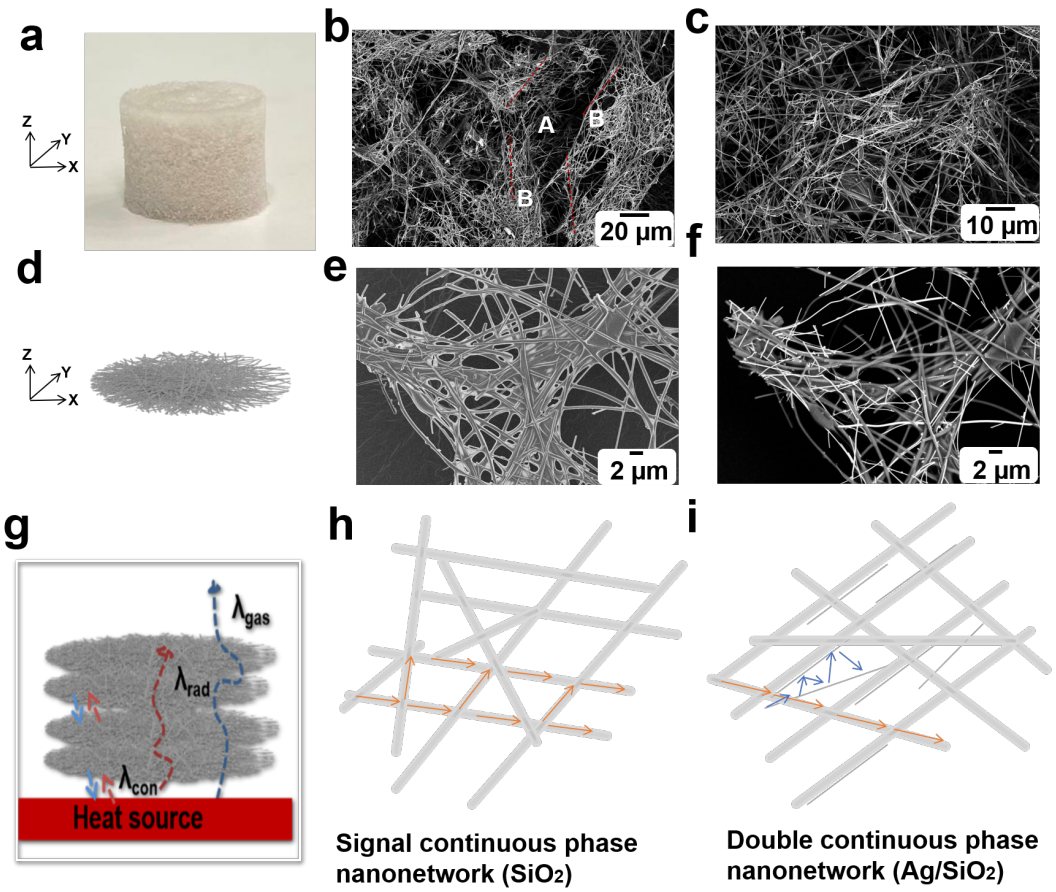

Figure 4.22: a. and d. Schematic diagrams of the AgNW/SiO_2 sponge structure and sponge lamellar fibers. b-c and f. SEM-BSE images of the AgNW/SiO_2 sponge. e. SEM image of the AgNW/SiO_2 sponge. g. Schematic representation of the thermal conductivity propagation within the overall structure of the sponge. h-i. Roadmap of single SiO_2 and double AgNW/SiO_2 continuous phase networks for thermal conductivity.

To further evaluate the thermal insulation performance of the composite sponge, the AgNW/SiO_2 sponge was placed on a heat source maintained at 210 °C for 10 minutes, and its temperature evolution was monitored (Figure 4.23a). After approximately 2 minutes, the temperature difference between the top and bottom surfaces of the sponge reached 120 °C (Figure 4.23b), demonstrating its excellent thermal insulation capability. Considering the common risk of thermal exposure in practical use, the thermal stability and flame-retardant behavior of the AgNW/SiO_2 sponge were also examined. Under direct high-temperature flame exposure from a butane torch, the composite sponge maintained its structural integrity without visible combustion even after 300 s of heating (Figure 4.23c). Subsequent infrared thermography measurements revealed that the temperature of the sponge surface was substantially lower than the 1100 °C flame temperature, further confirming its exceptionally low thermal conductivity.

The outstanding thermal insulation and flame-retardant properties of the AgNW/SiO_2 sponge are primarily attributed to its nanoscale silica framework and hierarchical porous

network, which significantly suppress heat transfer. Additionally, the coexistence of AgNWs and silica fibers introduces coupled heat-transfer pathways, wherein phonon scattering at heterogeneous interfaces further contributes to reduced thermal transport.

After flame exposure, a distinct color change in the sponge was observed (Figure 4.24a–b). This change originates from a thermal depolymerization–repolymerization (unzipping) process involving siloxane species. At high temperatures, the terminal ethoxy groups in tetraethyl orthosilicate undergo hydrolysis to form silanol groups, which subsequently undergo condensation reactions, increasing the local crosslink density and altering the optical properties of the polysiloxane coating [183]. Concurrent intramolecular redistribution produces low-molecular-weight cyclic siloxanes, leading to a visible color transition from gray to yellow.

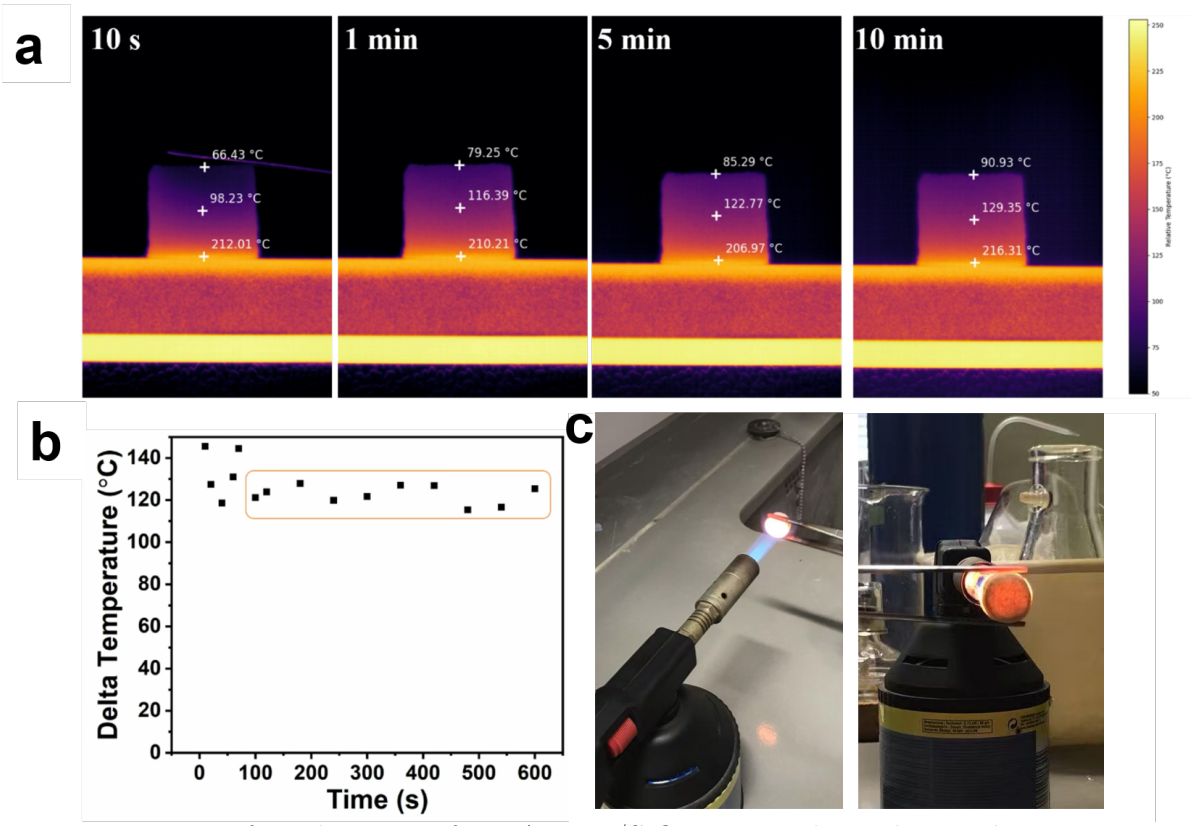

Figure 4.23: a. Infrared image of an AgNW/SiO_2 sponge heated on a heat source at approximately 210 °C. b. Temperature difference between the bottom and top of an AgNW/SiO_2 sponge over time. c. Optical images of AgNW/SiO_2 sponge heated from both sides using a butane torch.

To further confirm the intrinsic flame-retardant characteristics, the sponge was exposed to combustion testing in a 100% oxygen atmosphere. Remarkably, the AgNW/SiO_2 sponge remained non-flammable under these conditions as well (Figure 4.24c–d), demonstrating that its flame-resistant behavior is independent of atmospheric conditions. In addition

to flame retardancy, the hydrophilicity of the sponge also plays an important role in determining its potential application versatility.

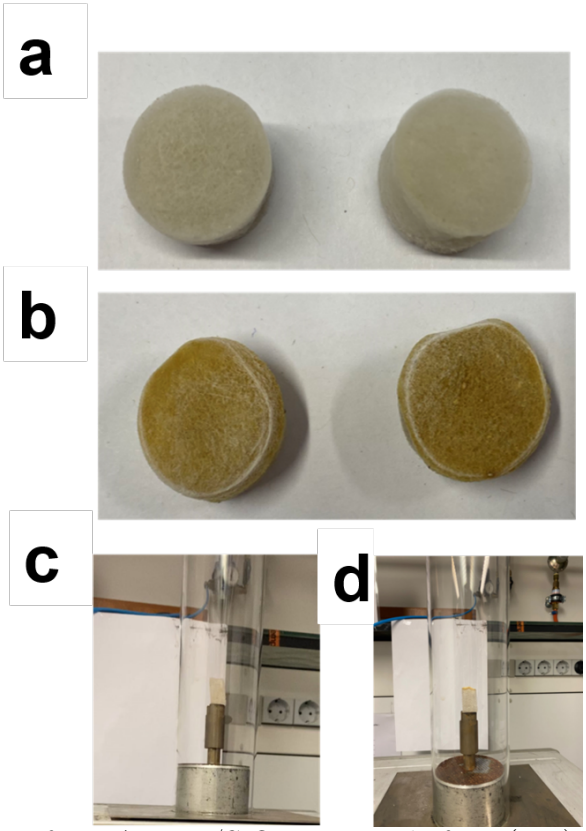

Figure 4.24: a-b. Color of an AgNW/SiO_2 sponge before (top) and after (bottom) 5 minutes of heating with a butane torch. c-d. Images showing the process of the LOI test on an AgNW/SiO_2 sponge before (left) and after (right) under a 100% O_2 atmosphere.

Wettability of AgNW/SiO_2 sponge

Silica sponges and AgNW/SiO_2 sponges exhibit markedly different wetting behaviors owing to differences in their surface morphology and chemical composition. The pure silica sponge shows a contact angle of 0°, indicating superhydrophilicity and a high surface energy surface. Upon incorporation of AgNWs, the surface roughness is significantly altered, leading to a transition from high to low surface energy. As a result, the AgNW/SiO_2 sponge displays a contact angle exceeding 110°, demonstrating pronounced hydrophobicity (Figure 4.25). This wetting transition can be interpreted through the Cassie–Baxter model [184], which states that increased surface roughness introduces trapped air pockets within the micro/nanostructure, reducing the actual solid–liquid contact area and thereby promoting hydrophobic behavior.

In this material system, the hierarchical surface structure consists of silica fibers as the primary scaffold, AgNWs as an interfacial roughness-enhancing layer, and a polysiloxane coating that encapsulates both fiber types. The highly porous architecture of the composite sponge (porosity > 95%, Figure 4.16) enables substantial air entrapment, further sup-

porting the Cassie–Baxter state. Moreover, the presence of siloxane- and Si–C-containing groups introduced during the hydrolysis–condensation of tetraethyl orthosilicate (TEOS) contributes to reduced surface energy (Figure 4.26). During the reaction, hydrolysis of the ethoxy (–OR) groups in TEOS forms reactive silanol (Si–OH) groups, which subsequently condense to form a crosslinked siloxane network. The resulting Si–O–Si and Si–O–C bonding structures impart intrinsic hydrophobicity to the sponge surface.

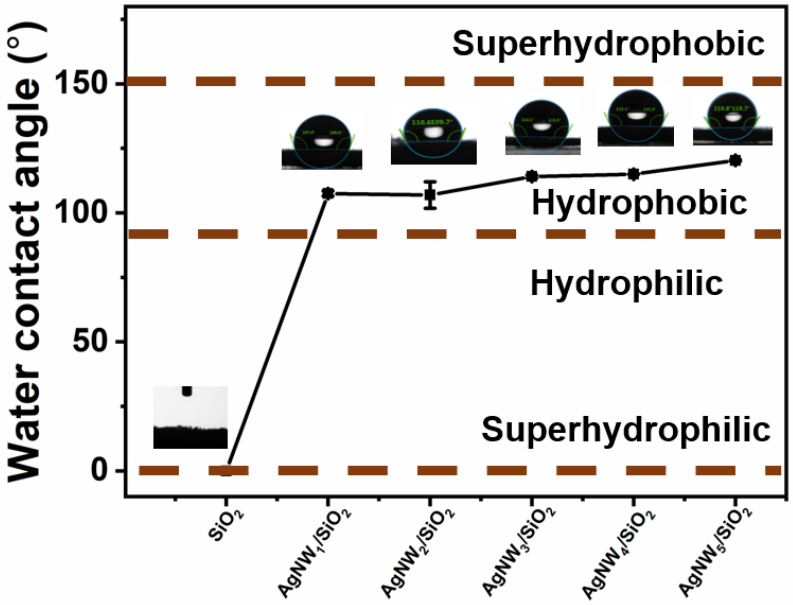

Figure 4.25: Contact angle evolution of the AgNW/SiO_2 sponge, revealing the tunable transition of the surface from hydrophilic to hydrophobic.

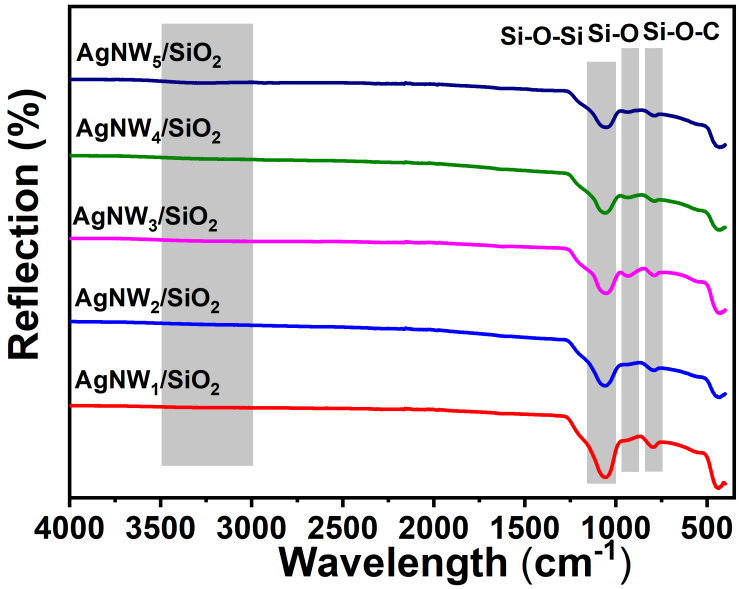

Figure 4.26: FT-IR spectrum of the AgNW/SiO_2 sponge, showing the presence of siloxane and silicon–carbon bonds within the composite.

Consequently, the combined effects of (i) hierarchical roughness induced by AgNWs, (ii) high porosity enabling air entrapment, and (iii) siloxane-derived low surface energy lead to the observed hydrophobic transition. Notably, the AgNWs provide mechanical interlocking that stabilizes the polysiloxane coating, allowing the hydrophobic state to remain robust under external abrasion or chemical exposure.

Such low-surface-energy behavior is of practical relevance for dye-removal applications in industrial wastewater treatment, where hydrophobic composite sponges can improve solvent recyclability, enhance dye adsorption–desorption efficiency, and reduce environmental contamination.

Adsorption performance

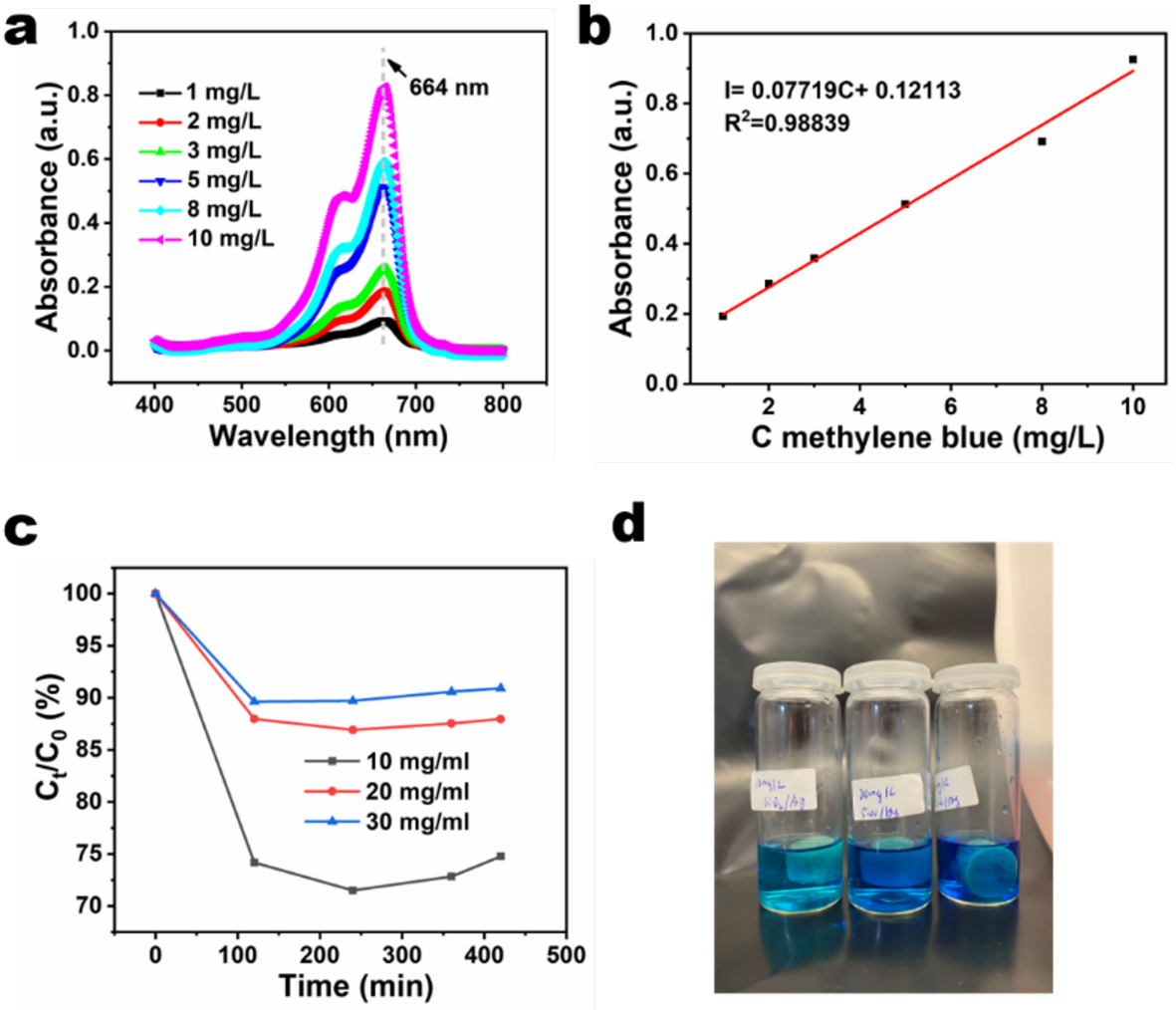

Figure 4.27: Quantification analysis of methylene blue content by a UV-vis spectrum. a. Standard curves in water. b. The scattering plot of methylene blue in water by UV-vis c. The relationship between time and methylene blue residual. d. The photograph is taken after the dye absorption of an AgNW/SiO_2 sponge.

Sponges can also serve as light-weight absorbent receivers for recovering organic solvents from dye-containing coating waste, thereby improving solvent utilization efficiency and

reducing environmental contamination. In this study, methylene blue (MB), a typical cationic organic dye widely used in the textile industry, was selected as a model pollutant [185]. The adsorption behavior of MB at low concentrations was investigated under ambient conditions at the liquid–solid heterogeneous interface.

Contact filtration adsorption was employed by immersing the sponge in MB-contaminated organic solvents. MB was used as a probe molecule to evaluate the adsorption capacity of the sponges. The residual dye concentrations in water and chloroform were quantified using UV–Vis spectroscopy. A standard calibration curve was first established, and the absorbance of the remaining dye in solution was measured at defined concentration intervals. Representative optical images of the sponge after adsorption were also recorded (Figures 4.27 and 4.28). In addition, adsorption behavior in a high-concentration MB–chloroform mixture was examined, with results shown in Figure 4.29.

The AgNW/SiO_2 sponge does not exhibit strong adsorption performance in aqueous dye solutions or in high-concentration dye–chloroform mixtures (Figures 4.27, 4.28, 4.29, and 4.32a). However, at low dye concentrations, the AgNW/SiO_2 sponge demonstrates significantly enhanced MB adsorption relative to the pure SiO_2 sponge. This improved adsorption capacity is attributed to interfacial affinity effects. MB is a polar dye that exhibits limited solubility in non-polar solvents and tends to exist as dispersed aggregates. The hydrophobic polysiloxane-modified AgNW/SiO_2 sponge readily interacts with these aggregates, enhancing the adsorption of MB through surface-mediated hydrophobic interactions. Consequently, the composite sponge exhibits superior equilibrium adsorption performance in low-concentration organic dye systems compared to the unmodified SiO_2 sponge.

The adsorption behavior of MB in the AgNW/SiO_2 sponge system can be understood in terms of interfacial interactions and solvent–solute dispersion thermodynamics. In non-polar solvents such as chloroform, MB exhibits poor solubility and tends to form molecular aggregates due to strong π–π stacking and intermolecular Coulombic interactions. These aggregated MB domains possess relatively high surface energy and thus preferentially interact with surfaces of lower polarity. The AgNW/SiO_2 sponge, modified by a polysiloxane-based low-surface-energy coating, provides hydrophobic microdomains that effectively adsorb MB aggregates through van der Waals and hydrophobic association forces.

In contrast, the pure SiO_2 sponge, with its intrinsically hydrophilic surface and high surface energy, has limited affinity for MB aggregates in chloroform, resulting in weaker adsorption performance. The presence of AgNWs further contributes to the adsorption process by increasing surface roughness and introducing additional nano-scale confinement regions, which facilitate MB capture via physical entrapment at the fiber–nanowire

junctions. This multi-scale roughness enables the sponge to maintain a Cassie–Baxter interfacial state, wherein partial air retention enhances the effective hydrophobic surface area available for adsorption.

However, in aqueous systems or in high-concentration dye-loaded chloroform, MB is more uniformly solvated, and the driving force for hydrophobic adsorption is significantly reduced. As a result, the AgNW/SiO_2 sponge exhibits limited adsorption efficiency under these conditions, consistent with the experimental observations. Therefore, the selective adsorption behavior arises from the cooperative effects of dye aggregation state, solvent polarity, interfacial free energy, and hierarchical surface topology.

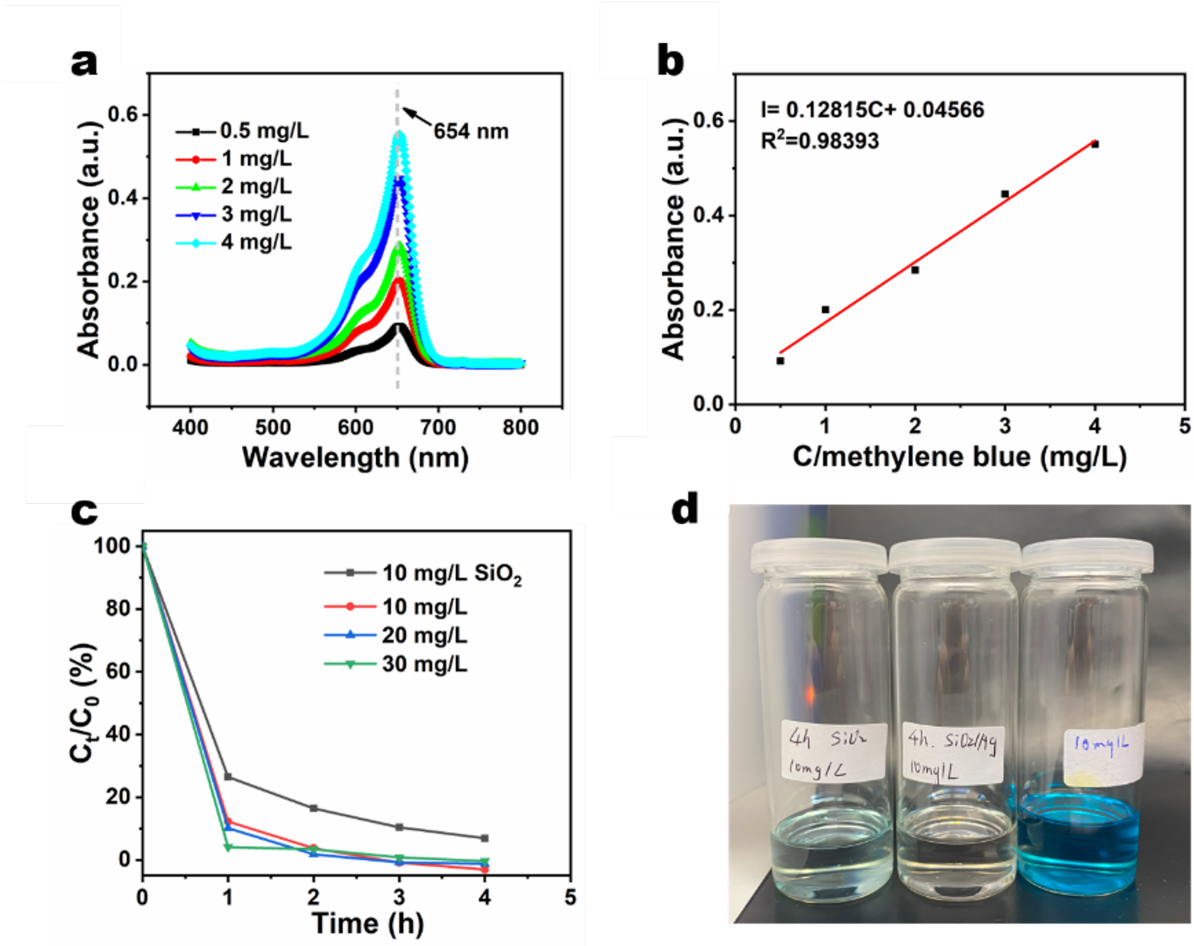

Figure 4.28: Quantification analysis of methylene blue content by a UV-vis spectrum. a. Standard curves in chloroform. b. The scattering plot of methylene blue in chloroform by UV-vis. c. The relationship between time and methylene blue residual. d. The photograph of a solution is taken after the dye absorption, From left to right: silica sponge, AgNW/SiO_2 sponge, and 10 mg/L MB solution.

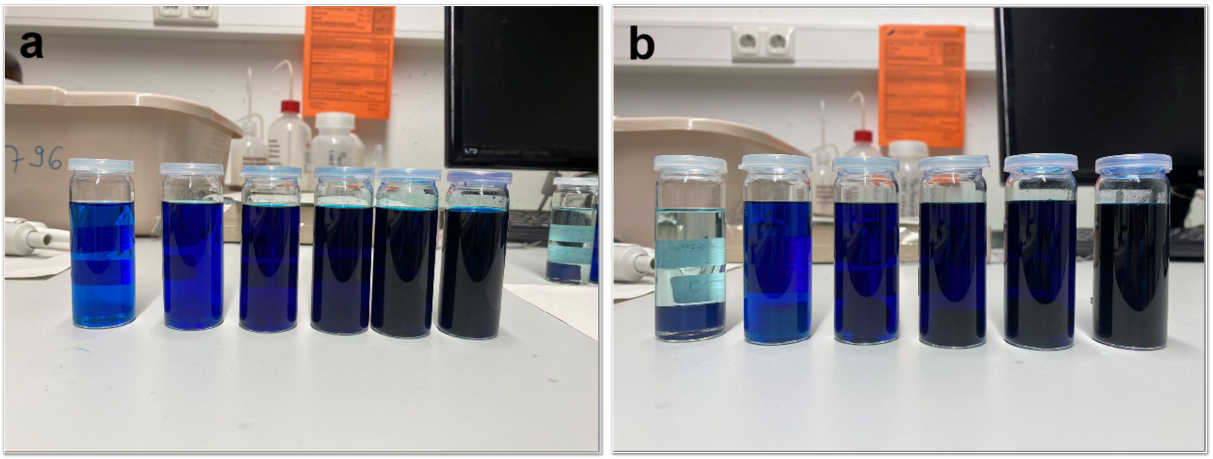

Figure 4.29: Photographs taken after dye adsorption at room temperature with dye concentrations of 30 mg/L, 50 mg/L, 100 mg/L, 200 mg/L, 300 mg/L, and 400 mg/L. a. SiO_2 sponge. b. AgNW/SiO_2 sponge.

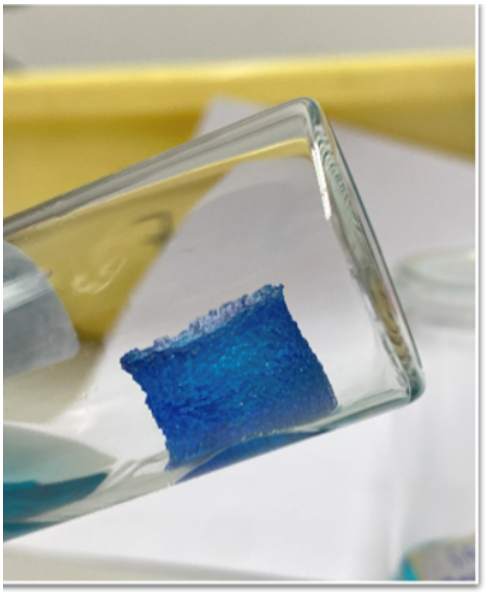

Figure 4.30: The SiO_2 sponge undergoes gelation when placed in the chloroform dye solution.

Silica sponges are prone to solvent-induced gelation (Figure 4.30). Chloroform, being a weakly polar to non-polar solvent, contains trace amounts of water that facilitate the formation of hydrogen bonds between silanol groups on the silica surface. These strengthened hydrogen-bonding interactions promote interparticle association among silica domains. As a result, molecular rearrangement occurs at the silica surface, leading to the aggregation of silica fibers into a three-dimensional interconnected network, thereby causing a gelation phenomenon [186].

In contrast, the incorporation of AgNWs in the AgNW/SiO_2 sponge inhibits this solvent-induced gelation process and preserves a high effective surface–solvent contact area for adsorption. This structural stability allows the AgNW/SiO_2 sponge to leverage interfacial

affinity to enhance MB adsorption capacity. Based on the preliminary structure–property characterization, a composite sponge with a 25% volume fraction of AgNWs was selected for detailed adsorption evaluation.

During the initial adsorption stage (first 2 h), a rapid decrease in MB concentration was observed, reflecting the availability of abundant accessible adsorption sites on the AgNW/SiO_2 surface. After 2 h, the AgNW/SiO_2 sponge effectively removed MB from the dye–chloroform mixture, resulting in a clear-to-colorless solution transition. In comparison, the pure SiO_2 sponge exhibited significantly weaker adsorption efficiency due to gelation-induced reduction of its effective contact area in chloroform, leaving visible residual dye in solution even after 4 h (Figure 4.31a).

After reaching adsorption equilibrium at 72 h, the AgNW/SiO_2 sponge demonstrated a maximum adsorption capacity of 84.8 $mg \cdot g^{-1}$ at an initial MB concentration of 30 $mg \cdot L^{-1}$, corresponding to a removal efficiency of 98.44% (Figure 4.28). Optical observations before and after adsorption (Figure 4.31c–d) further confirm the strong dye uptake capability of the composite sponge.

Taken together, these results demonstrate that the AgNW/SiO_2 sponge possesses both high dye-removal efficiency and structural robustness, positioning it as a promising material for solvent recovery and reuse in low-concentration dye–chloroform processing systems. Such performance offers practical benefits in improving resource utilization and mitigating environmental contamination.

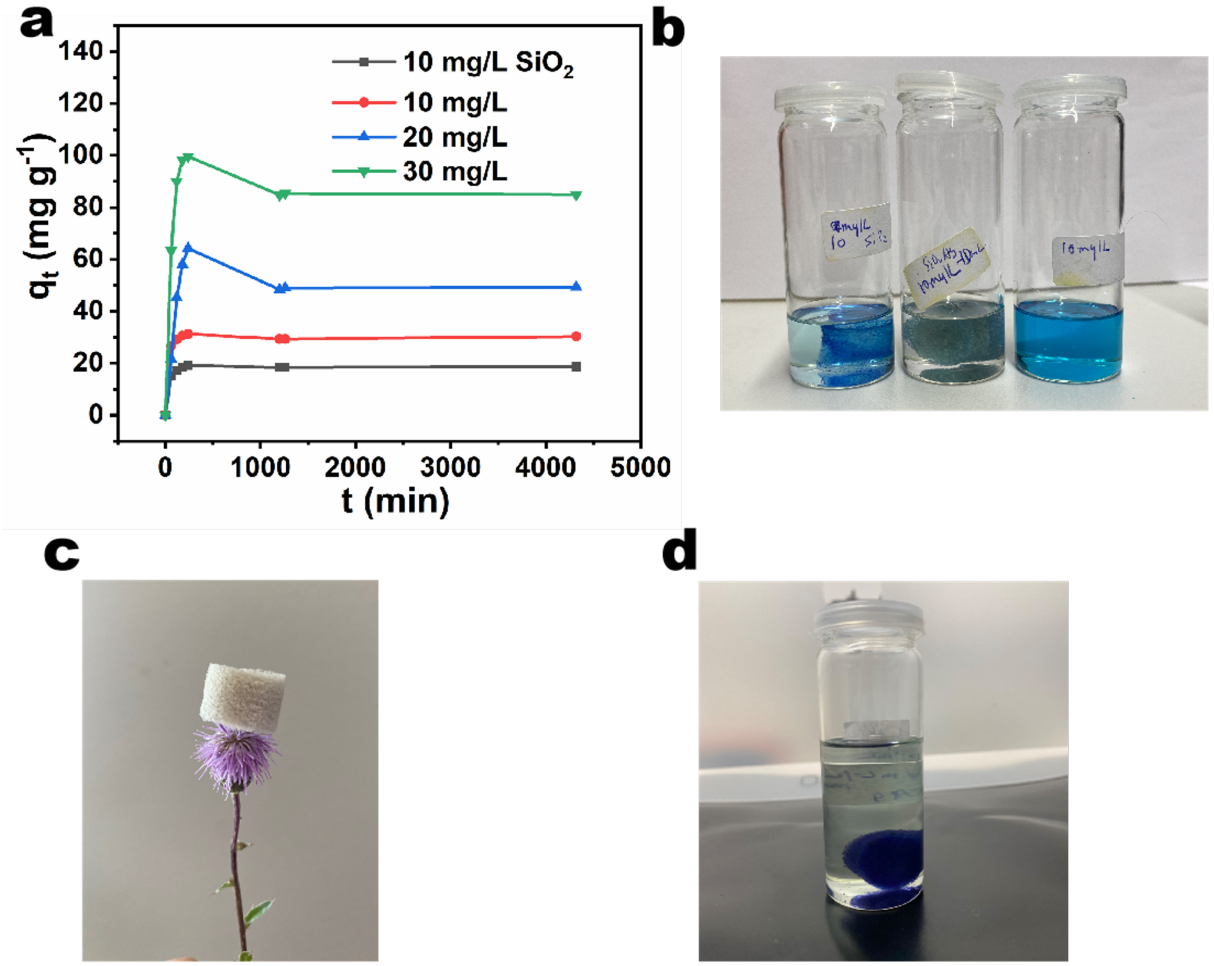

Figure 4.31: a. Adsorption of MB at different initial concentrations over time at room temperature. The curves from top to bottom correspond to the SiO_2 sponge in a 10 mg/mL MB solution, the AgNW/SiO_2 sponge in a 10 mg/mL MB solution, the AgNW/SiO_2 sponge in a 20 mg/mL MB solution, and the AgNW/SiO_2 sponge in a 30 mg/mL MB solution, respectively. b. Photographs of the sponges immersed in MB solutions. From left to right: SiO_2 sponge in 10 mg/mL MB solution, AgNW/SiO_2 sponge in 10 mg/mL MB solution, and the pure 10 mg/mL MB solution. c. The AgNW/SiO_2 sponge supported by a flower, highlighting its ultralight nature. d. Optical photograph of the sponge after MB adsorption, in comparison with the pristine sponge shown in (c).

The adsorption kinetics and thermodynamic behavior of MB on the sponge were further analyzed [187, 188]. The high correlation coefficients (R values) and the close agreement between the calculated and experimental equilibrium adsorption capacities indicate that the adsorption process follows a pseudo-second-order kinetic model (Figure 4.32b–c). This suggests that chemisorption is the rate-controlling step during adsorption (Table 1). The interaction between MB molecules and the AgNW/SiO_2 sponge is therefore governed not only by the dye concentration but also by intrinsic material properties, including surface energy, pore structure, specific surface area, and surface chemical characteristics. The number of available adsorption sites is inherently limited by the fixed specific

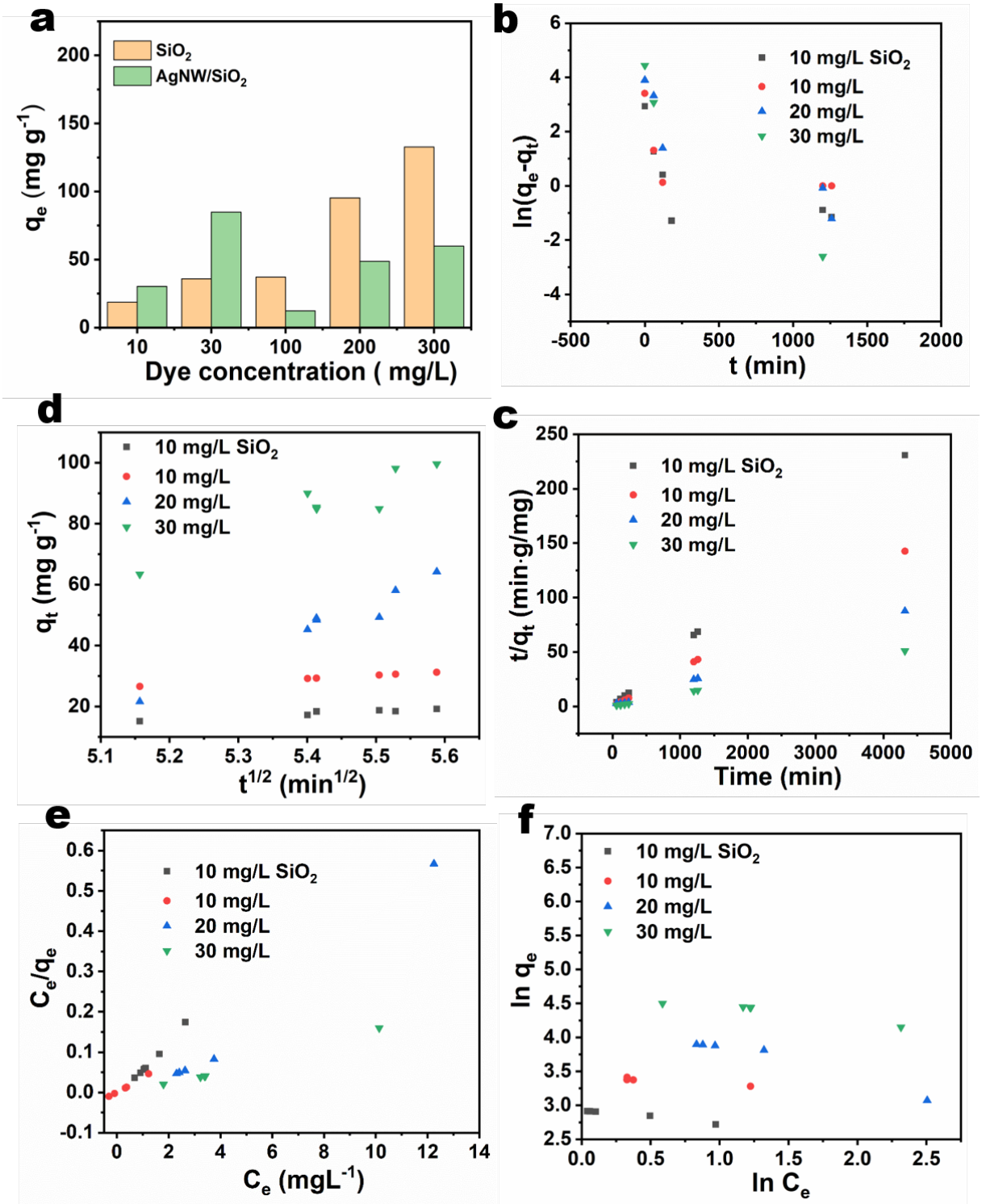

Figure 4.32: a. The maximum adsorption capacity of sponges with different concentrations was obtained from experiments (T: 298 K). b. Adsorption kinetics plot from Pseudo-first-order model. c. Adsorption kinetic plot from Pseudo-second-order model. d. Intraparticle diffusion. e. Thermodynamics fitting from Langmuir isotherms with MB adsorption on sponges. f. Thermodynamics fitting from Freundlich isotherms with MB adsorption on sponges.

surface area and the chemical functionality of the AgNW/SiO_2 sponge. Although the sponge possesses a highly porous structure, the total number of silica fibers and the corresponding effective surface area are constant. Likewise, the functional groups capable of interacting with MB—such as silanol groups (Si–OH), hydrophobic moieties from polysiloxane, and the surface interaction sites associated with AgNWs—do not increase with dye concentration. These groups govern hydrogen bonding, electrostatic attraction, hydrophobic association, and π–π interactions during adsorption. Once these active sites become progressively occupied by MB molecules, additional dye molecules cannot effectively bind, resulting in site saturation. This saturation behavior is consistent with the high adsorption efficiency observed at low MB concentrations and explains the gradual plateau in adsorption capacity at higher concentrations. This also implies finite number of available adsorption sites, consistent with the superior adsorption performance observed at low MB concentrations.

Furthermore, the enhanced interaction between the AgNW/SiO_2 sponge and MB can be attributed, in part, to the molecular structure and flexibility of the polysiloxane component. The polysiloxane backbone, composed of Si–O–Si bonds with a bond angle of approximately 140°, possesses greater rotational freedom than carbon-based chains, imparting high molecular flexibility. This flexibility allows the polymer chains to conform around the planar aromatic rings of MB, strengthening molecule–surface interactions. Additionally, the presence of hydrophobic methyl groups in polysiloxane facilitates hydrophobic association and π–π interactions with the aromatic system of MB, thereby promoting dye adsorption at the sponge surface.

Table 4.1: Parameters derived from pseudo-first-order and pseudo-second-order models for samples (T = 298 K).

samples	**pseudo-first-order**			**pseudo-second-order**		
	$q_{e,\mathrm{exp}}$	k_1	$q_{e,\mathrm{cal}}$	k_2	$q_{e,\mathrm{cal}}$	R^2
SiO_2 10 mg/L	18.72	-0.0019	3.047	90.455	18.70	0.99994
AgNW/SiO_2 10 mg/L	30.30	-0.0015	5.810	278.12	30.28	0.99982
AgNW/SiO_2 20 mg/L	49.30	-0.0031	22.26	339.90	49.36	0.99927
AgNW/SiO_2 30 mg/L	84.88	-0.0055	51.03	–	84.67	0.99987

Note: $q_{e,\mathrm{exp}}$ and $q_{e,\mathrm{cal}}$ are equilibrium adsorption capacities (mg g^{-1}); k_1 is the pseudo-first-order rate constant (min^{-1}, values are reported as $\times 10^3$); k_2 is the pseudo-second-order rate constant (g mg^{-1} min^{-1}, values are reported as $\times 10^{-5}$); R^2 is the coefficient of determination (dimensionless).

To further elucidate the adsorption mechanism, the intra-particle diffusion model was employed (Figure 4.32d and Table 2). At low MB concentrations, the kinetic curves exhibit a single linear region, indicating that adsorption is predominantly controlled by rapid boundary-layer diffusion. As the MB concentration increases, two distinct adsorption stages appear, and the emergence of the second diffusion rate constant ($k_{\mathrm{i},2}$) suggests that

intra-particle diffusion becomes a dominant rate-controlling step under these conditions. Additionally, the fact that the regression lines do not pass through the origin confirms that intra-particle diffusion is not the sole rate-determining mechanism, in agreement with the pseudo-second-order kinetic analysis.

Table 4.2: Parameters derived from Langmuir and Freundlich models for samples (T = 298 K).

samples	**langmuir**			**freundlich**		
	$q_{\max}$	K_L	R^2	$1/n$	K_F	R^2
SiO_2 10 mg/L	13.98	-4.125	0.99631	0.178	18.42	0.94997
AgNW/SiO_2 10 mg/L	29.74	–	0.99622	0.104	30.44	0.93501
AgNW/SiO_2 20 mg/L	24.11	-4.288	0.91263	0.503	78.73	0.96694
AgNW/SiO_2 30 mg/L	66.13	-4.37	0.97754	0.215	107.38	0.92966

Note: $q_{\max}$ is the maximum adsorption capacity (mg g^{-1}); K_L is the Langmuir constant (typically L mg^{-1}); K_F is the Freundlich constant (units depend on n, commonly (mg g^{-1})(L $mg^{-1})^{1/n}$); $1/n$ is dimensionless; R^2 is the coefficient of determination (dimensionless).

The adsorption isotherm data were further analyzed using the Langmuir and Freundlich models (Figure 4.32e–f and Table 3). The Freundlich isotherm provides a better fit, indicating that the adsorbent surface is heterogeneous and that multilayer adsorption occurs. The Freundlich constant K_{F} reflects the affinity between MB and the adsorbent; the larger K_{F} value for AgNW/SiO_2 compared with SiO_2 confirms that the incorporation of AgNWs significantly enhances surface affinity. The parameter n describes adsorption favorability, where a smaller $1/n$ corresponds to more favorable adsorption. The experimental results demonstrate that, under the studied conditions, the AgNW/SiO_2 sponge achieves a higher equilibrium adsorption capacity than the SiO_2 sponge, particularly at an MB concentration of 20 mg/L, highlighting its superior adsorption performance.

Table 4.3: Parameters derived from the two-stage intraparticle diffusion model for sponges with different MB concentrations (T = 298 K).

samples	**stage 1**			**stage 2**		
	R^2	$K_{i,1}$	C	R^2	$K_{i,2}$	C
SiO_2 10 mg/L	0.89517	9.222	–	–	–	–
AgNW/SiO_2 10 mg/L	0.99982	10.73	–	–	–	–
AgNW/SiO_2 20 mg/L	0.99989	98.63	–	0.76929	80.12	–
AgNW/SiO_2 30 mg/L	0.96953	86.54	–	0.72415	73.98	–

Note: $K_{i,1}$ and $K_{i,2}$ are intraparticle diffusion rate constants (mg g^{-1} $min^{-1/2}$); C is the intercept related to boundary layer thickness (mg g^{-1}); R^2 is the coefficient of determination (dimensionless).

4.2.4 CONCLUSION

In this chapter, nanowire–nanofiber structured AgNW/SiO_2 sponges were successfully fabricated, exhibiting high compressibility, ultralow thermal conductivity, and notable adsorption performance toward methylene blue at low concentrations. By integrating Ag nanowires and flexible SiO_2 nanofibers and encapsulating them within a polysiloxane network, a synergistic reinforcement was achieved, whereby the composite performance surpassed that of the individual components.

A representative cylindrical sponge with a mass of 15.22 mg and a volume of 5.55 cm^3 demonstrated a thermal conductivity of 0.024 $W\,m^{-1}\,K^{-1}$ at an Ag volume fraction of 25.0%. Furthermore, the sponge maintained excellent mechanical resilience, exhibiting only 9% residual plastic deformation after 100 compression cycles. The presence of Ag nanowires, interwoven with the fibrous SiO_2 scaffold, effectively prevented mechanical degradation associated with uneven nanowire distribution.

During the liquid-to-solid transition, the formation of a uniform polysiloxane coating served as an *in situ* binding phase, improving interfacial compatibility between AgNWs and SiO_2 fibers. The transition from hydrophilic to hydrophobic wetting behavior was attributed to both increased surface roughness introduced by AgNWs and the evolution of surface functional groups resulting from siloxane hydrolysis and condensation reactions.

The AgNW/SiO_2 sponge also exhibited high adsorption efficiency for methylene blue in chloroform under static conditions at room temperature, achieving a removal rate of up to 98.44% at low dye concentrations.

Overall, these results provide a fundamental strategy for regulating the spatial distribution of metal nanowires within three-dimensional fibrous networks and highlights the resulting influence on composite mechanical, thermal, and interfacial properties. The developed AgNW/SiO_2 sponges show strong potential in applications such as thermal insulation, organic dye remediation, and multifunctional porous material systems.

4.3 1D PT-DOPED WITH POLYVINYLPYRROLIDONE SUPPORTED SHAPE-CONTROLLED PTAGNT NANOSTRUCTURES AS AN EXCELLENT CATALYST FOR DIRECT METHANOL FUEL CELL

Extending the functional applications of AgNWs represents another important focus of this chapter. During AgNW synthesis, PVP acts as a key complexing and capping agent that directs the anisotropic growth of silver from nanoparticles into nanowires, thereby drawing considerable attention in nanostructure-controlled synthesis [85]. Beyond its role in AgNW formation, PVP also strongly influences subsequent structural evolution in Ag-based alloyed nanomaterials. For instance, in PtAg alloy systems, PVP regulates the morphology and stability of alloy nanostructures synthesized with AgNWs as sacrificial templates.

PtAg nanoalloys have been widely studied for catalytic applications, including methanol, ethanol, and formic acid electro-oxidation. The scarcity and high cost of Pt, coupled with catalyst deactivation during operation, have motivated the development of Pt-based alloys. Compared with pure Pt, PtAg alloys typically exhibit enhanced catalytic activity and stability, which can be attributed to the synergistic effects arising from both electronic and geometric modifications. Electron transfer from Ag (with lower electronegativity) to Pt results in modulation of the Pt d-band vacancies, while lattice strain introduced by alloy formation modifies orbital overlap. Together, these factors lower the Pt d-band center, thereby weakening the adsorption strength of reaction intermediates and improving catalytic performance.

PtAg nanostructures are generally synthesized under kinetically controlled conditions in colloidal systems containing metal precursors and surfactants. The formation dynamics are strongly influenced by metal–ligand complexation, where surfactants adsorb on growing metal surfaces to modulate surface energy and thermodynamic shape distribution. However, the complexity of these interactions has made it challenging to quantitatively evaluate the role of ligands in nucleation and growth mechanisms.

PtAg nanowires are typically synthesized via two main routes, including a one-step hydrothermal co-reduction of Pt and Ag precursors driven by an autocatalytic surface-coupled growth mechanism, or a two-step strategy based on galvanic replacement or electrochemical deposition using AgNWs as sacrificial templates. In the latter, PVP acts not only as a steric stabilizer that maintains the nanowire morphology, but its π–π coordination interactions also promote ordered alloying, enhancing catalytic activity.

Previous studies also highlight the influence of PVP in stabilizing noble metal catalysts. For example, Xia *et al.* demonstrated that PVP aging significantly affects the catalytic durability of Pd nanoparticles, while Huang *et al.* reported that PdAg nanomaterials anchored to nanotubular substrates exhibit excellent electrocatalytic performance toward methanol oxidation.

In this chapter, relatively thick AgNWs were selected as structural templates to provide sufficient spatial volume for Pt nucleation and deposition. Ethylene glycol (EG) was used as a reducing agent to partially reduce Pt precursors, enabling PtNPs to nucleate and grow on the AgNW surface. By regulating the PVP concentration, the interfacial deposition kinetics of Pt were precisely controlled, allowing tunable Pt particle size or PtAg alloy distribution on the nanowires and thus optimizing electrocatalytic activity.

4.3.1 SCHEMATIC ILLUSTRATION OF THE EXPERIMENTAL DESIGN WITH THE NANOSTRURE CONSTRUCTION PROCESS

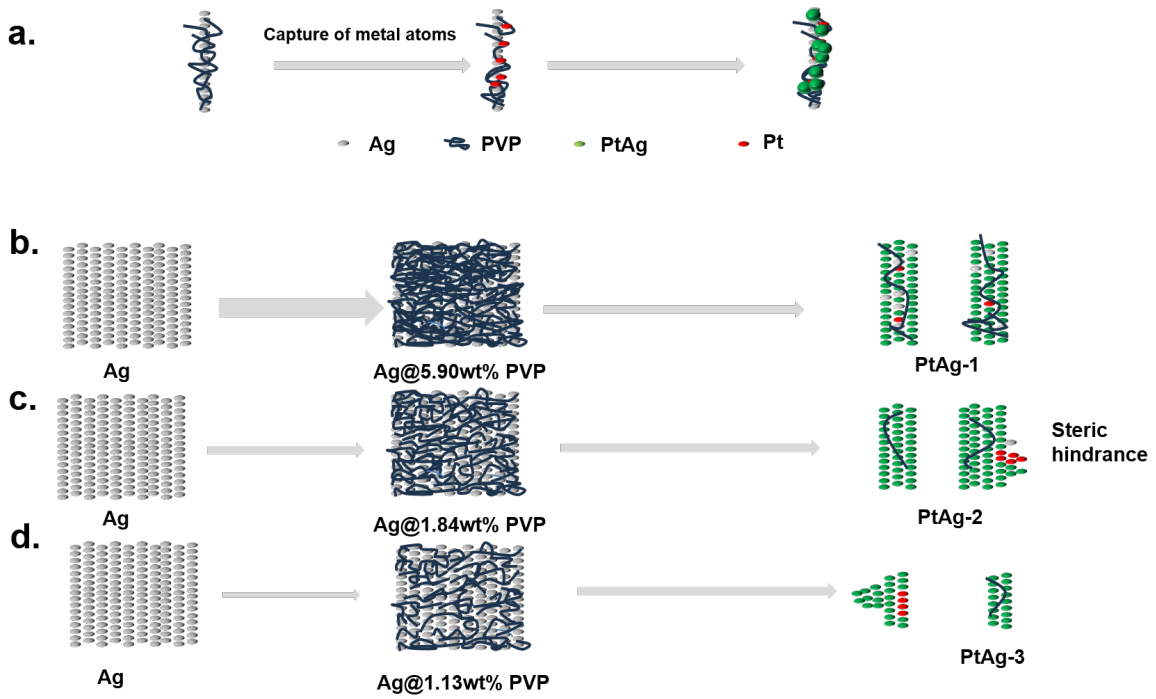

Figure 4.33: The schematic diagram of the synthesis of PtAg nanotubes. a. Atomic arrangement and PVP distribution on the outermost layer of AgNWs and formation of alloys on the surface. b.The cross-sectional nanostructure of PtAg nanotubes with the PVP content is 5.90%. c. The cross-sectional nanostructure of PtAg nanotubes with the PVP content is 1.80%. d. The cross-sectional nanostructure of PtAg nanotubes with the PVP content is 1.13%.

Figure 4.33 illustrates the formation process of PtAgNTs, which are synthesized via a galvanic replacement-type reaction between the Pt^{4+} precursor and pre-synthesized Ag nanowires in a polyol system. In this preparation, the only intentional variable is the concentration of PVP (Mw = 1,300,000), which serves as a surface capping ligand. The amount of residual PVP on AgNWs plays a crucial role in regulating the final PtAgNT morphology, and consequently influences the electrocatalytic performance.

To quantitatively determine the residual PVP content on AgNWs prior to alloy formation, thermogravimetric analysis (TGA) was conducted over a temperature range from room temperature to 800 °C (Figure 4.34), covering the characteristic thermal decomposition region of PVP. The TGA profile of pure PVP shows three well-recognized weight-loss stages: an initial 8.02% loss below 250 °C corresponding to the release of physically adsorbed water and low-molecular-weight oligomers; a subsequent 12.35% loss between 250 and 396 °C associated with partial chain cleavage; and a major 79.63% decomposition from 396 to 695 °C attributed to breakdown of the polymer backbone.

Based on the corresponding mass-loss region (250–650 °C) in the TGA curves of AgNWs, the estimated residual PVP contents on the nanowire surface were determined to be 5.90%, 1.84%, and 1.13% for the respective samples. These results confirm that the amount of PVP retained on AgNWs varies systematically with the PVP concentration used during synthesis, providing a controllable parameter for tuning Pt deposition behavior and the structural evolution of PtAgNTs.

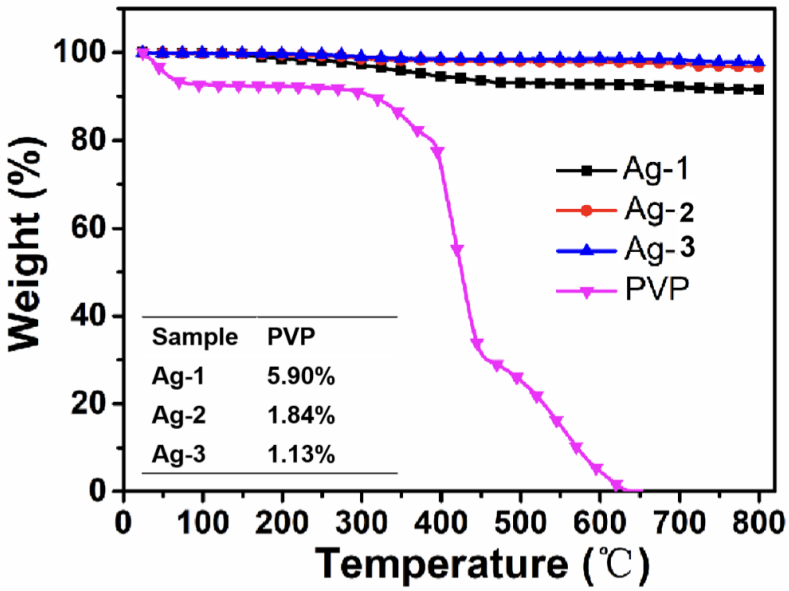

Figure 4.34: TGA analysis of an Ag and a pure PVP. From 24 to 800 degrees at 10 ml/min in the air atmosphere. The insert table is the residual PVP on the AgNWs.

The reaction among $PtCl_6^{2-}$, AgNWs, and ethylene glycol follows a galvanic replacement pathway for the synthesis of Pt-based nanoshells. Typically, the Pt shell is formed by introducing an H_2PtCl_6 solution into a dispersion of AgNWs at a mild temperature of approximately 100 °C. In this process, Ag atoms from the nanowire template are oxidized by $PtCl_6^{2-}$, while Pt^{4+} is reduced to Pt^0. In the presence of a capping ligand such as PVP, the generated Pt atoms are confined near the nanowire surface, where they nucleate and grow into nanoparticles, ultimately forming a continuous nanoshell retaining the wire-like morphology. Simultaneously, the Ag atoms from the template diffuse outward into the bulk solution as Ag^+, while the Pt nanoshell remains as a structural replica of the original AgNW template. Overall, this template-mediated galvanic replacement process can be divided into two sequential stages. First, Ag is oxidized and Pt is epitaxially deposited on the AgNW surface, forming a Pt–Ag alloy layer due to interdiffusion between the two metals. In the second stage, selective dealloying of Ag occurs, producing structural remodeling of the alloy wall and the formation of nanoscale pinholes, ultimately yielding hollow PtAg nanotubes.

In the absence of capping ligands such as PVP, direct addition of H_2PtCl_6 leads to rapid internal corrosion of the AgNWs, generating hollow interiors surrounded by alloyed Pt–Ag shells. As the reaction proceeds, openings form along the nanotube sidewalls to facilitate mass transport of $PtCl_6^{2-}$, Ag^+, and Cl^- species, resulting in characteristic hollow nanotube structures [134, 189–193].

The influence of PVP on nanotube morphology is particularly significant. As the Pt precursor concentration increases, Ag is progressively consumed. Based on the reaction stoichiometry, four Ag atoms are oxidized for each Pt atom formed:

$$4\,Ag + [PtCl_6]^{2-} \rightarrow Pt + 4Ag^+ + 6Cl^-$$

This results in lattice vacancy formation. To relieve the accumulated structural strain, the nanotubes undergo surface reorganization via Ostwald ripening, and excessive depletion of Ag ultimately leads to structural collapse into fragmented Pt-rich debris—an undesirable outcome with low Pt utilization efficiency.

4.3.2 MORPHOLOGY AND STRUCTURE OF PTAG NANOTUBES

In this chapter, variation in PVP content on AgNW templates leads to observable morphological differences in PtAg nanotubes. SEM imaging confirms the successful formation of hollow PtAgNTs across all samples. For PtAg-3, localized aggregation of larger particles is observed along one side of the nanotube surface. This phenomenon can be attributed to

reduced PVP coverage on the AgNWs, which decreases the number of surface anchoring sites available for controlled Pt nucleation, leading to uncontrolled growth and particle coalescence in the ethylene glycol medium.

In contrast, PtAgNTs synthesized with higher PVP coverage (e.g., PtAg-1 and PtAg-2) exhibit smaller and more uniformly distributed particles. The increased steric stabilization provided by PVP imposes growth confinement at the nanowire interface, effectively restricting particle coarsening and resulting in finer structural features (Figure 4.35).

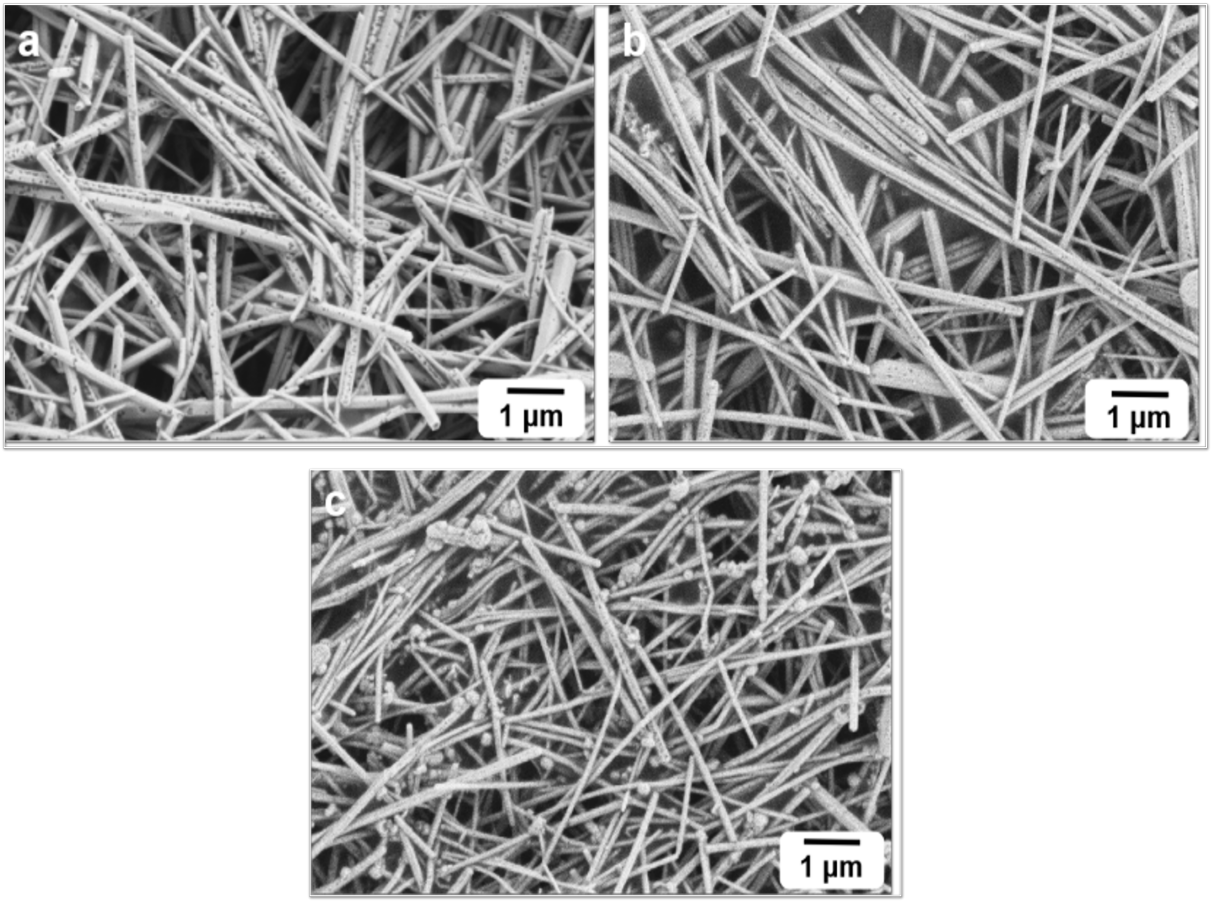

Figure 4.35: SEM images of PtAg catalysts synthesized with different amounts of PVP: a. PtAg-1, b. PtAg-2, and c. PtAg-3, demonstrating the influence of PVP content on the resulting nanotube morphology.

TEM was employed to further analyze the surface structure of the PtAg nanotubes and to elucidate the influence of residual PVP. As shown in Figure 4.36, the overall hollow tubular morphology is preserved in all three samples (PtAg-1, PtAg-2, and PtAg-3) (Figures 4.36a, 4.36d, and 4.36g). Notably, the average tube length decreases progressively from PtAg-1 to PtAg-3 as the residual PVP content decreases, suggesting that PVP contributes to maintaining structural integrity during galvanic replacement. Closer examination of the nanotube walls reveals distinct differences in porosity and surface roughness among the samples. PtAg-1 exhibits well-defined and relatively large pores on the tube walls (Figure 4.36b), indicating a more extensive dealloying process. In contrast, PtAg-2 and PtAg-

3 display smaller and fewer pores (Figures 4.36e and 4.36h), reflecting a slower or less complete dealloying process in PtAgNTs. Correspondingly, PtAg-1 possesses the greatest wall thickness, while PtAg-3 exhibits the thinnest walls. These differences are attributed to the variation in PVP coverage: higher PVP content can selectively adsorb to specific crystal facets, modulating atomic diffusion and growth kinetics, thus affecting both wall thickness and pore evolution.

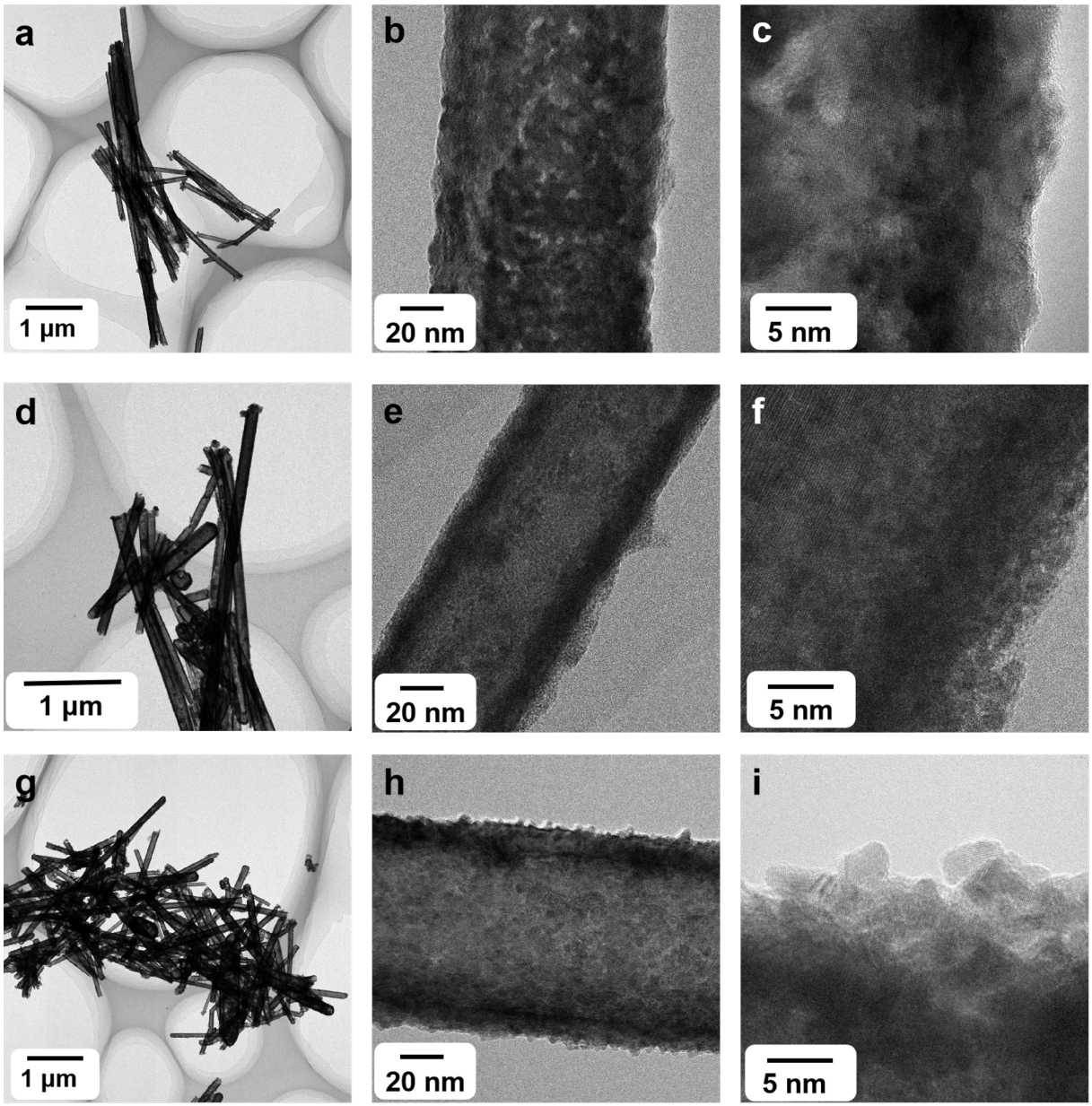

Figure 4.36: TEM images of AgNWs reacted with H_2PtCl_6 under different PVP mass ratios: a–c. 5.90% PVP, d–f. 1.84% PVP, and g–i. 1.13% PVP. These images further reveal the effect of residual PVP content on the surface structure of the PtAg nanotubes.

Surface morphology further differentiates the samples. PtAg-1 displays the roughest tube surface, whereas PtAg-2 shows the smoothest and most uniform shell. In PtAg-3, noticeable nanoparticle aggregation is observed on the tube surface (Figures 4.36c, 4.36f, and

4.36i). The larger particle size in PtAg-3 can be attributed to insufficient PVP coverage, resulting in reduced steric hindrance during nucleation and growth, which promotes particle coalescence. In contrast, PtAg-2 maintains a balanced PVP level that effectively stabilizes metal atoms during alloying, yielding a more homogeneous surface.

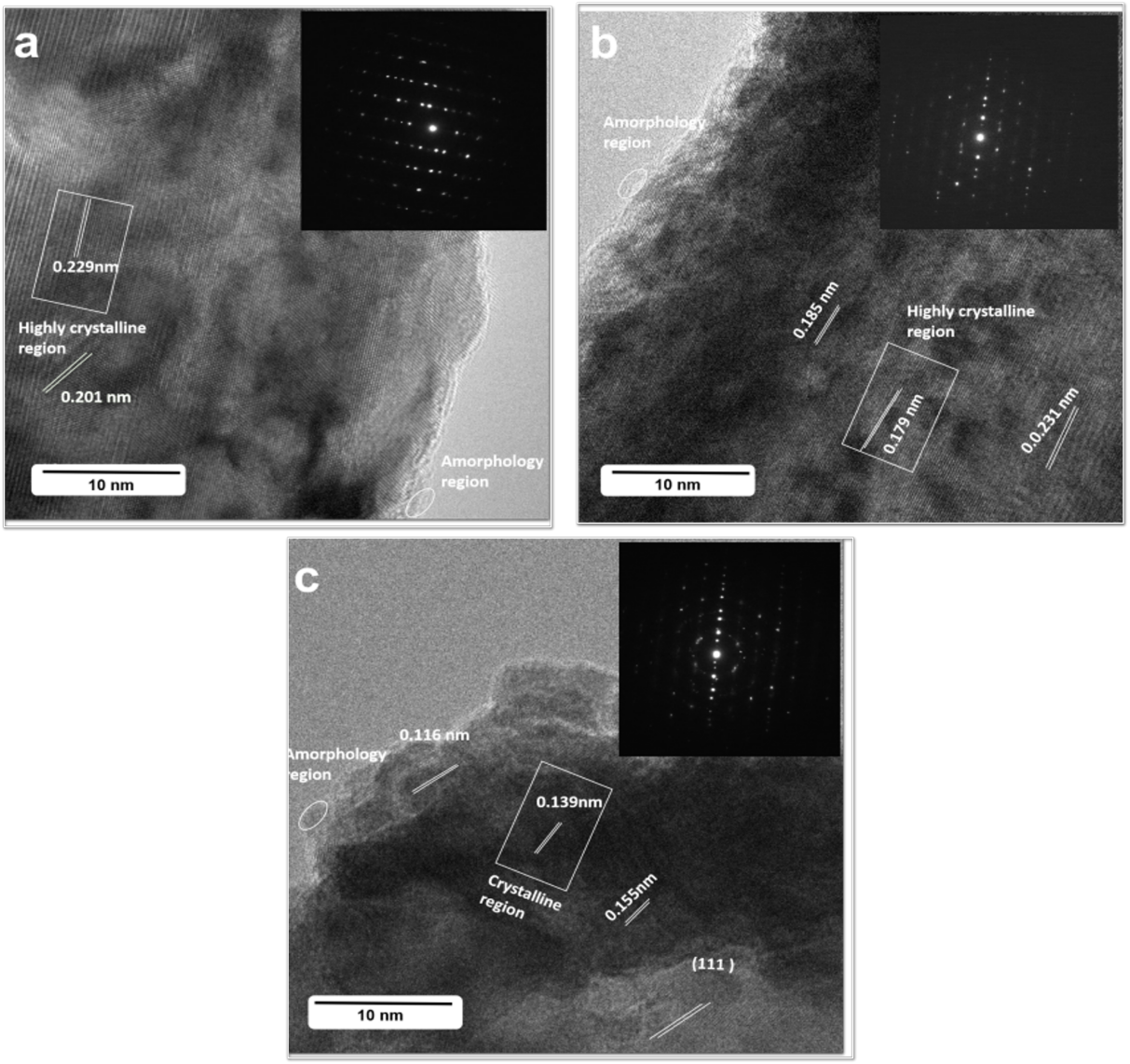

Figure 4.37: STEM images of a. PtAg-1, b. PtAg-2, and c. PtAg-3, with the corresponding SAED patterns shown in the insets, where the difference in atomic mobility between Pt and Ag results in a periodically ordered electron diffraction pattern.

High-resolution transmission electron microscopy (HRTEM) was further conducted to investigate the crystal structure of the PtAg nanotubes. As shown in Figure 4.37a–c, clear lattice fringes corresponding to the (111) plane of a face-centered cubic (FCC) metal structure are observed. Given that Ag and Pt share similar FCC lattice parameters, the formation of PtAg nanotubes proceeds through a crystallographically aligned (111) oriented growth mode. In the PtAg-1 sample, well-defined lattice fringes with continuous periodicity indicate high crystallinity and a relatively low density of lattice defects. For

PtAg-2, the nanotube walls also exhibit strong crystalline ordering without noticeable nanoparticle aggregation on the surface, suggesting an optimized growth environment. In contrast, PtAg-3 displays localized nanoparticle accumulation on the nanotube walls. This morphology likely arises from the surface-protection effect of PVP, allowing uncontrolled nucleation followed by coalescence, ultimately generating interfacial strain. In this case, the system minimizes interfacial mismatch energy through the formation of curved or partially reconstructed tube morphologies.

The corresponding selected-area electron diffraction (SAED) patterns inserted in Figure 4.37 reveal superlattice diffraction rings/spots. These superlattice patterns originate from the ordered distribution of Pt and Ag atoms within the alloy lattice, where alternating occupancy of lattice sites produces periodic modulation in electron scattering. The formation of superlattice ordering may be attributed to the difference in atomic mobility between Pt and Ag during alloying. Silver, with its lower atomic mass (107.87 g/mol) and slightly larger atomic radius (0.144 nm), exhibits a higher diffusion rate compared to platinum (195.08 g/mol; 0.139 nm). Consequently, Ag atoms diffuse outward more rapidly than Pt during the galvanic replacement and dealloying stages, enabling alternating deposition of Pt and Ag. This dynamic redistribution process contributes to the formation of superlattice-ordered PtAg alloy domains.

The CIF file of Ag0.91Pt0.9 was obtained from the International Crystal Structure Database, and the corresponding XRD pattern was simulated using FullProf for comparison with the experimentally measured diffraction spectra. This allowed the identification and assignment of characteristic diffraction peaks. Since PtAg crystallizes in a face-centered cubic (FCC) structure, Lebail fitting is typically sufficient for extracting lattice and crystal plane information. However, in this work, the primary objective was to investigate the effect of residual PVP on the crystallographic orientation during alloy formation. The complexation and preferential surface adsorption of PVP can induce oriented growth, which may suppress or enhance the development of specific crystal facets. Therefore, the Lebail refinement was applied to analyze the extent to which PVP influences plane-dependent growth behavior and to determine the critical PVP content beyond which preferential orientation becomes significant. As shown in Figure 4.38, the differences between Y_{obs} and Y_{calc} are mainly reflected in peak intensities rather than peak positions. Under identical crystal symmetry conditions, peak intensities are predominantly governed by the structure factor, multiplicity factor, absorption factor, thermal vibration factor, and the number of coherent diffracting unit cells along a specific crystallographic direction. Given that the first four contributions remain essentially constant among the samples, variations in peak intensity indicate differences in the number of coherently aligned unit cells, which correspond to different effective thicknesses of the same crystal plane. This directly reflects the plane-selective adsorption behavior of PVP during growth. Across the PtAg-1, PtAg-2,

and PtAg-3 samples, the intensity of the (111) diffraction peak at 17.30–17.40° decreases progressively. This trend suggests that decreasing PVP coverage on the Ag nanowire template weakens the facet-selective adsorption, thereby reducing the preferential growth and thickness of the (111) crystal plane. In contrast, when the PVP content is sufficient (PtAg-1), stronger selective adsorption stabilizes the (111) plane, leading to enhanced peak intensity. In addition to the dominant (111) reflection, diffraction peaks corresponding to the (200), (220), (311), (222), (400), (331), and (420) planes are also observed at 20.00–20.13°, 28.44–28.62°, 33.48–33.69°, 35.02–35.24°, 40.65–40.91°, 44.49–44.77°, and 45.71–46.00°, respectively, further confirming the FCC alloyed nanocrystalline structure of the PtAg nanotubes.

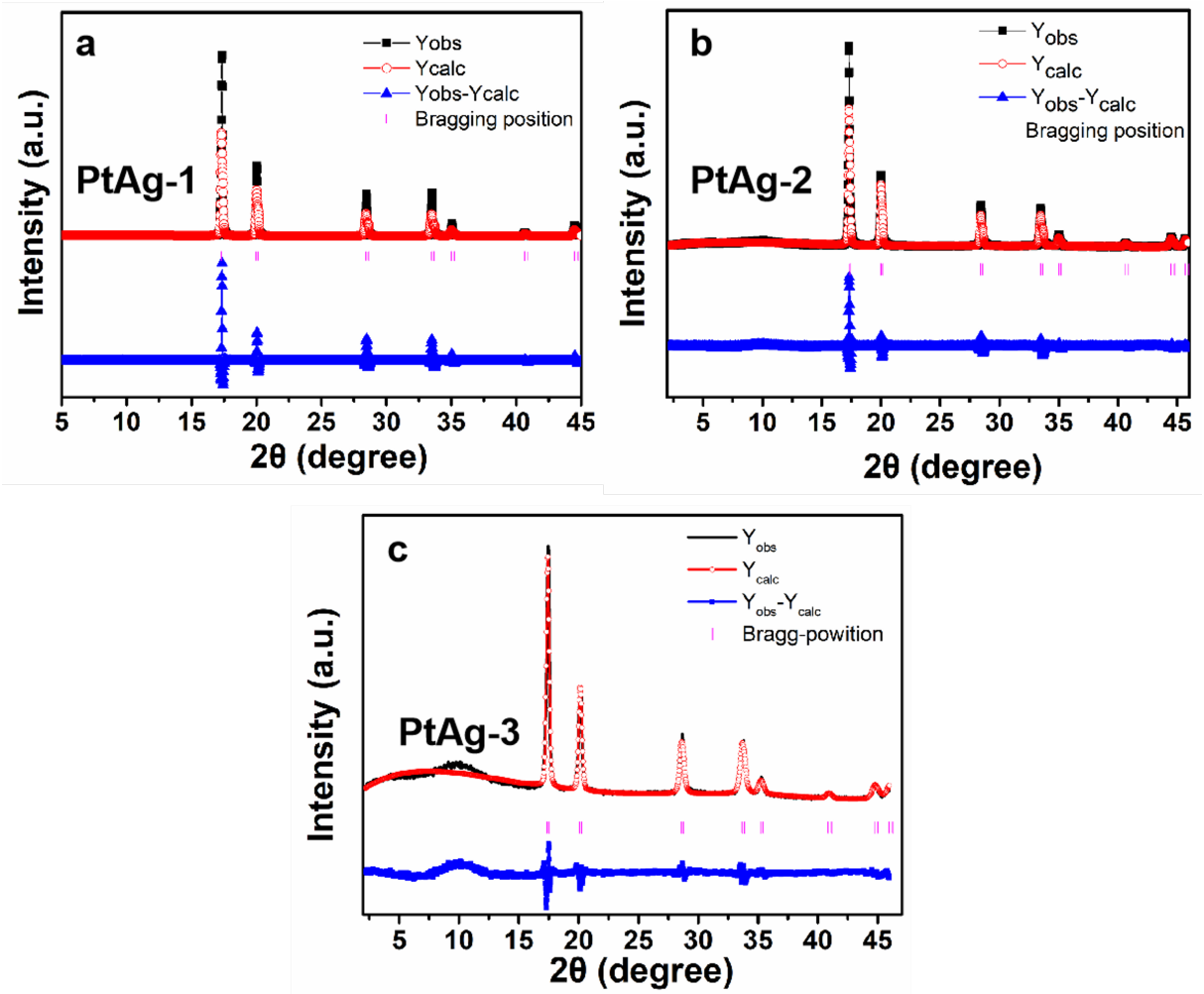

Figure 4.38: XRD diffraction patterns of a. PtAg-1, b. PtAg-2, and c. PtAg-3, highlighting the characteristic diffraction peak positions.

The elemental distribution of the synthesized PtAg nanotubes was investigated using EDS mapping and line-scan analysis. As shown in Figure 4.39b–c, f–i, and j–k, the spatial distributions of Pt and Ag differ among the three samples. For PtAg-1, a comparison between regions b-1 and c-1 reveals that Ag is enriched in areas where Pt is relatively deficient on the nanotube surface. This may be due to sequential deposition during galvanic

replacement or the retention of Ag within the template core caused by PVP encapsulation, which hinders Ag dissolution into the solution. In contrast, regions b-2 and c-2 display largely overlapping Pt and Ag signals, indicating alloy formation on the tube wall. In PtAg-2, Pt and Ag exhibit a largely co-localized distribution on the nanotube surface; however, localized variations are still observed. Regions f-1 and g-1, as well as f-2 and g-2, show discrete Pt- and Ag-rich domains, suggesting that alloying and surface particle deposition occur simultaneously, producing a more compositionally homogeneous nanotube compared to PtAg-1. For PtAg-3, both overlapping and complementary Pt/Ag distributions are observed. Regions j-1 and k-1 show Pt–Ag co-localization, while regions j-2 and k-2 exhibit complementary segregation, forming a continuous tubular structure with apparent compositional gradients. Based on these mapping results, PtAg-2 demonstrates the most uniform elemental distribution among the three samples. To further examine compositional uniformity along individual nanotubes, EDS line-scanning was performed. In PtAg-1 and PtAg-3, the Ag signal intensity is consistently higher than that of Pt along the tube length, whereas PtAg-2 exhibits comparable signal intensities for both elements, supporting a more homogeneous alloy formation. Under an accelerating voltage of 200 kV, the electron beam can penetrate nanotubes with thicknesses of 120–140 nm, enabling depth-averaged compositional detection. Based on the corresponding intensity profiles (Figure 4.39d, 4.39h, and 4.39i), the estimated shell thicknesses of PtAg-1, PtAg-2, and PtAg-3 are approximately 28.4 nm, 28.7 nm, and 19.3 nm, respectively.

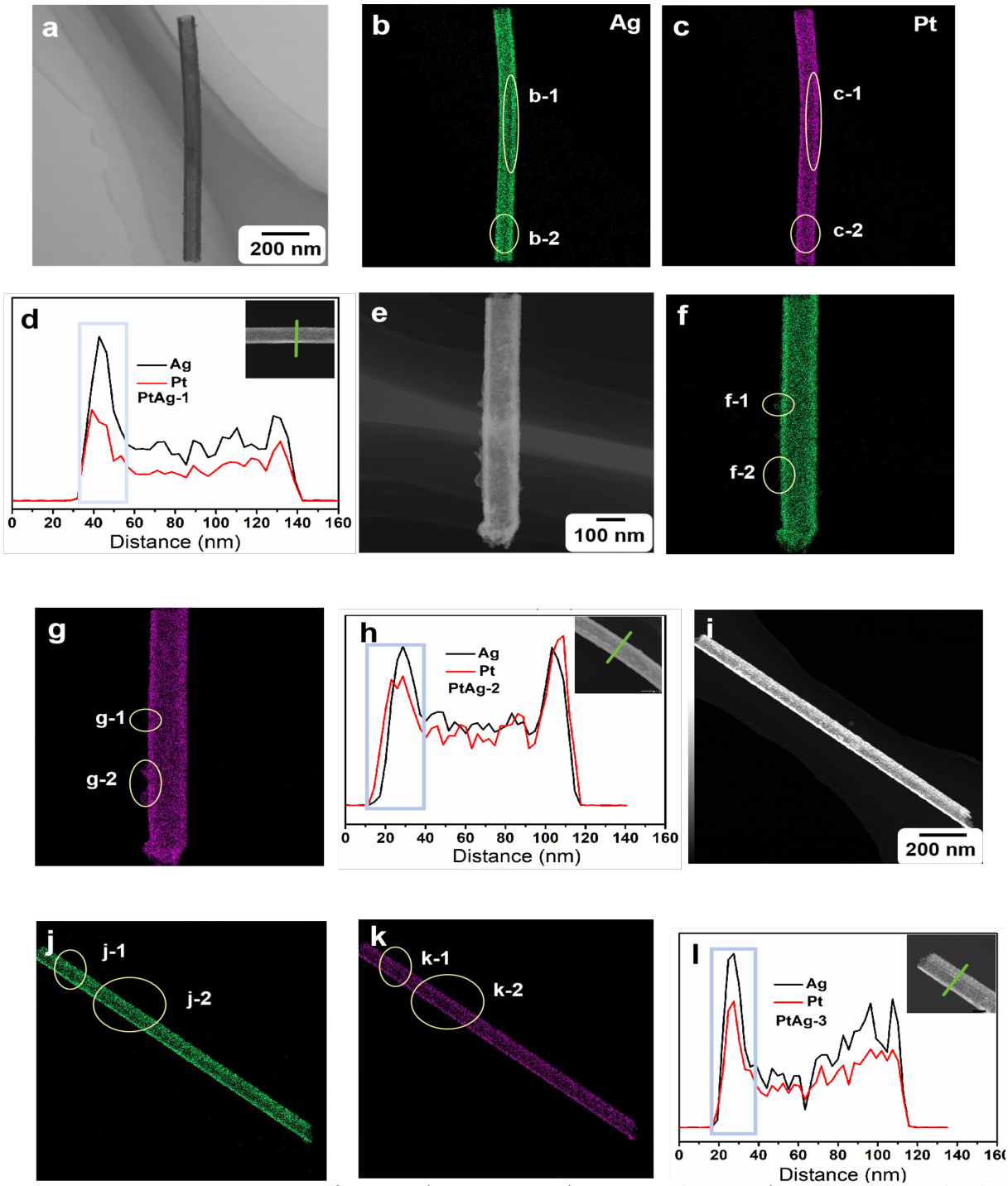

Figure 4.39: TEM images of a. PtAg-1, e. PtAg-2 , and i. PtAg-3, along with the corresponding EDS elemental mapping images (b-c,f-g, and j-k) and EDS line scanning profiles along the green line shown in the inset images of d. PtAg-1, h. PtAg-2 , and i. PtAg-3. The highlighted by boxes in the figures were used for the analysis of nanotube thickness.

To supplement the localized compositional information obtained from EDX line-scanning, the overall Pt–Ag content in the catalysts was quantified using ICP–OES (Table 4.4). The mass ratios of Ag to Pt in PtAg-1, PtAg-2, and PtAg-3 were determined to be 91.1:8.9, 93.3:6.68, and 91.2:8.8, respectively. Furthermore, the utilization efficiencies

of Ag and Pt were calculated by comparing the amount of metal incorporated into the final products with that present in the initial precursors. The utilization rates of Ag and Pt were 24.29% and 0.078% (PtAg-1), 24.88% and 0.058% (PtAg-2), and 24.32% and 0.077% (PtAg-3), respectively. These results indicate that while Ag incorporation into the nanotube structure is relatively consistent across samples, the utilization efficiency of Pt is extremely low. This suggests that a considerable fraction of Pt remains in the reaction solution and does not participate in alloy formation. The loss of Pt may be attributed to incomplete surface nucleation, insufficient ligand coordination, or the formation of Pt-containing debris that does not deposit onto the nanowire template.

Table 4.4: Variation in platinum and silver mass and their utilization rates.

sample	M_{AgNWs}	M_{Pt}	M_{PtAg}	W_{Ag}	W_{Pt}	U_{Ag}	U_{Pt}
PtAg-1	11.25	3.43	3.0 ± 0.3	91.1	8.9	24.29	0.078
PtAg-2	11.25	3.43	3.0 ± 0.3	93.3	6.68	24.88	0.058
PtAg-3	11.25	3.43	3.0 ± 0.3	91.2	8.8	24.32	0.077

Note: M_{AgNWs} is the mass of AgNWs used as templates (mg); M_{Pt} is the mass of platinum in precursor solutions (mg); M_{PtAg} is the mass of the obtained alloy (mg); W_{Ag} and W_{Pt} are the mass percentages of silver and platinum, respectively (%); U_{Ag} and U_{Pt} are the utilization rates of silver and platinum, respectively (%).

To investigate the origin of the enhanced catalytic activity of the PtAg nanotubes, the electronic structures were examined using X-ray photoelectron spectroscopy (XPS). The spectra clearly display characteristic Pt and Ag signals, confirming the formation of a bimetallic Pt–Ag nanostructure. For the Pt 4f7/2 state, a pronounced red shift from 71.4 to 70.7 eV ($\Delta E = -0.7$ eV) is observed for PtAg-1, PtAg-2, and PtAg-3 compared with pure Pt, indicating an increase in electron density at Pt sites. This electron enrichment arises from interfacial charge transfer from Ag to Pt as well as ligand coordination effects originating from residual PVP. In contrast, the Ag 3d5/2 peak shows only a slight shift (368.2 $\rightarrow$ 368.1 eV, $\Delta E = -0.1$ eV), which falls within typical instrumental uncertainty (0.05–0.2 eV), suggesting that Ag does not undergo significant charge accumulation. Furthermore, the $Pt(OH)_2$ component within the Pt 4f region exhibits a gradual red shift (72.5 $\rightarrow$ 72.4 $\rightarrow$ 72.3 eV from PtAg-1 to PtAg-3), which indicates preferential coordination of PVP to hydroxylated Pt sites and a progressively enhanced final-state screening effect as the PVP content decreases. These results collectively demonstrate that electron redistribution occurs predominantly at Pt sites, while PVP modulates both the extent of reduction and interfacial electronic coupling rather than acting as a direct electron donor to both metals. Importantly, these XPS observations are consistent with the compositional data obtained from ICP–OES and EDX. Although the Pt content differs slightly among PtAg-1, PtAg-2, and PtAg-3, the direction and magnitude of the Pt 4f shift correlate more strongly with the extent of electronic interaction than with the absolute Pt/Ag ratio. In

particular, PtAg-2, which previously demonstrated the most uniform Pt–Ag elemental distribution, exhibits the most pronounced electronic coupling signature—consistent with optimal alloying and interfacial charge transfer. This confirms that structural homogeneity rather than Pt quantity is the dominant factor in tuning the electronic state. The increased electron density on Pt induces partial filling of the Pt 5d band, leading to a downward shift of the d-band center. A weakened d-band center reduces the adsorption strength of CO_{ad}, thereby improving CO tolerance and enhancing catalytic performance. Thus, the synergy between Ag→Pt electron transfer, PVP coordination, and uniform alloy microstructure collectively underlies the superior electrocatalytic activity of PtAg nanotubes.

Table 4.5: Summary of X-ray photoelectron spectroscopy (XPS) measurement results.

sample	**Ag $3d_{5/2}$**	**Pt $4f_{7/2}$**	**Ag**	**Pt**	**Ag/Pt**
Ag	368.2	–	100	0	1:0
PtAg-1	368.1	70.7	7.8	8.0	0.98:1
PtAg-2	368.0	70.7	4.2	7.3	0.58:1
PtAg-3	368.1	70.7	11.8	14.7	0.80:1
Pt	–	71.4	0	100	0:1

Note: Binding energies are given in eV; atomic concentrations are given in at%; Ag/Pt denotes the atomic ratio of silver to platinum (at/at). All binding energies were calibrated using the C 1s peak at 284.8 eV.

Electrocatalysts play a critical role in the development of sustainable energy storage and transformation technologies. Platinum-based materials, in particular, are widely employed as anodic catalysts in direct methanol fuel cells due to their high intrinsic catalytic activity for methanol oxidation. In catalyst selection and design, the Sabatier principle serves as an important guideline: the interaction between the catalyst surface and reaction intermediates should be neither too strong nor too weak to enable both efficient activation and effective product desorption. To evaluate the catalytic performance of the synthesized PtAg nanotube catalysts, their electrocatalytic activity toward methanol oxidation was systematically compared with that of commercial 20% Pt/C under identical experimental conditions. Based on these comparisons, the optimal PtAg catalyst was identified and subsequently integrated into a membrane electrode assembly for further testing in a direct methanol fuel cell. This approach enables a direct assessment of the practical electrocatalytic performance and application potential of the PtAg catalysts.

4.3.3 ELECTROCHEMICAL PROPERTIES

The electrochemical active surface area (ECSA) is a critical factor for catalysts. ECSA is calculated based on the charge associated with hydrogen adsorption or desorption in the cyclic voltammetry (CV) curve. In our results, the ECSA was estimated by measuring

the charge associated with hydrogen underpotential deposition (H_{upd}) adsorption (Q_H) between -0.2 and 0.1 V, using the formula:

$$\text{ECSA} = \frac{Q_H}{q_H \times m}$$

where a value of 210 $\mu C/cm^2$ is assumed for the adsorption of a monolayer of hydrogen on a platinum surface (q_H) [194]. The H_{upd} adsorption charge (Q_H) can be determined using $Q_H = 0.5 \times Q$, where Q represents the charge in the H_{upd} adsorption/desorption region obtained after double-layer correction.

The ECSAs of the Pt/C, PtAg-1, PtAg-2, and PtAg-3 catalysts were found to be 175.7, 121.2, 260.7, and 20.75 cm^2/mg_{Pt}, respectively (Figures 4.3.8a and 4.3.8c). The peak potential of the 20% Pt/C catalyst was measured at 492.7 mV, while the peaks for PtAg-1, PtAg-2, and PtAg-3 were observed at 598.7 mV, 592.7 mV, and 580.7 mV, respectively. This indicates that the electrochemical stability of the PtAg catalysts is significantly enhanced compared to that of 20% Pt/C.

Furthermore, in CV tests conducted in acidic methanol solutions, the results demonstrated that PtAg-2 exhibited the best performance, likely due to its favorable surface morphology and higher platinum utilization. We also assessed the methanol oxidation process by comparing the cyclic voltammograms of the PtAg catalysts and the Pt/C catalyst in a mixed solution of 0.5 M H_2SO_4 and CH_3OH. During the forward scan, distinct oxidation peaks attributed to methanol oxidation were observed. These peaks result from the electrocatalytic oxidation of methanol occurring on the surface of the catalysts.

The oxidation peak currents for Pt/C, PtAg-1, PtAg-2, and PtAg-3 were measured at 164.1 mA/mg_{Pt}, 482.55 mA/mg_{Pt}, 667.70 mA/mg_{Pt}, and 352.41 mA/mg_{Pt}, respectively. During the forward scan, intermediate products generated from methanol oxidation contribute to new peaks in the reverse scan, which are oxidized during that phase. While peak current density and ECSA are commonly used to estimate catalyst activity, it is important to note that ECSA only provides a measure of the number of electrochemically active sites on the electrode, not all of which exhibit catalytic activity.

Therefore, we also computed and compared the mass activity and specific activity of the catalysts to provide a more comprehensive evaluation of their catalytic performance. Specific activity was also calculated to evaluate the catalytic activity of the catalysts. The results indicate that the overall activity of the PtAg catalysts is higher than that of the Pt/C catalyst. This enhanced performance suggests that the PtAg catalysts possess superior catalytic properties for methanol oxidation compared to their Pt/C counterpart.

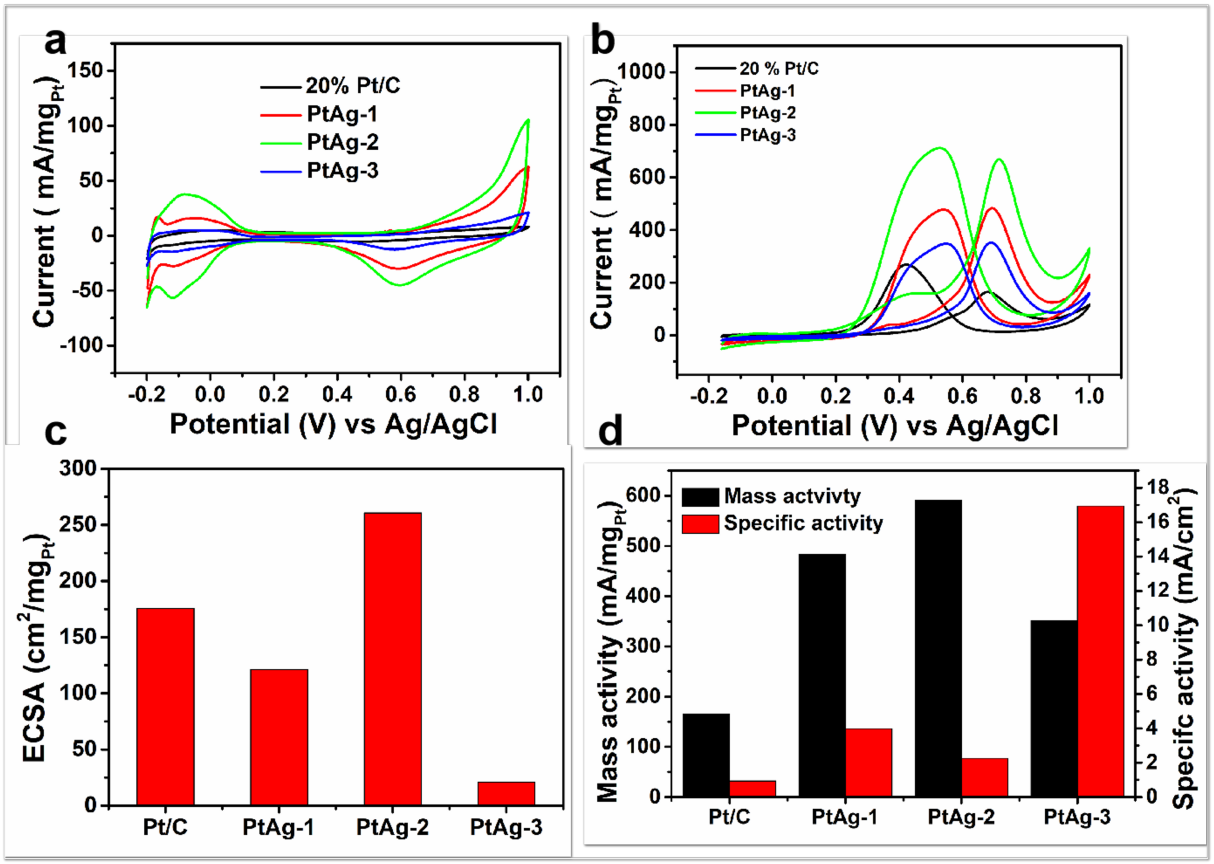

Figure 4.40: Electrocatalytic activity of PtAg-1, PtAg-2, PtAg-3, and Pt/C (20%) catalysts: (a) cyclic voltammetry curves in N_2-saturated 0.5 M H_2SO_4 solution at a scan rate of 50 mV/s; (b) mass activity in 0.5 M H_2SO_4 + 2 M CH_3OH solution at a scan rate of 50 mV/s; (c) histogram of ECSA of different catalysts for the methanol oxidation reaction (MOR) in 0.5 M H_2SO_4 solution; (d) histogram of mass and specific activities of different catalysts for MOR in 0.5 M H_2SO_4 + 2 M CH_3OH solution.

This improvement in activity may be attributed to the ability of silver to modulate the electronic structure of platinum, thereby adjusting the binding energies of the intermediate products during the methanol oxidation reaction (MOR). This adjustment results in enhanced MOR activity. Additionally, the unique porous structure of the nanowires and their high electrical conductivity further contribute to the improved catalytic performance.

Figures 4.41 and 4.42 illustrate the cyclic voltammograms of Pt/C and PtAg catalysts at various scan rates [195]. As the scan rate increases, both the intensity of the oxidation peaks and their peak potentials shift positively. Additionally, we compared the trends of current density as a function of the square root of the scan rate to assess the kinetics of methanol oxidation for each catalyst.

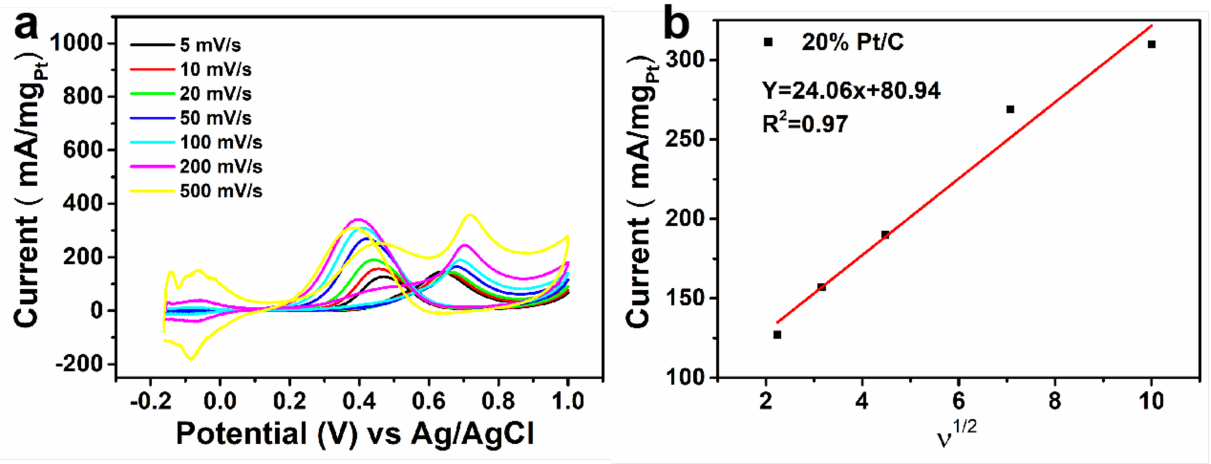

Figure 4.41: a. Cyclic voltammograms (CV) of methanol oxidation reaction (MOR) on PtAg-1 at different scan rates; b.corresponding plot of forward peak current versus the square root of the scan rate.

From Figures 4.41b and 4.42b, d, and f, it is evident that the oxidation peaks increase linearly with the rising scan rates. The corresponding slopes for Pt/C, PtAg-1, PtAg-2, and PtAg-3 were found to be 24.06, 40.07, 50.42, and 36.23, respectively. This indicates that the methanol oxidation reaction follows a diffusion-controlled process.

The higher slope value of the PtAg catalysts compared to the commercial Pt/C catalyst suggests an enhancement in the kinetics of methanol electro-oxidation on the PtAg catalysts. This improvement can be attributed to the more favorable reaction conditions and structural characteristics of the PtAg catalysts, which facilitate more efficient mass transport and reaction kinetics.

The electrochemical durability of the catalysts was evaluated through long-term stability tests in acidic methanol solution(Figures 4.43). The current density of the Pt/C catalyst gradually decreased with increasing cycles of cyclic voltammetry (CV). For PtAg-1, the current density also decreased after a certain number of cycles. In contrast, PtAg-2 and PtAg-3 exhibited a continual increase in current density, although the rising trend for PtAg-3 was less pronounced than that for PtAg-2.

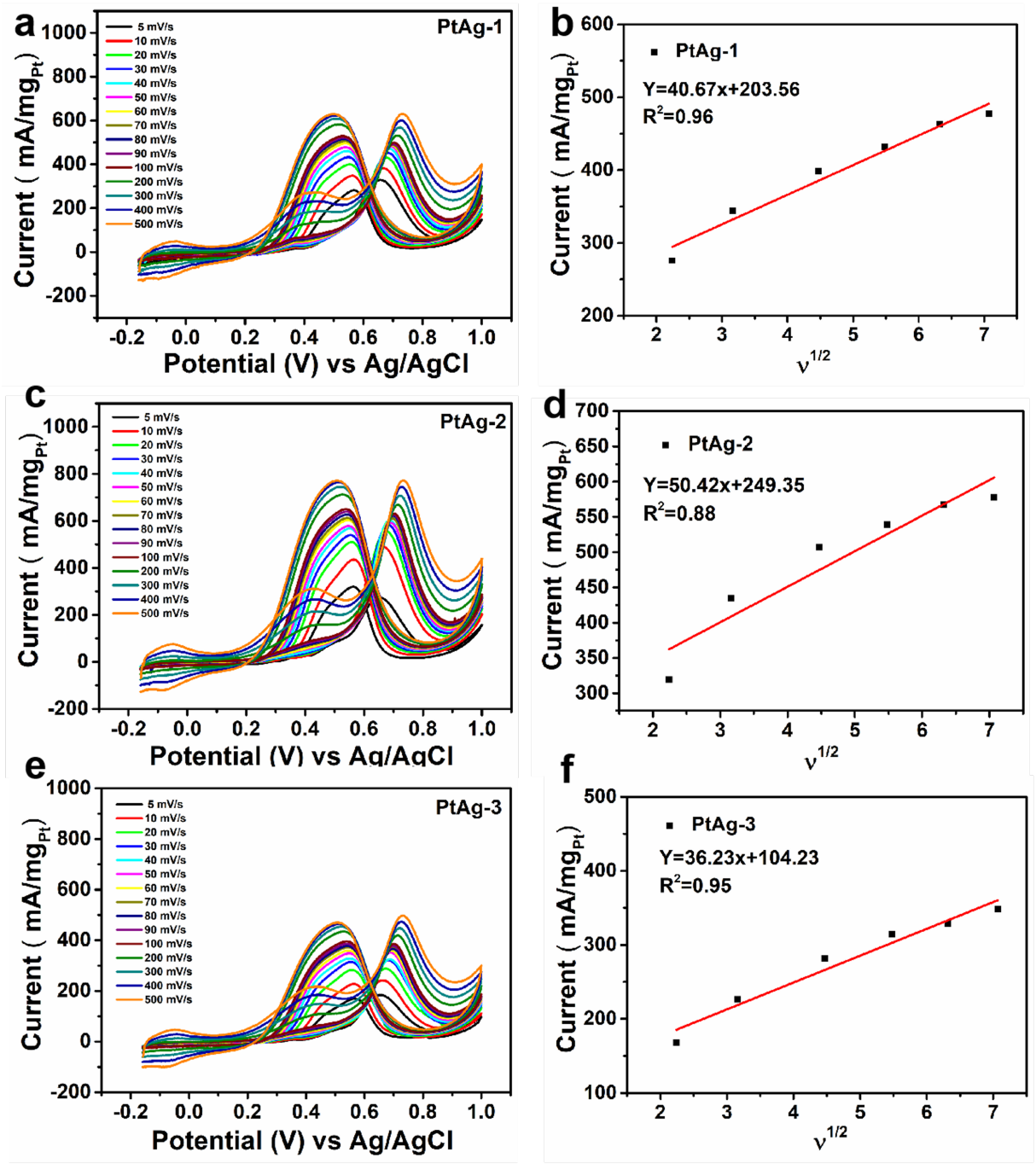

Figure 4.42: a. CV of MOR on PtAg-1 at different scan rates and b. the corresponding plot of forward peak current versus the square root of the scan rate. c. CV of MOR on PtAg-2 at different scan rates and d. the corresponding plot of forward peak current versus the square root of the scan rate. e. CV of MOR on PtAg-3 at different scan rates and f. the corresponding plot of forward peak current versus the square root of the scan rate.

As shown in Figure 4.44, chronoamperometry tests were conducted on the catalysts after cycling [196]. Over a 3600-second experimental period, PtAg-3 demonstrated the lowest residual current density, followed by Pt/C, while PtAg-2 exhibited the highest residual current density. These results indicate that PtAg-2 possesses the best durability.

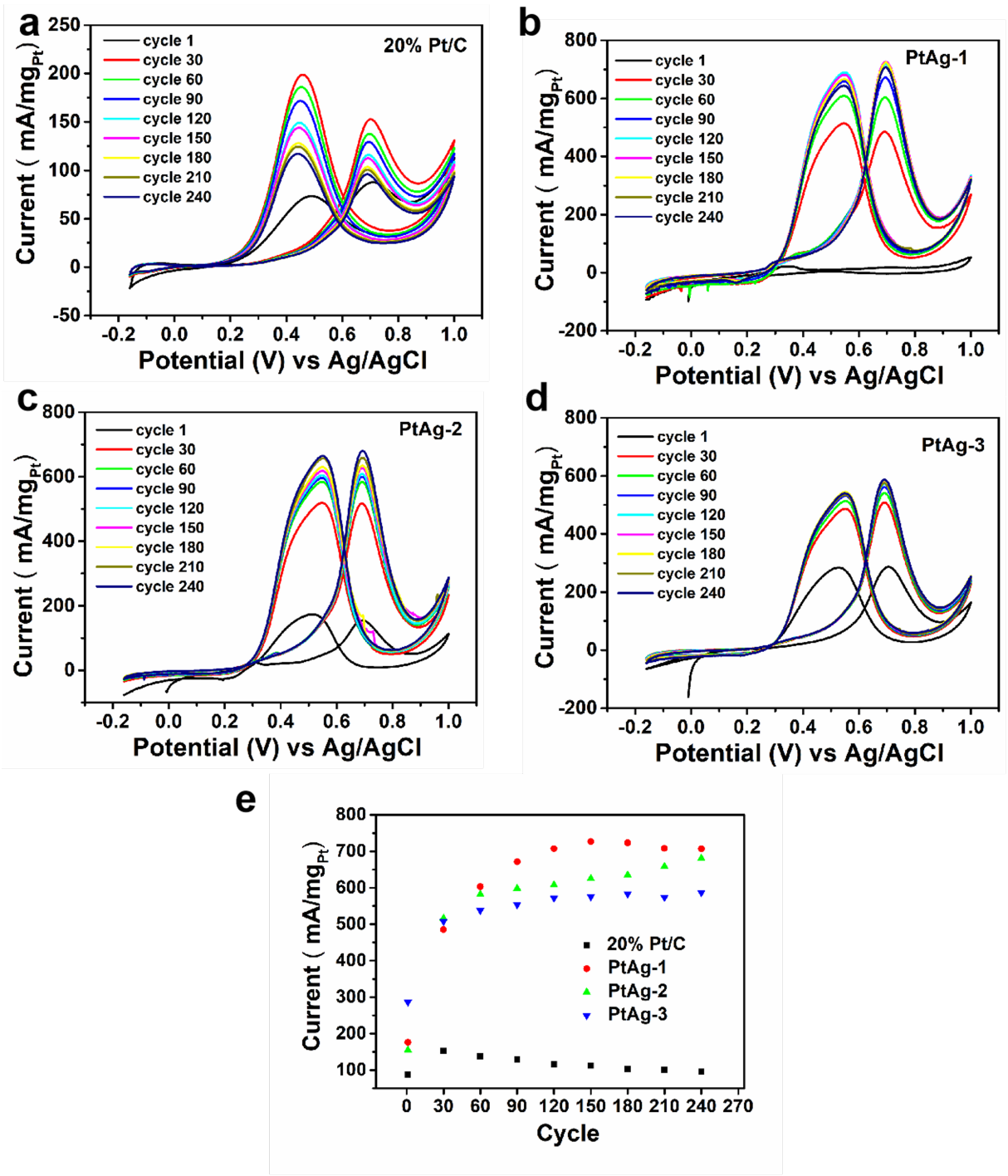

Figure 4.43: Cyclic voltammograms (CV) of the commercial Pt/C, PtAg-1, PtAg-2, and PtAg-3 catalysts for the methanol oxidation reaction (MOR) in 0.5 M H_2SO_4 + 2 M CH_3 OH.

For the Pt/C catalyst, significant aggregation of the commercial Pt nanoparticles was observed after the durability test, with uniformly sized small Pt nanoparticles coalescing into larger, irregular particles, resulting in reduced durability. In the case of PtAg-3, the low residual current density may be attributed to its crystal structure, which resulted in fewer active sites compared to PtAg-1 and PtAg-2, as indicated by TEM analysis. Relative

to PtAg-2, PtAg-3 had larger deposited nanoparticle sizes. For isolated Pt particles, the optimal catalytic activity is typically found at sizes ranging from 1 to 3 nm, which explains the lower catalytic activity of PtAg-3 compared to PtAg-2.

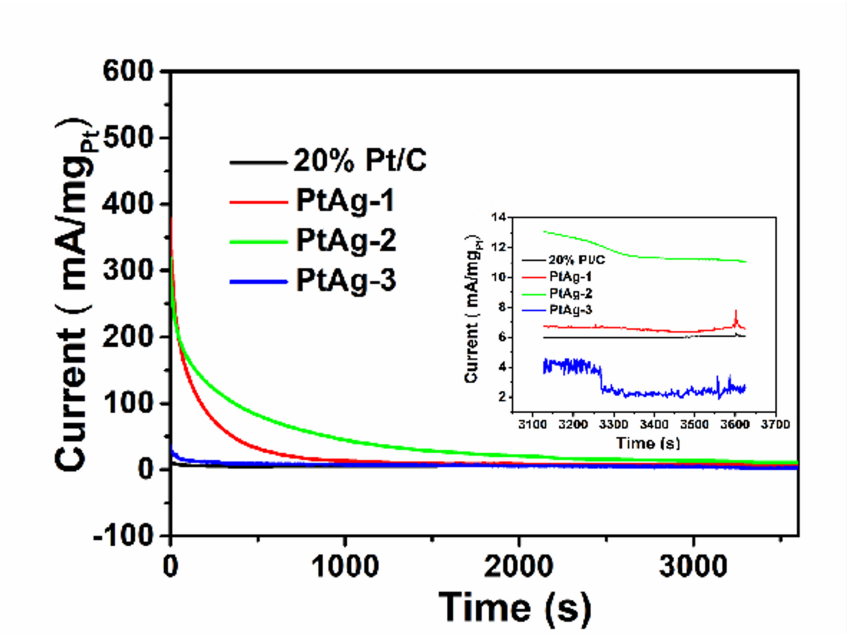

Figure 4.44: Current–time curves recorded at 0.70 V; the inset shows a magnified image of the region indicated by the square.

For platinum-based catalysts in the MOR, the reaction proceeds through a pathway that generates CO intermediates. CO is a toxic species that can occupy active sites on the metal surface, thereby reducing the catalytic activity. To further investigate the poisoning capability of the catalysts, we conducted CO poisoning tests in acidic methanol solution to ensure that the catalyst surface was fully covered by a monolayer of CO. Based on the data from the second CV cycle, we can ascertain that CO had completely desorbed from the catalyst surface[54]. The corresponding potentials observed for the catalysts were 0.670, 0.724, 0.748, and 0.720 mV. These results indicate that the PtAg catalysts reacted with CO at elevated potentials in the acidic methanol solution, demonstrating their ability to tolerate CO poisoning under these conditions. The presence of methanol in the electrolyte indicates that, compared to pure Pt/C, the CO oxidation potential of PtAg is higher, which may be attributed to the stronger catalytic activity of PtAg towards methanol oxidation. The enhanced reactivity likely results in methanol participating in the oxidation process alongside the oxidation of CO adsorbed on the catalyst surface, thereby increasing the oxidation potential.

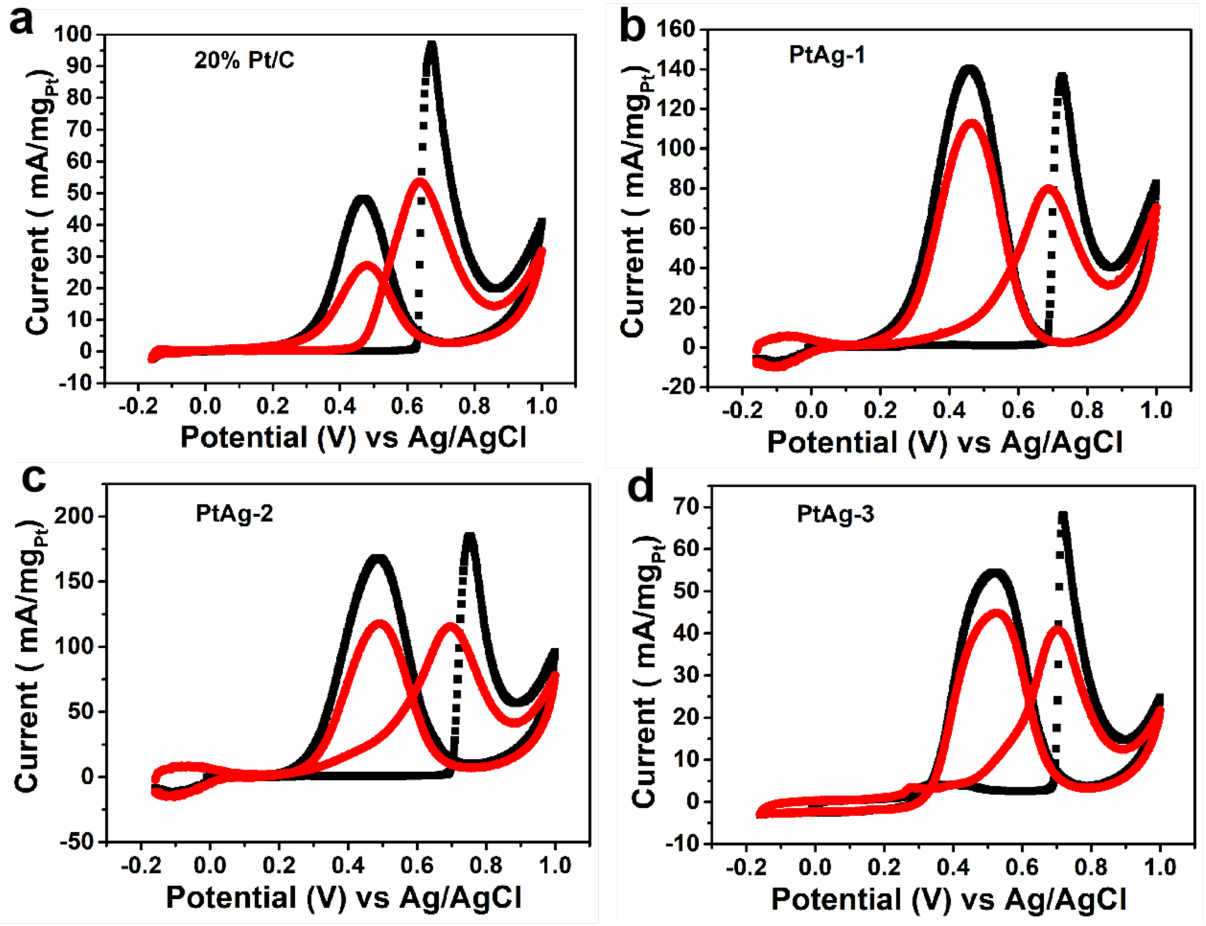

Figure 4.45: CO-stripping voltammograms in 0.5 M H_2SO_4 solution at a scan rate of 50 mV s^{-1} for Pt/C, PtAg-1, PtAg-2, and PtAg-3 catalysts.

The catalytic performance was evaluated in a customized direct methanol fuel cell (DMFC) system [197–201]. After assembly of the membrane electrode structure, the cell was subjected to standard pre-conditioning and activation procedures. Subsequently, polarization curves were obtained by varying the applied load current and recording the corresponding cell voltages. Commercial 60% Pt/C was used as the reference catalyst, whereas the Pt content in the PtAg-2 catalyst is only 6.68%. To ensure an equivalent mass of Pt loaded onto the carbon paper, a larger total mass of PtAg-2 was required. This increased catalyst dosage is likely to cause partial catalyst agglomeration and reduce the effective contact area between the catalyst and reactants, thereby decreasing the number of accessible active sites and limiting charge/mass transfer during methanol oxidation. As a result, the catalytic performance of PtAg-2 was inferior to that of the 60% Pt/C catalyst, and the maximum power output of the 60% Pt/C-based fuel cell was approximately 3.6 times that of the PtAg-2 system.

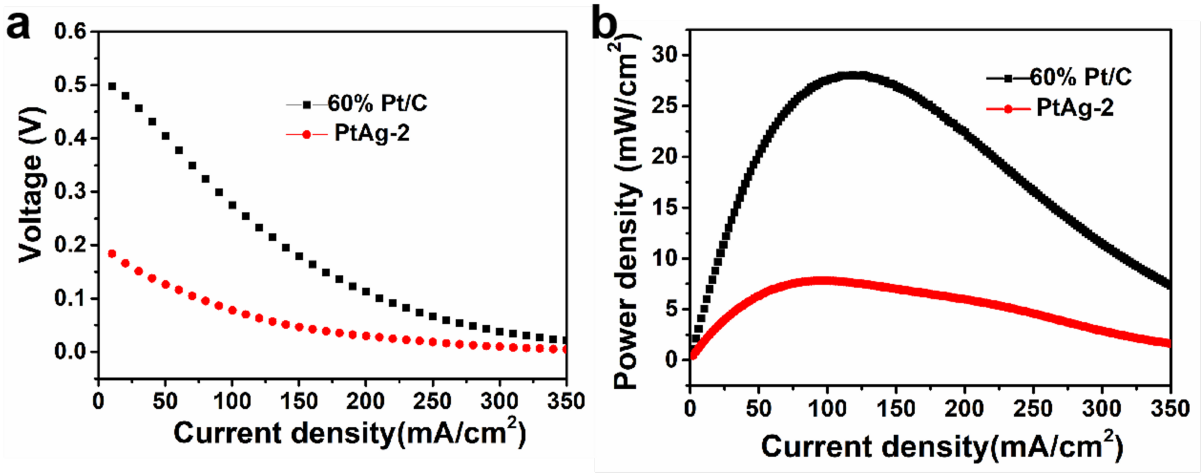

Figure 4.46: Voltage (a) and power density (b) as a function of current density for a DMFC at 65 °C.

4.3.4 CONCLUSION

Overall, PtAg nanotubes were synthesized via a galvanic displacement reaction using AgNWs as templates. The residual PVP content on the Ag nanowire surface is identified as the key quantitative parameter governing the structural evolution and compositional regulation of the PtAg alloy. Thermogravimetric analysis confirms that the AgNWs used in PtAg-1, PtAg-2, and PtAg-3 contain 5.90 wt%, 1.84 wt%, and 1.13 wt% residual PVP, respectively. Despite these seemingly minor differences, such variation in PVP content leads to pronounced differences in Pt deposition behavior, alloy formation, wall thickness, and surface morphology of the resulting nanotubes.

During the galvanic displacement process, PVP modulates the coordination environment and surface adsorption behavior, thereby directly influencing the nucleation and growth kinetics of Pt atoms. Specifically, when the residual PVP content is controlled at approximately 1.84 wt%, the resulting PtAg nanotubes (PtAg-2) exhibit the most uniform Pt/Ag elemental distribution, optimal wall thickness, and the highest electrochemically active surface area (ECSA). Consequently, the mass activity of PtAg-2 reaches 4.07 times that of commercial 20% Pt/C, and it also demonstrates superior long-term electrochemical stability. However, when incorporated into membrane electrode assemblies, the practical performance of PtAg-2 is limited by its relatively low Pt content (6.68%) compared to commercial 60% Pt/C. To achieve comparable Pt loading, a higher catalyst dosage is required, which can induce nantube aggregation and lead to accelerated activity degradation during operation. Furthermore, ICP-OES analysis reveals a low Pt utilization efficiency during synthesis, indicating that a significant portion of Pt remains unincorporated in the final product, suggesting that further optimization of the deposition and alloying process is necessary.

In summary, precisely controlling the residual PVP content near approximately 1.84 wt% is essential for tailoring the surface structure, electronic configuration, and catalytic performance of PtAg nanotubes. These findings highlight the critical role of ligand-amount regulation in directing alloy formation and provide a mechanistic basis for tuning PtAg alloy catalysts for enhanced methanol oxidation performance.

Chapter 5

OUTLOOK

In the first part of this research, I explored how polyethylenimine (PEI) affects the distribution of silver nanowires (AgNWs) within porous silica sponges and subsequently influences their conductivity and mechanical properties. The silica sponge used in this work had a relatively low density, which suggests that increasing the sponge density could enhance the mechanical properties and support the mass of the absorbed AgNWs, ultimately maintaining mechanical properties or even improving electrical conductivity. Future work could also optimize the freeze-drying step during sponge preparation to create larger internal pores and consider the use of longer AgNWs or copper wires as conductive fillers. These modifications are anticipated to yield lightweight, high-conductivity materials. In the second part of the study, we synthesized a composite porous sponge by coating AgNWs and silica fibers with polysiloxane. The multifunctional applications of the composite sponge were validated, yet several challenges require further investigation. For instance, the polymer unzipping reaction at high temperatures could potentially be mitigated through annealing procedures. Moreover, the non-conductive of the composite material may be addressed by rinsing off the polymer that covers the AgNWs and silica fibers, allowing direct contact between AgNWs to facilitate conductivity. Alternatively, polysiloxane and silica fibers could be mixed, with subsequent removal of the solvent before adding AgNWs and then freeze-drying to form the composite sponge. Based on the findings from these two parts, we propose designing Janus structures, where one part of the sponge is conductive and the other non-conductive, to cater to specialized applications. Additionally, coaxial electrospinning could be used to create hollow silica fibers, further reducing the composite material's electrical conductivity. These factors could be considered for further optimization to obtain high-performance composite materials. In the third part, we used polyvinylpyrrolidone (PVP)-coated AgNWs as templates for synthesizing PtAg alloys, aiming to investigate the role of PVP in the synthesis of nanometal materials. The use of PVP enabled precise control at the nanoscale. However, further

exploration of Pt's irregular crystal facets is necessary, potentially through scanning tunneling microscopy (STM), while PVP's electronic interactions with PtAg could be studied using Photoelectron Diffraction (PDVC) techniques. For practical applications, catalyst dispersion on the layer surface could be enhanced by utilizing a quantitative solid-liquid particle dispersion system to avoid linear agglomeration and improve the overall fuel cell performance. Optimizing the fuel and oxygen supply, possibly by using pure oxygen instead of compressed air, may help mitigate volume errors associated with oxygen supply. Increasing Pt utilization is another area of interest, which might be achieved through altering complexing agents.The interaction forces can be directly tested by modifying Pt and Ag ions through the AFM tip. By measuring the interaction forces between the metal ions and the ITO glass coated with PVP, which are likely to be Van der Waals interactions, a comparison can be made with tips that have not been modified with metal ions. These suggestions aim to guide future research to refine the synthesis, properties, and applications of porous composite materials and further enhance their performance in specialized environments.

Chapter 6

MATERIALS AND EXPERIMENTAL METHODS

6.1 MATERIALS

Tetraethyl orthosilicate (TEOS, 99.0%, Fluka), phosphoric acid (H_3PO_4, 85%, Merck), polyvinyl pyrrolidone (PVP, $M_n \approx$ 1,300,000 g/mol, Sigma-Aldrich), ethylene glycol (EG, 99.5%, Acros Organics), ferric chloride ($FeCl_3$, 99.9%, Sigma-Aldrich), silver nitrate ($AgNO_3$, >99%, VWR), Congo Red (Sigma), branched polyethyleneimine (PEI, $M_n \approx$ 10,000 g/mol, 50 wt% solution, Sigma-Aldrich), acetone (technical grade), ethanol (technical grade), hydrogen hexachloroplatinate(IV) hexahydrate (H_2PtCl_6, Tokyo Chemical Industry), sulfuric acid (H_2SO_4, >98%, Merck), Nafion 117 (5%, Sigma-Aldrich), methanol (>99.9%, Fisher Chemical), and ammonia (25%, VWR) were used in this thesis.

All water used throughout the experiments was of Milli-Q grade. Milli-Q water was obtained from a Milli-Q Plus purification system equipped with a QPAK® 2 column and had an electrical conductivity of 18.2 MΩcm. All glassware and magnetic stirring bars used in the syntheses were thoroughly cleaned in aqua regia (HCl/HNO_3 = 3:1), rinsed with distilled water, and dried before use.

6.2 MATERIAL CHARACTERIZATION

6.2.1 MORPHOLOGICAL AND STRUCTURAL CHARACTERIZATION

Microscopes are common tools used to observe the surface morphology of materials. Microscopes can be optical microscopes, scanning electron microscopes, transmission electron microscopes, atomic force microscopes, and scanning probe microscopes. Among these, electron microscopy opens the world of nanomaterials and is a key technique for the characterization of materials. In addition to microscopes, secondary ion mass spectrometry and X-ray techniques can also characterize the morphology of a material. For this thesis, we used optical microscopes, scanning electron microscopes, and transmission electron microscopes to examine the morphology of the materials.

Optical Microscope

The viewing limit of an optical microscope is 100 nm, largely due to the wavelength range of visible light radiation, which is between 400 nm and 700 nm. The optical microscopes used in the thesis were the VHX digital microscope (VH-Z500) and the ZEISS smartzoom 5 motorized digital microscope. VH-Z50 microscope was used to observe the electrospinning fibers, while a smartzoom 5 motorized microscope was used to observe the macroscopic structure of the sponge.

Scanning Electron Microscopy (SEM), Transmission Electron Microscopy (TEM), and Scanning Transmission Electron Microscopy (STEM)

For scanning electron microscopy (SEM), transmission electron microscopy (TEM), and scanning transmission electron microscopy (STEM), the use of a high-energy electron beam on the surface of a solid sample produces a variety of signals originating from the interaction between the electrons and the sample, revealing detailed information about the specimen. When a beam of high-energy incident electrons bombards the surface of a sample, the activated region emits secondary electrons, backscattered electrons, Auger electrons, transmitted primary electrons, characteristic X-rays, and electromagnetic radiation in the visible, ultraviolet, and infrared regions, as well as electron–hole pairs, lattice vibrations (phonons), and electron oscillations (plasmons), as partially depicted in Figure 6.1a-b.

Compared with optical microscopes, SEM provides clearer images because electrons exhibit wave–particle duality, and their wavelength depends on momentum, which is influenced by changes in the accelerating voltage. Higher voltage results in higher energy, shorter wavelength, and thus a clearer image. For SEM, the magnification can range from 100 to 500,000 times, whereas for TEM, the magnification can range from 2,000 to

1,000,000 times. SEM is primarily used to observe the surface morphology of materials through electron reflection, while TEM enables the transmission of electrons through the sample, providing information about its internal structure.

In this thesis, backscattered electron detection (BSD) and energy-dispersive X-ray spectroscopy (EDS) were employed to analyze the elemental composition of the samples in addition to conventional morphological characterization.

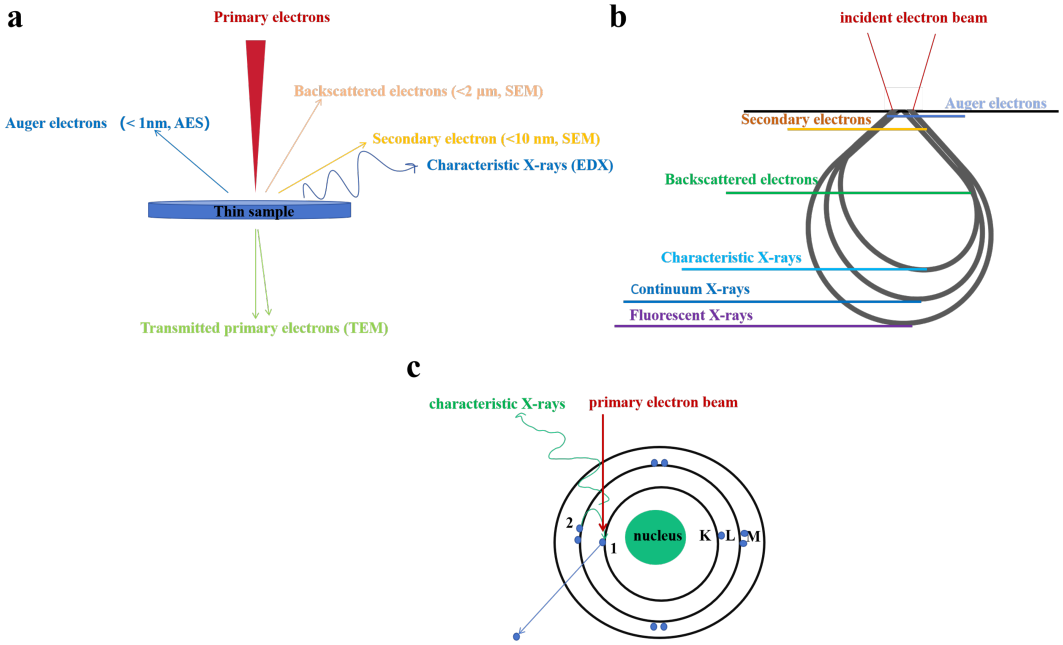

Figure 6.1: The interaction of incident electrons with specimen, a. on the surface of a thin sample, b. on a thick sample, c. EDX working principle.

Backscattered electron imaging is the result of an elastic collision of an incident electron with an atom, which results in a change in the orbit of the incident electron. When incident electrons collide with atoms, heavier atoms scatter electrons more readily than lighter atoms, resulting in a stronger signal, so the number of backscattered electrons reaching the detector is proportional to the atomic number of the substance. In our thesis, Ag atoms (higher atomic number) scatter more incident electrons to the detector than lighter Si or O atoms and therefore look brighter in the SEM image. EDX is used for element definition, content, and position, which are in a sample. In EDX, an incident high-energy electron beam hits a sample and transfers some of its energy to the sample's atoms. The electrons of the atoms in the sample absorb this energy and break away from the atoms, jumping to energy levels higher than Fermi energy. At this point, the empty space left in the electron orbital is filled with electrons in higher-energy orbitals, a process that produces X-rays and releases excess energy, as shown in Figure 6.1c. For any given atom, the energy difference between the various energy levels is determined, and the energies of the X-rays produced by the various atoms as a result of excitation are determined, which can therefore be used to identify the type of element present in a

sample. In this thesis, SEM analysis was done on a Zeiss LEO 1530 instrument (Jena, Germany) equipped with a Schottky field-emission cathode at an acceleration voltage of 3 kV. Before measurements, the samples were sputter-coated with a 3 nm platinum layer by a high-resolution sputter coater (208 HR, Cressington). Backscattered electron (BSE) measurements were performed at an acceleration of 10 kV with the Robinson detector, and the working distance was 10 mm. Transmission electron microscopy involves projecting an accelerated and focused beam of electrons onto a very thin sample, where the electrons collide with atoms in the sample and change direction, resulting in stereo-angular scattering. The magnitude of the resolution is affected by the De Broglie wavelength of the electrons. The concentrated nanomaterial dispersion in water was drop-cast onto a carbon-covered copper grid, which is carbon support films, 300 mesh, Quantofoil, treated with argon plasma beforehand, to prepare the sample. During the TEM measurement, we have used the test under the condition of a 200 KV voltage. The STEM can combine the techniques of SEM and TEM to see the internal structure of a sample at high resolution. The STEM we used was a JEM-F200 cold field emission electron microscope with a voltage of 200 kV and a silicon drift detector dual energy spectrum probe.

6.2.2 MOLECULAR/STRUCTURAL SPECTROSCOPIC ANALYSIS

The presence of elements and substances with characteristic spectral lines makes it possible to identify substances and determine their chemical composition, structure, or relative content by means of spectroscopic analysis of substances. Spectroscopic techniques are categorized according to the form of the detected location and are mainly divided into atomic and molecular spectroscopy. Molecular spectroscopy is categorized into four groups, namely infrared, ultraviolet, Raman, and fluorescence spectroscopy. In this thesis, infrared, Raman, and ultraviolet spectroscopic techniques are used.

Fourier-transform infrared spectroscopy (FT-IR)

FT-IR spectroscopy is a chemical analysis technique for the interaction between infrared light and matter, with wavelengths ranging from 780 nm to 1 mm. In our experiments, we used infrared absorption spectroscopy. Two conditions exist for the production of IR absorption spectra: the energy of the IR-radiated photons is the same as the energy required for the molecular vibrational energy level jumps and the coupling between the IR light and the molecules (the energy transfer is realized by the change of the molecular vibrational dipole moments). Nowadays, the mid-infrared region is generally used. In this thesis, we use a Perkin Elmer Ultra 2. The mode used is the total reflection mode, which utilizes the ATR (Total Reflectance Attenuation) effect. During the measurement, the sample is placed on the surface of an infrared ATR element, and as the infrared beam

passes through the ATR element, some of the light is reflected and some is absorbed. The absorbed light gives information about the infrared spectrum of the sample, which can be analyzed for chemical composition (Figure 8.2.2 b).

Raman spectroscopy

Raman spectrometers use a monochromatic laser (usually in the visible or near-infrared wavelengths) to probe materials. When a sample is irradiated, most of the light is scattered without changing energy, a process known as Rayleigh scattering. However, a small fraction of photons lose or gain energy as they scatter due to molecular vibrations, a phenomenon known as the Raman effect. The energy of these vibrations is related to the composition and structure of the molecule. While infrared spectroscopy involves changes in dipole moments during vibrations, Raman spectroscopy requires a change in the polarizability of the analyte, i.e., a change in the shape of the electron cloud. Well-defined energy transitions cause changes in polarizability, resulting in Raman scattering. Raman spectroscopy is used to track the intensity versus wavelength shift to obtain a combination of shifts specific to the chemical structure of the sample. The instrument used in this experiment is a Witec Alpha 300 RA+, and the wavelength used is 532 nm (Figure 8.2.2 c).

Ultraviolet-visible spectroscopy

The UV-Vis spectrophotometer is a detector designed based on the principle of absorption of UV light by solute molecules, operating according to the Lambert-Beer law. This law states that when a beam of monochromatic light passes through a flow cell if the mobile phase does not absorb the light, the absorbance A is directly proportional to the concentration of the light-absorbing component C and to the length of the optical path of the cell L. The absorbance is then measured by taking the negative logarithm of the transmittance of the substance. In our experiments, UV-Vis spectra were recorded using a JASCO double-beam UV-visible spectrophotometer with quartz glass cuvettes and a halogen lamp. We calculated the length of the nanowire by analyzing the position of the peaks, which is caused by the plasmon resonance (Figure 8.2.2 d).

X-ray diffraction

X-rays are extremely short wavelength (10^{-8} to 10^{-12} m), a high-energy electromagnetic wave. We generally use soft X-rays between 0.25 and 0.05 nm to analyze the crystal structure of the material phase rather than the elements of the chemical composition. In the case of crystal structures, such as metal nanowires, the atoms in the crystals are forced to move periodically under the action of X-rays, and a large number of atomically dispersed waves interfere with each other in space to form X-ray diffraction patterns. The intrinsic relationship between diffraction and crystal structure is revealed by the Bragg equation for structural analysis, and the grain size is measured using the Scherrer formula,

which relates grain size to the half-peak width of the diffraction peaks. For amorphous structures, since there is no long-range ordering of the atomic arrangement, only short-range ordering in the range of a few atoms exists, resulting in some diffuse reflection of the broad peaks. The XRD instruments of the first and second work used in our study are Bruker-AXS 2D SAXS with copper target. The third work of powder XRD data was collected using a STOE Stadi-P diffractometer with a Mo anode (λ = 0.70926 Å) and a DECTRIS MYTHEN 1K strip detector in Debye-Scherrer geometry. Work 1 and 2 employ a copper target as the light source, tested at angles ranging from 30 to 85 degrees, 0.15 degrees per minute. The wavelength, test step, and test range of work 3 are specified as follows: 0,7 mm quartz capillary is used; measurement ranges up to 46°; step size is 0.015°; measuring time is 150 s. The structure of the nanomaterials for Work 3 was refined using FullProf software via the Rietveld method (Figure 8.2.2 e).

X-ray photoelectron spectroscopy

X-ray Photoelectron Spectroscopy (XPS) is a method that uses an electron spectroscopy tester to measure the energy distribution of photoelectrons and auger electrons emitted from the surface of a sample when irradiated with X-ray photons and analyzes them using photoionization. Since only a thin layer of photoelectrons emitted near the surface of the sample can escape, the depth of the sample that can be detected is generally three times the depth of electron escape. For metals, this depth is generally 0.5-3 nm, for inorganic non-metallic materials it is 2-4 nm, and for organics and polymers, it is 4-10 nm. XPS analyzes samples qualitatively by photoionization. The reason XPS can analyze the valence states is that the binding energy of the electrons in the inner shells of atoms changes due to the different types and numbers of elements bonded to them, or due to different valence states of the atoms. This change is reflected in the spectral peaks. The displacement of these peaks indicates the electronic binding energy variations caused by different bonded elements or valence states. For XPS measurements, a PHI 5000 VersaProbe III machine was employed. The X-ray source is an Al K excitation source (hv = 1486.6 eV) with a beam diameter of 100.0 µm*100.0 µm and a pass energy of 26 eV. The high-resolution spectra were analyzed using PHI Multipak software. The shift for every peak that was recorded was the same (Figure 8.2.2 f).

6.2.3 QUANTITATIVE COMPOSITION ANALYSIS

There are four commonly used methods to analyze the elemental composition of substances: X-ray fluorescence spectrometry (XRF), inductively coupled plasma spectrometry (ICP), energy dispersive X-ray spectrometry (EDS), and wavelength dispersive spectrometry (WDS). In our experiment, we used an inductively coupled plasma emission spectrometer and an energy-dispersive X-ray spectrometer for quantitative analysis of the

composition. Additionally, the polymer content on the surface of the metal nanowires was calculated using thermogravimetric analysis (TGA).

Inductively coupled plasma-optical emission spectrometry

Inductively Coupled Plasma-Optical Emission Spectrometry (ICP-OES) is based on the emission of well-characterized spectral lines from a substance in a high-temperature plasma formed by a high-frequency magnetic field. These spectral energies are detected by a semiconductor detector, and the content of the element to be measured in the test solution is calculated from standard solution curves. The effective wavelength range for the test is 120-800 nm. The ICP-OES principle involves transferring electrons from the ground state to an excited state by utilizing the fact that atoms and ions can absorb energy. This energy comes from the heat generated by an argon plasma operating at 10,000 Kelvin in ICP-OES. The working principle of ICP-OES is based on the ability of the excited atoms to release light at particular wavelengths when transitioning to a lower energy level. The instrument used in this thesis is a Perkin Elmer Avio 200 equipped with an S10 autosampler, an Echelle polychromator, an argon humidifier, and a DBI-CCD detector. All samples were filtered with syringe filters (PTFE, 0.22 µm). The standard curves were plotted using concentrations of 0.01 mg/L, 0.05 mg/L, 0.1 mg/L, 1 mg/L, 10 mg/L, and 30 mg/L of silver dissolved in a 5% nitric acid solution. For the first and second works, the samples were treated by dissolving a certain amount of the sample in concentrated nitric acid, then diluting it to 5 %, filtering to remove the silica fibers, and then testing it. For the third work, the samples were treated by dissolving them in aqua regia, filtering to remove the silver oxide, and then testing to obtain the platinum content. The ICP-OES uses the Lambert-Beer law to measure the energy of emitted light at each wavelength and calculate the concentration of metal in the sample (Figure 8.2.2 g).

Energy dispersive x-ray spectrometer

The Energy Dispersive X-ray Spectrometer (EDS) is an instrument for analyzing the elements of a substance. In the thesis, the EDS is used in conjunction with a scanning electron microscope (SEM) and a transmission electron microscope (TEM). It bombards the surface of a sample with a beam of electrons in a vacuum chamber, which excites the substance to emit characteristic X-rays. The EDS then qualitatively and semi-quantitatively analyzes elements of the periodic table with atomic numbers greater than 5, based on the characteristic wavelengths of the X-rays, with a detection limit of 0.1 percent. In our experiments,The EDS used in the TEM is SDD dual energy spectrum probe. Compared with XPS, both EDS and XPS can be used for qualitative and quantitative analysis of elements. However, XPS uses X-rays to hit the electrons and detects electrons, while EDS uses electrons to hit the sample and detects the emitted X-rays. EDS can only detect the composition and content of elements but cannot determine their valence, and the element

content needs to be more than 2% for detection. In contrast, XPS can detect surface elements and their content, as well as determine the valence states of the elements. XPS has higher sensitivity, with a minimum detection concentration of greater than 0.1%. The detection range of XRD is typically for element concentrations greater than 1%.

Thermogravimetric analysis

Thermogravimetric Analysis (TGA) is a thermal analysis technique that measures the relationship between the mass of a sample and the change in temperature under programmed temperature control. It can be used to study the thermal stability and composition of materials. The basic working principle is that the balance displacement caused by the change in sample weight on the thermal balance is converted into an electromagnetic signal. The magnitude of this signal is proportional to the change in sample weight, and this small signal is amplified by an amplifier to record the change in sample mass. Here, we determined the content of PVP on the surface of AgNWs using TGA. We also investigated the thermal stability of silver and silica composites. Thermogravimetric analysis was performed on a TGA 209 Libra F1 (Netzsch, Selb, Germany) in an aluminum oxide (The pro 85 μL , 6.8 $\times$ 4 mm). The heating rate was set to 10 K/min under the nitrogen or air condition from 20 to 800 ℃.

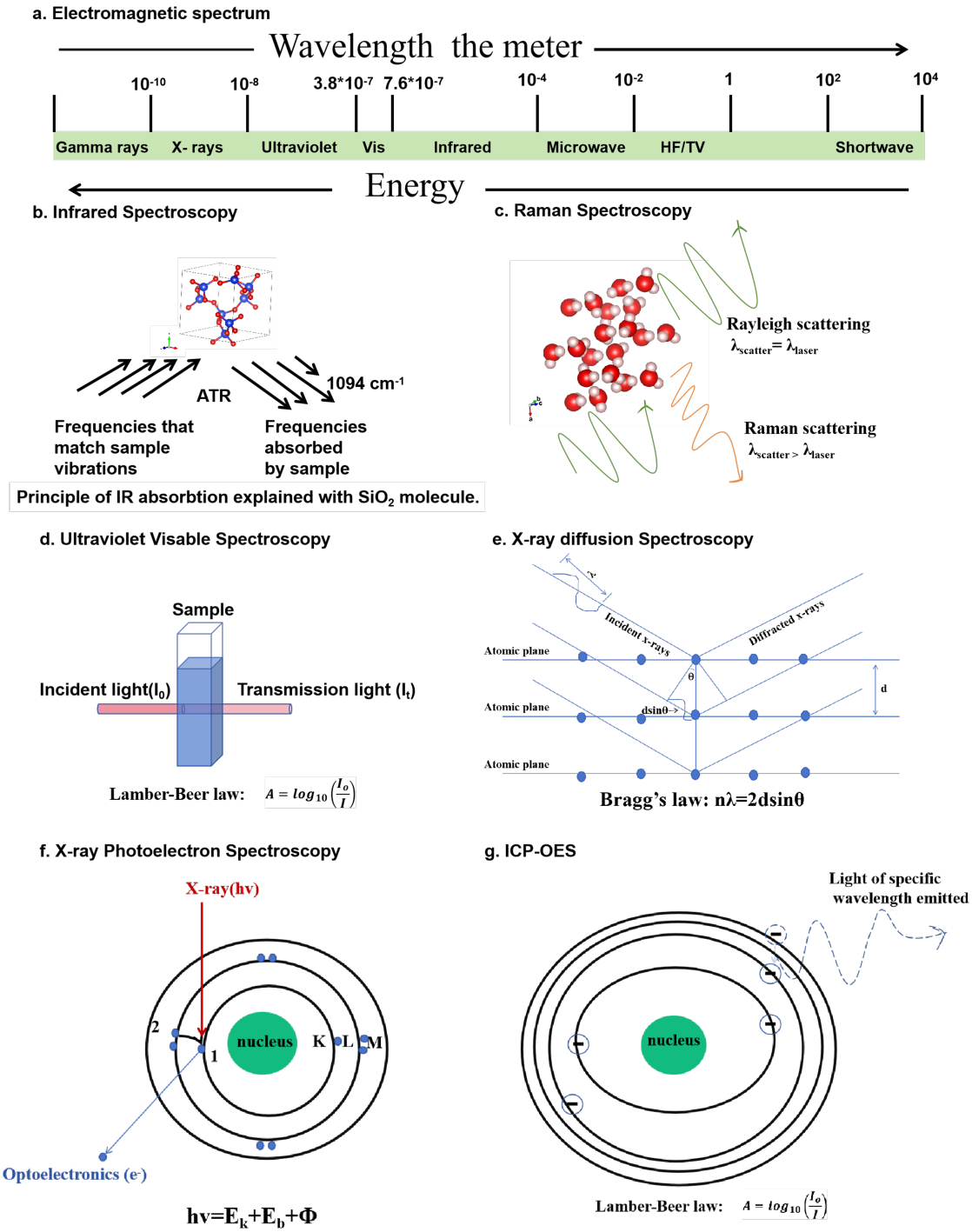

Figure 6.2: Simple instrument principle schematic a. Infrared spectroscopy. b. R aman spectroscopy. c. Ultraviolet visable spectroscopy. d. X-ray diffusion spectroscopy. f. X-ray photoelectron spectroscopy. g. Inductively coupled plasma-optical emission spectrometry (ICP-OES).

6.2.4 MECHANICAL PROPERTIES

Tensile and compressive tests were conducted on the materials presented in this thesis. The specimen was clamped between fixtures or between two flat molds, allowing the two

collets/plates to move relative to each other. During the test, the force and displacement changes were captured by the force transducer located on the moving collet and the displacement transducer built into the machine. These measurements were used to calculate the specimen's performance indexes. The compression test and the cyclic compression test were performed on a Zwick Z2.5 machine equipped with a 200 N sensor at a compression rate of 10 mm/min. Hundred compression cycles were measured, and the curves for 1-100 cycles were recorded. The tensile test used a 20N sensor.

6.2.5 CONTACT ANGLE MEASUREMENT

The contact angle is the angle formed between the liquid and the solid-liquid interface when the liquid is placed ideally to describe or measure its wetting behavior on a solid surface. The magnitude of the contact angle is determined by Young's equation, which incorporates surface tensions at the three interfaces involved. Factors influencing the contact angle include the inherent properties of the material, contact angle hysteresis, surface roughness, unevenness of the solid surface, and environmental conditions. For instance, in hydrophilic materials, increased surface roughness typically results in a smaller contact angle, indicating better wettability. Conversely, hydrophobic materials exhibit a larger contact angle with greater surface roughness, indicating poorer wettability. Wetting phenomena are generally categorized into three types: ashesion, immersions, and spreading. A contact angle of approximately 90 degrees is commonly used as a criterion for assessing the hydrophilicity of materials, particularly in the ashesion process. ashesion energy is often calculated through the immersion process to assess the potential for spontaneous wetting. In systems with hydrophilic materials, the spreading coefficient can be computed from spreading behavior to determine whether the liquid can autonomously spread on the solid surface.

In our experiment, we employed a simple ashesion test method to evaluate changes in material hydrophilicity by machine A. The droplet was dispensed at a velocity of 0.16 μL/s with a volume of 5 μL.

6.2.6 CONDUCTIVITY TEST CHARACTERIZATION

The carriers of electronic conductivity are electrons or holes (i.e., electron vacancies). We use the DC method for materials that are purely electronic conductors, and calculate the resistance of the conductor by determining the current through the conductor and the voltage drop across the conductor according to Ohm's law: R=UI, where R is the resistance, U is the voltage, and I is the current. We measure the geometry of the sample to be tested, which in turn allows us to calculate the conductivity.

6.2.7 THERMAL-PHYSICAL PERFORMANCE MEASUREMENT

The testing mechanisms for thermal conductivity are mainly categorized into steady-state testing and transient method testing. Common steady-state methods include the flat plate method and the guard plate method; transient methods include the hot plate method, the laser method, and the hot wire method. In practice, the steady-state method affects the accuracy of measurement due to too many factors is not convenient to operate. Therefore, the transient hot wire method is generally used more often. We briefly summarized the different thermal conductivity test methods, as shown in Figure 8.3.

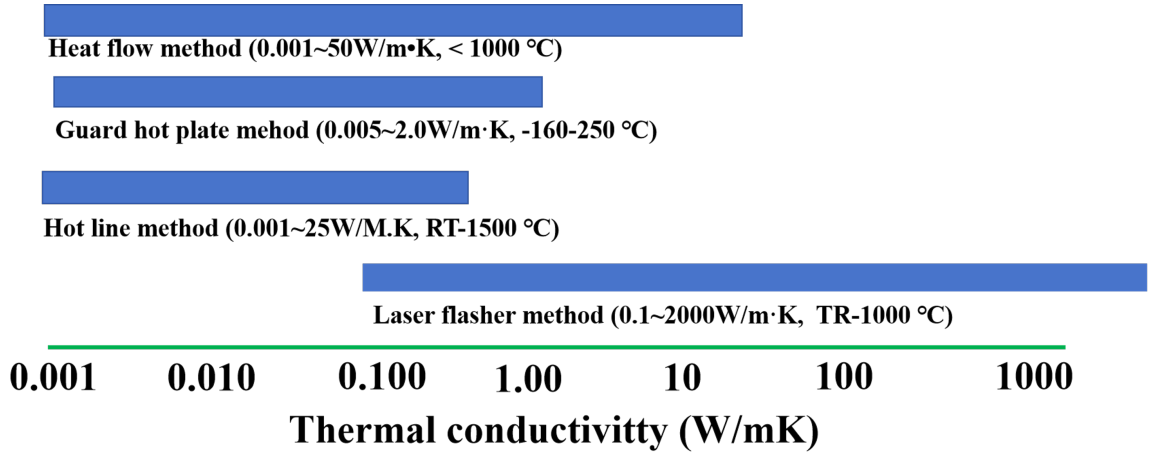

Figure 6.3: Part instruments suitable for thermal conductivity testing and their detection ranges.

Hot Disk

The Hot Disk method relies on transient planar heat source technology and is by far one of the simplest and most accurate methods available. Hot Disk's probe is a sheet-like structure with a thermally resistive material, nickel, on the inside and a polyimide composition on the outside, which is usually used as both a heat source and a temperature sensor. The coefficient of thermal resistance of the nickel wire and the relationship between temperature and resistance are linear. The change in resistance can be used to determine the heat loss, allowing a mathematical model to be fitted to derive the thermal conductivity of the sample. Since the heat transfer depends on the temperature change and transient time of the probe, the test model is based on the premise that the sample surrounding the probe is infinite or that the heat flow can be trnasferred through the sample during the test. In our tests, we use the Hot Disk model A, the probe model C. In our experiment, we positioned sensors in two cylindrical samples, each with at least one flat side (Figure 8.4a). we optimized data characterization by adjusting power and test time, resulting in a transient warming of 1.5-5 K within an overall specific characterization time of 0.33-1s, displaying a horizontally dispersed scatter plot in the temperature drift diagram. Additionally, residual were considered.Mathematical simulations fitted to the samples allowed

us to obtain their thermal conductivity, specific heat of volume, and thermal diffusion coefficient. For the Hot Disk test, the range extends from 0.005 to 500 W/mK with a test accuracy of ±3%, unaffected by contact thermal resistance. This method yields results closer to the material's intrinsic thermal conductivity and is applicable to a variety of materials. However, caution is advised when testing molten salts, alkalis, fluorine-containing materials, as well as samples with non-flat, sharp, or hard surfaces, as these may damage the sensor to some extent during testing. The equation for the rete of warming of the probe surface can be expresses as:

$$\Delta T_S(|\tau|) = P_0 \left(|\pi^{\frac{3}{2}} r \lambda|^{-1} \right) D(|\tau|) \tag{6.1}$$

The equation for calculating thermal conductivity from the transient curve, given P_0 as the probe output power and r as the radius of the probe, can be expressed as:

$$\tau = \left(\frac{t}{\theta} \right)^{\frac{1}{2}}, \quad \theta = \frac{r^2}{\kappa}, \quad \rho C_p = \frac{\lambda}{\kappa} \tag{6.2}$$

$$k = \frac{P_0 \cdot r}{2 \cdot \frac{dT}{dt} \cdot A} \tag{6.3}$$

where k is the thermal conductivity of the material surrounding the probe, $\frac{dT}{dt}$ is the rate of temperature change with respect to time, and A is the cross-sectional area of the probe.

Transient Hot Bridge

The transient hot bridge is tested by Linseis THB 100. The instrument's thermal conductivity test range is 0.02-3, with an accuracy of plus or minus 3%. The thermal diffusion rate ranges from 0.05 to 10. The temperature test range spans from 25 to 200 degrees Celsius. The smallest sample size accommodated is 4x4x4 units. The sensor types employed include insulated caption sensors (40x20 mm) and hot point sensors (4x4 mm).

Limiting oxygen index

There are numerous test methods available to assess the combustion performance of materials. These range from traditional methods like the Limiting Oxygen Index (LOI) method, the horizontal and vertical combustion methods outlined in UL standards, and the NBS smoke box method, to advanced methods such as the Cone Calorimeter (CONE) method and the Miniature Calorimeter (MCC) method, among others. In this thesis, we employ the Oxygen Index (LOI) method and the Cone Calorimeter (CONE) method to evaluate the performance of our materials

The LOI represents the minimum concentration of oxygen required to sustain the combustion of a polymer and is expressed as a percentage of oxygen by volume. It is determined by adjusting the ratio of oxygen to nitrogen in the environment where the burning specimen is located, gradually reducing the oxygen level until a critical threshold is reached. The LOI is influenced by factors such as pressure, temperature, and the type of inert gas (flammable or combustion-assisting) added. The equation for calculating LOI is: LOI (%)=Lower Explosive Limit (%)×Oxygen Moles (mol). LOI serves as an indicator of a material's flammability—the higher the value, the more resistant to combustion it is. If a material's LOI exceeds 21%, it is considered flame-resistant; if the LOI surpasses 27%, it indicates high refractoriness to combustion. In our experiments, we utilized a Fire Testing Technology Oxygen Index Apparatus ISO 4589-3–NES 715 (Edenharter, Germany) to assess the flame resistance of materials under 100% oxygen concentrations with methane.

Thermal Infrared Imaging Instruments

Modern thermal imaging cameras operate by using optoelectronic devices to detect and measure radiation, establishing a correlation between this radiation and the surface temperature. All objects above absolute zero (-273℃) emit infrared radiation. An infrared thermal imager employs an infrared detector and an optical imaging objective to receive a graphical representation of the energy distribution of the infrared radiation from the target under test. This energy distribution is reflected on the photosensitive element of the infrared detector, producing an infrared thermogram that corresponds to the heat distribution field on the surface of the object. The thermal images used in this thesis is instrument Fluke TiS55+. Before use, coefficients such as temperature and humidity are calibrated to ensure accurate measurements.

6.2.8 ELECTROCHEMICAL PROPERTIES CHARACTERIZATION

Three electrode system

All electrochemical properties were performed in a standard three-electrode system with a Gamry Inter1010E. The three electrodes were platinum wire electrodes, silver/silver chloride electrodes, and platinum carbon electrodes. All the working electrodes were cleaned before data collection by performing a steady-state cyclic voltammetry (CV) scan for three cycles in the potential range of $-0.16\,\mathrm{V}$–$1\,\mathrm{V}$ versus Ag/AgCl (saturated KCl solution) at $50\,\mathrm{mV\,s^{-1}}$ in 0.5 mol saturated N_2-purged H_2SO_4. All electrochemical experiments were carried out at room temperature and ambient pressure.

For CO stripping voltammetry, nitrogen was introduced into the electrolyzer to achieve saturation, and the change in current under constant pressure was monitored while introducing CO for testing.

For the preparation of working electrodes, the ink solution consisted of 0.35 mg of PtAg-NTs, 0.25 mL of ethanol, 0.084 mL of DI-H_2O, and 10 μL of Nafion solution, corresponding to a concentration of 3.0 mg mL^{-1}. The mixture was sonicated for 30 minutes before use.

Home-made direct methanol fuel cell setup

To further study the application of materials, we built a brief direct methanol fuel cell test system to meet the impact of the application of catalysts in fuel cells.

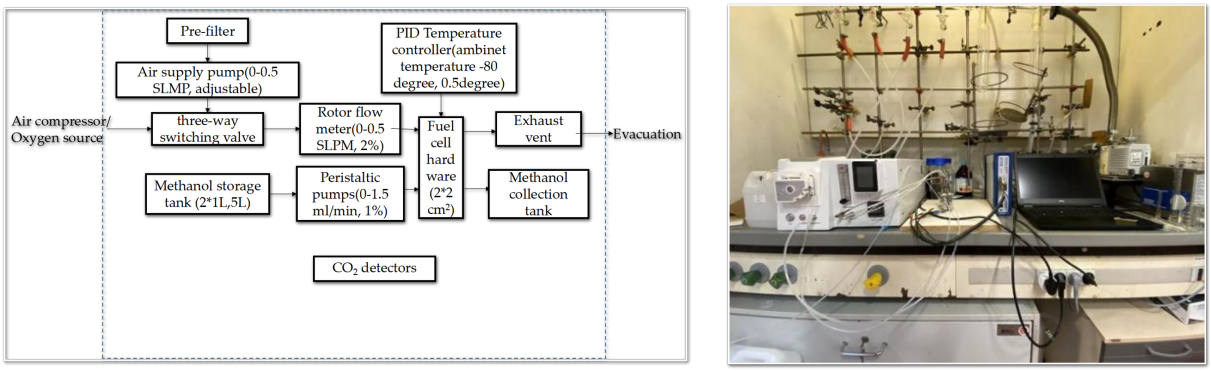

Figure 6.4: Theoretical design drawing and corresponding laboratory display drawing.

The membrane electrode used in the cell is prepared by the following steps:

The anode-supported catalyst was prepared using either a sponge or a commercial catalyst, while the cathode consisted of Pt black (Johnson–Matthey). Catalyst layers were formed on teflonized carbon paper (TGPH-090) substrates using catalyst inks containing the appropriate weight percent of a Nafion ionomer solution.

For unit cell tests, membrane electrode assemblies (MEAs) were fabricated by pressing the prepared cathode and anode layers onto both sides of a pre-treated Nafion 117 membrane at 110 ℃ and 800 psi (5.5 MPa) for 3 minutes. The membrane was pre-treated by boiling in 3 wt% H_2O_2 for 1 hour, followed by 0.5 M H_2SO_4 for 1 hour.

The cell performance was evaluated in a direct methanol fuel cell (DMFC) with a 2 cm^2 cross-sectional area using a potentiometer (WMPG-3000), which recorded the cell under a constant current. A 2 M methanol solution with a flow rate of 1 ± 1 cm^3/min was supplied using a Masterflex liquid micropump, and a dry O_2 flow was regulated at 500 cm^3/min using a flow meter.

6.3 EXPERIMENTAL PROCEDURES

6.3.1 PREPARATION OF RAW MATERIALS

Preparation of SiO_2 sponge

Tetraethyl orthosilicate (TEOS), Milli-Q water, and phosphoric acid were used for the preparation of a SiO_2 sol at a wt% ratio of 1:1:0.01. A PVP solution was prepared by adding 10% PVP powder to H_2O. These solutions were stirred for 8 h, respectively. Then, the PVP solution was heated in an oil bath at 90 °C until completely dissolved. The precursor solution was obtained by mixing equal parts of SiO_2 sol and PVP solution and stirring for 4 h.

Electrospinning was performed using an Elub 848 spinning instrument. During electrospinning, the positive voltage was 20 kV, the negative voltage was 0.7 kV, the spinning speed was 1 mL h^{-1}, the receiving distance was 17 cm, the syringe volume was 3 mL, the tip size was 0.80×22 mm, the relative humidity was 10%, and the temperature was 21.7 °C. The spun SiO_2 nanofiber membrane was heated in air to 800 °C at a heating rate of 5 °C min^{-1} and then cooled.

As an example, a SiO_2 sponge with a bulk density of 3 mg cm^{-3} was prepared. First, a gel was obtained by mixing 5 g TEOS, 20 g H_2O, and 0.02 g H_3PO_4, followed by stirring for 2 h. Then, 1 g SiO_2 sol and 0.05 g SiO_2 membrane were dispersed in 18.8 g of H_2O by homogenization (IKA Disperser) at 10 000 rpm for 10 min, followed by stirring for 0.5 h at 100 rpm. The resulting solution was poured into molds and frozen in a freezer for 12 h, then freeze-dried for 36 h. The SiO_2 sponge was heated in air to 800 °C at a heating rate of 5 °C min^{-1} and then cooled. The silica fibers prepared in the second experiment were similar to those in the first, except that the spinning aid was changed from PVP to PVA.

Preparation of AgNWs

AgNWs (AgNWs) were synthesized using the polyol process according to a previous report. Ethylene glycol (EG, 160 mL) was preheated at 130 °C for 1 h under 500 rpm magnetic stirring. A total of 0.2 mL of NaCl (0.01985 g mL^{-1}), 0.1 mL of $FeCl_3$ (0.0054 g mL^{-1}), 20.76 mL of PVP (0.042 g mL^{-1}), and 20.76 mL of $AgNO_3$ (0.042 g mL^{-1}) were added to the above-mentioned hot EG. After the reaction at 130 °C for 6 h, the solution was cooled to room temperature, and ethanol and acetone (1:2 v/v) were added to flocculate the AgNWs. After purification three times, the AgNWs were centrifuged at 4000 rpm for 5 min and then dispersed in water to obtain dispersions with different concentrations. The AgNWs used in the subsequent experiments were obtained by adjusting the reaction temperature and reaction time based on this procedure to meet specific requirements.

6.3.2 PREPARATION OF COMPOSITE MATERIALS

Preparation of AgNWs@PEI@SiO_2 sponge

The preparation steps of the AgNWs@PEI@SiO_2 composite sponge are illustrated in Figure S1c. As a representative example, the distribution of AgNWs was investigated at a PEI concentration of $1\,g\,L^{-1}$. The SiO_2 sponge (diameter: 1.6 cm; height: 1.2 cm) was immersed in PEI aqueous solutions of various concentrations (0, 0.5, 1.0, 1.5, and $2.0\,g\,L^{-1}$) for 30 s, then removed and rinsed three times with water. The treated sponges were then immersed in an aqueous AgNW dispersion ($12\,mg\,mL^{-1}$) and shaken at 250 rpm for 36 h. Afterward, the composite sponges were rinsed with water and freeze-dried to obtain the final products. The samples were designated as AgNW@PEI0@SiO_2, AgNW@PEI0.5@SiO_2, AgNW@PEI1@SiO_2, AgNW@PEI1.5@SiO_2, and AgNW@PEI2@SiO_2, corresponding to PEI concentrations of 0, 0.5, 1.0, 1.5, and $2.0\,g\,L^{-1}$, respectively.

Preparation of Ag/SiO_2 sponge

An AgNWs/SiO_2 sponge sample was prepared by mixing AgNWs, silica fibers, and silica gel in a specific proportion, pouring the resulting solution into a mold, and freeze-drying. The silica gel was synthesized by mixing 5.0 g tetraethyl orthosilicate (TEOS), 20 g H_2O, and 0.002 g H_3PO_4, followed by stirring for 2 h. The obtained sponge sample had a mass of 15.25 ± 0.2 mg and a volume of approximately $5.65\,cm^3$, corresponding to a bulk density of about $3\,mg\,cm^{-3}$. The volume fractions of AgNWs in the samples—designated AgNWs1/SiO_2 sponge, AgNWs2/SiO_2 sponge, AgNWs3/SiO_2 sponge, AgNWs4/SiO_2 sponge, and AgNWs5/SiO_2 sponge—were 6.7%, 13.3%, 20.2%, 25.0%, and 29%, respectively.

Preparation of PtAg nanotubes

PtAg bimetallic nanotubes (PtAgNTs) were synthesized via a solution-phase method. AgNWs and H_2PtCl_6 were rapidly injected into an ethylene glycol (EG) solution maintained at 95 ℃. The solution color changed quickly from gray to dark brown, indicating the formation of PtAgNTs. After an additional 30 min reaction at 95 ℃, the product was collected by centrifugation and washed several times with an ammonia/H_2O mixture, followed by freeze-drying at −60 ℃ before use (as shown in Figure 8.5).

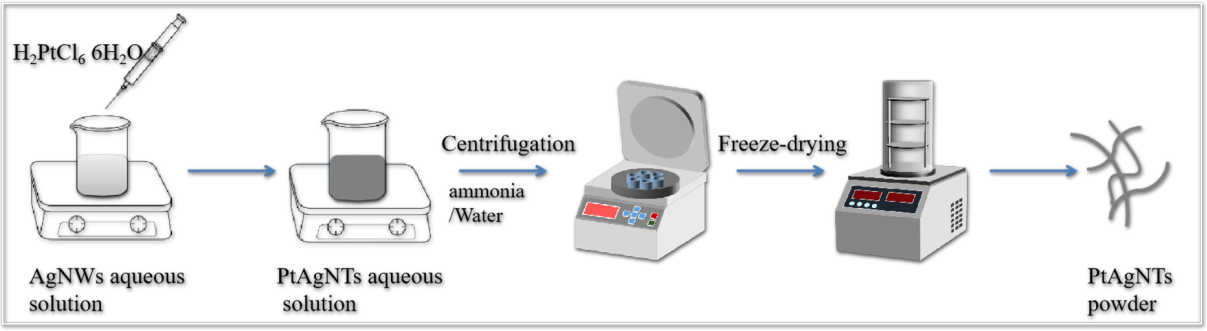

Figure 6.5: Schematic illustration of the experimental procedure.

ACKNOWLEDGEMENTS

During my doctoral studies, I received invaluable help and support from many people, for which I am deeply grateful.

First and foremost, I would like to express my sincere appreciation to my supervisor Prof. Dr. Andreas Greiner. Thank you for your guidance, patience, and understanding throughout my PhD journey. Although I sometimes insisted on my own ideas, I gradually came to realize that your suggestions and insights were always well-founded. Especially towards the end of my doctoral work, I understood that the directions you encouraged me to explore were not only beneficial to this research, but also important for my personal growth. I am truly grateful for your mentorship, which has shaped my way of thinking and helped me become a better person.

I am also grateful to Prof. Dr. Seema Agarwal for her valuable feedback during our group meetings. Her comments and suggestions prompted me to consider my research from alternative viewpoints, which has been greatly beneficial to the development of my work.

I would also like to express my gratitude to Prof. Dr. Bin Ding and Prof. Dr. Yitao Liu for their guidance on the preparation of silica sponges, as well as for their collaboration and support in other aspects of the work.

I would like to express my special thanks to Prof. Dr. Markus Retsch for his support and suggestions regarding thermal characterization, and to Sahoo Sudeshna for her help with thermal conductivity measurements. I also appreciate Prof. Dr. Jürgen Senker's support with BET testing and Johannes Guellich's assistance in this area. Additionally, I want to thank Prof. Dr. Roth, Christina allowing for the electrochemical testing, and Dr. Loukrakpam Jalan, Rameshwori for their assistance with CO stripping measurements. I am also grateful to Prof. Dr. Francesco Ciucci for his valuable suggestions regarding my research on the catalytic performance toward the methanol oxidation reaction. I appreciate Prof. Dr. Holger Ruckdäschel for providing the opportunity for in-situ electron microscopy testing, and I thank Agarkov, Natalja, and Kulig, Agata for their help during these tests. Thanks to Prof. Andreas Fery for agreeing to conduct TEM testing, as well as to Dr. Petr Formanek and Dr. Dong Yue for their support in this area. My thanks also

go to Prof. Dr. Matteo Bianchini for supporting XRD testing and to Wißmeier, Lena for her assistance. I am grateful to Prof. Dr. Meike Nicole Leiske for her help, and to Dr. Mansfeld, Ulrich and Heider, Martina for their training and discussions regarding TEM and SEM testing. I would like to thank Bretschneider, Felix for his help with TEM and ICP testing, Dr. Giesa, Reiner for the introduction to XRD testing, and Benker, Lothar for his support with Hotdisk measurements, as well as Schmitt, Thomas for assistance with IT issues and Simon Knorr for ICP-OES measurements. I want to thank Dr. Gao Qiang for his support in studies when I first joined this new group, as well as Dr. Liao Xiaojian and his wife for their assistance in my daily life, and Dr. Xu, Chengzhang for her support in both my studies and life. I would like to acknowledge the use of the ChatGPT language model as a tool to improve linguistic expression and assist with LaTeX formatting during the preparation of this dissertation. I am grateful to SGL Carbon company for generously providing the carbon paper used for the fuel cell performance evaluations.

Additionally, I would like to thank all my colleagues in the MC 2 group, working with you has been both beneficial and enjoyable. I would like to thank my friends for their encouragement and support during my PhD, which allowed me to gain new perspectives through our diverse backgrounds and experiences. A special thanks goes to Prof. Dr. Hou Haoqing, whose constant encouragement has warmed.

Finally, I would like to express my sincerest gratitude to my family. They have always been there for me, especially during times when I needed to make difficult choices, providing me with unconditional support. I will forever cherish their love and encouragement.

I also wish to express my expectations for my own development. Ultimately, I hope to become a specialist in the development of tactile sensing materials for robotic applications. Additionally, regardless of the position I ultimately choose or am able to pursue, I will continue to refine my expertise, further develop my skills, and do my best to contribute to and support others.

Once again, I would like to thank everyone who has helped me along the way. It is your support that has brought me to this point.

REFERENCES

[1] Srinivasa Kartik Nemani, Rama Kishore Annavarapu, Behrouz Mohammadian, Asif Raiyan, Jamie Heil, Md Ashraful Haque, Ahmed Abdelaal, and Hossein Sojoudi. Surface modification of polymers: methods and applications. *Advanced Materials Interfaces*, 5(24):1801247, 2018.

[2] N. Abid, A. M. Khan, S. Shujait, K. Chaudhary, M. Ikram, M. Imran, J. Haider, M. Khan, Q. Khan, and M. Maqbool. Synthesis of nanomaterials using various top-down and bottom-up approaches, influencing factors, advantages, and disadvantages: A review. *Advances in Colloid and Interface Science*, 300:102597, 2022.

[3] A. A. Aboalhassan, J. Yan, Y. Zhao, K. Dong, X. Wang, J. Yu, and B. Ding. Self-assembled porous-silica within n-doped carbon nanofibers as ultra-flexible anodes for soft lithium batteries. *iScience*, 16:122–132, 2019.

[4] S. Agarwal and A. Greiner. On the way to clean and safe electrospinning—green electrospinning: emulsion and suspension electrospinning. *Polymers for Advanced Technologies*, 22:372–378, 2011.

[5] S. Agarwal, A. Greiner, and J. H. Wendorff. Functional materials by electrospinning of polymers. *Progress in Polymer Science*, 38:963–991, 2013.

[6] R. Ahmad and M. Shah. Hydrothermally synthesised nickel oxide nanostructures on nickel foam and nickel foil for supercapacitor application. *Ceramics International*, 49:6470–6478, 2023.

[7] S. A. Al-Ajlan. Measurements of thermal properties of insulation materials by using transient plane source technique. *Applied Thermal Engineering*, 26:2184–2191, 2006.

[8] J. O. M. Amarah. Removal of methylene blue from industrial wastewater in palestine using polysiloxane surface modified with bipyrazolic tripodal receptor, 2015. Thesis / Report.

[9] L. Aspillaga, D. J. Bautista, S. N. Daluz, K. Hernandez, J. A. Renta, and E. C. R. Lopez. Nucleation and crystal growth: Recent advances and future trends. *Engineering Proceedings*, 56:22, 2023.

[10] A. A. Babar, X. Wang, N. Iqbal, J. Yu, and B. Ding. Tailoring differential moisture transfer performance of nonwoven/polyacrylonitrile-sio$_2$ nanofiber composite membranes. *Advanced Materials Interfaces*, 4:1700062, 2017.

[11] H. Bai, Y. Chen, B. Delattre, A. P. Tomsia, and R. O. Ritchie. Bioinspired large-scale aligned porous materials assembled with dual temperature gradients. *Science Advances*, 1:e1500849, 2015.

[12] N. Baig, I. Kammakakam, and W. Falath. Nanomaterials: A review of synthesis methods, properties, recent progress, and challenges. *Materials Advances*, 2:1821–1871, 2021.

[13] A. Bandyopadhyay, I. Mitra, S. B. Goodman, M. Kumar, and S. Bose. Improving biocompatibility for next generation of metallic implants. *Progress in Materials Science*, 133:101053, 2023.

[14] V. Barragán and A. Heinzel. Estimation of the membrane methanol diffusion coefficient from open circuit voltage measurements in a direct methanol fuel cell. *Journal of Power Sources*, 104:66–72, 2002.

[15] M. Becucci, M. Bracciali, G. Ghini, C. Lofrumento, G. Pietraperzia, M. Ricci, L. Tognaccini, S. Trigari, C. Gellini, and A. Feis. Silver nanowires as infrared-active materials for surface-enhanced raman scattering. *Nanoscale*, 10:9329–9337, 2018.

[16] F. Bresciani, A. Casalegno, M. Zago, and R. Marchesi. A parametric analysis on dmfc anode degradation. *Fuel Cells*, 14:386–394, 2014.

[17] R. P. Buck. Kinetics of bulk and interfacial ionic motion: microscopic bases and limits for the nernst–planck equation applied to membrane systems. *Journal of Membrane Science*, 17:1–62, 1984.

[18] D. E. Cagliostro and M.-T. S. Hsu. Method for waterproofing ceramic materials, 1998.

[19] J. Cao, Y. Zuo, D. Wang, J. Zhang, and S. Feng. Functional polysiloxanes: a novel synthesis method and hydrophilic applications. *New Journal of Chemistry*, 41:8546–8553, 2017.

[20] X. Cao, Y. Han, C. Gao, X. Huang, Y. Xu, and N. Wang. Ptag nanowires: facile synthesis and their applications as excellent oxygen reduction electrocatalysts for label-free electrochemical immunoassay. *Journal of Materials Chemistry A*, 1:14904–14909, 2013.

[21] X. Cao, N. Wang, Y. Han, C. Gao, Y. Xu, M. Li, and Y. Shao. Ptag bimetallic nanowires: Facile synthesis and their use as excellent electrocatalysts toward low-cost fuel cells. *Nano Energy*, 12:105–114, 2015.

[22] C.-W. Chang, D. Okawa, H. Garcia, A. Majumdar, and A. Zettl. Breakdown of fourier's law in nanotube thermal conductors. *Physical Review Letters*, 101:075903, 2008.

[23] C. Chen, H. Wang, Y. Xue, Z. Xue, H. Liu, X. Xie, and Y.-W. Mai. Structure, rheological, thermal conductive and electrical insulating properties of high-performance hybrid epoxy/nanosilica/agnws nanocomposites. *Composites Science and Technology*, 128:207–214, 2016.

[24] C. Chen, L. Wang, G. Jiang, J. Zhou, X. Chen, H. Yu, and Q. Yang. Study on the synthesis of silver nanowires with adjustable diameters through the polyol process. *Nanotechnology*, 17:3933, 2006.

[25] S. Chen, Z. Li, J. Huang, L. Sha, and Z. Lu. Electrically conductive yet insulating aramid nanofiber janus films via gel–gel assembling for flexible motion sensing and joule heating. *Chemical Engineering Journal*, 457:141021, 2023.

[26] Y. Chen, Z. Fan, Z. Zhang, W. Niu, C. Li, N. Yang, B. Chen, and H. Zhang. Two-dimensional metal nanomaterials: synthesis, properties, and applications. *Chemical Reviews*, 118:6409–6455, 2018.

[27] J. Chojnowski and M. Cypryk. Synthesis of linear polysiloxanes. In *Silicon-containing polymers: the science and technology of their synthesis and applications*, pages 3–41. 2000.

[28] J. Chojnowski, M. Cypryk, W. Fortuniak, M. Ścibiorek, and K. Rózga-Wijas. Synthesis of branched polysiloxanes with controlled branching and functionalization by anionic ring-opening polymerization. *Macromolecules*, 36:3890–3897, 2003.

[29] A. I. Cooper. Polymer synthesis and processing using supercritical carbon dioxide. *Journal of Materials Chemistry*, 10:207–234, 2000.

[30] J. Cruz and R. Fangueiro. Surface modification of natural fibers: a review. *Procedia Engineering*, 155:285–288, 2016.

[31] S. Deville. Ice-templating, freeze casting: Beyond materials processing. *Journal of Materials Research*, 28:2202–2219, 2013.

[32] Y. Ding, H. Hou, Y. Zhao, Z. Zhu, and H. Fong. Electrospun polyimide nanofibers and their applications. *Progress in Polymer Science*, 61:67–103, 2016.

[33] X. Dong, L. Cao, Y. Si, B. Ding, and H. Deng. Cellular structured cnts@sio2 nanofibrous aerogels with vertically aligned vessels for salt-resistant solar desalination. *Advanced Materials*, 32:1908269, 2020.

[34] A. S. Dorcheh and M. Abbasi. Silica aerogel; synthesis, properties and characterization. *Journal of Materials Processing Technology*, 199:10–26, 2008.

[35] L. Dou, X. Zhang, X. Cheng, Z. Ma, X. Wang, Y. Si, J. Yu, and B. Ding. Hierarchical cellular structured ceramic nanofibrous aerogels with temperature-invariant superelasticity for thermal insulation. *ACS Applied Materials & Interfaces*, 11:29056–29064, 2019.

[36] A. S. Douk, H. Saravani, and M. Noroozifar. One-pot synthesis of ultrasmall ptag nanoparticles decorated on graphene as a high-performance catalyst toward methanol oxidation. *International Journal of Hydrogen Energy*, 43:7946–7955, 2018.

[37] Y. Dror, W. Salalha, R. Avrahami, E. Zussman, A. L. Yarin, R. Dersch, A. Greiner, and J. H. Wendorff. One-step production of polymeric microtubes by co-electrospinning. *Small*, 3:1064–1073, 2007.

[38] G. Duan, S. Jiang, V. Jérôme, J. H. Wendorff, A. Fathi, J. Uhm, V. Altstädt, M. Herling, J. Breu, and R. Freitag. Ultralight, soft polymer sponges by self-assembly of short electrospun fibers in colloidal dispersions. *Advanced Functional Materials*, 25:2850–2856, 2015.

[39] P. R. Dvornic. Thermal properties of polysiloxanes. In *Silicon-containing polymers*, pages 185–212. 2000.

[40] K. Eid. Rapid one-step aqueous synthesis of porous ptag wavy nanochains for methanol electrooxidation with a high co-tolerance. *Journal of Electroanalytical Chemistry*, 961:118207, 2024.

[41] A. M. El-Khawaga, A. Zidan, and A. I. Abd El-Mageed. Preparation methods of different nanomaterials for various potential applications: A review. *Journal of Molecular Structure*, 1281:135148, 2023.

[42] M. H. Esfe, P. M. Behbahani, A. A. Arani, and M. R. Sarlak. Thermal conductivity enhancement of sio_2–mwcnt (85: 15%)–eg hybrid nanofluids. *Journal of Thermal Analysis and Calorimetry*, 128:249–258, 2017.

[43] F. R. Espinoza-Quiñones, M. Romani, C. E. Borba, A. N. Módenes, C. F. Utzig, and I. C. Dall'Oglio. A mathematical approach based on the nernst-planck equation for the total electric voltage demanded by the electrocoagulation process. *Chemical Engineering Science*, 220:115626, 2020.

[44] D. Fang, Y. T. Liu, B. Ding, and A. Greiner. Polyethyleneimine controlled impregnation of silver nanowires on electrospun ceramic sponges. *Macromolecular Materials and Engineering*, page 2400017, 2024.

[45] K. Feng, G.-Y. Hung, J. Liu, M. Li, C. Zhou, and M. Liu. Fabrication of high performance superhydrophobic coatings by spray-coating of polysiloxane modified halloysite nanotubes. *Chemical Engineering Journal*, 331:744–754, 2018.

[46] M. Feng, J. He, S. Song, S. Zhang, and X. Zhang. Recent progress on polysiloxane-based materials for flexible electronics. *Journal of Materials Chemistry C*, 9:879–896, 2021.

[47] X. Feng, Y. Yang, X. Zhang, X. Li, S. Ma, H. Zhang, and W. Zhang. Mechanically robust and thermally insulating silica aerogels: a review. *Journal of Non-Crystalline Solids*, 550:120344, 2020.

[48] Y. Feng, Y. Li, C. Wang, Y. Wang, and S. Bai. Metallic nanowire networks for flexible electronics: materials, fabrication, and applications. *Advanced Materials*, 35:2208002, 2023.

[49] H. Fischer. Polymer nanocomposites: from fundamental research to specific applications. *Materials Science and Engineering: C*, 23:763–772, 2003.

[50] Q. Fu, J. Ran, W. Li, M. Xu, J. Wei, and X. Li. A novel sio_2 aerogel–supported ag nanowire composite for enhanced thermal and electrical performance. *Composites Science and Technology*, 224:109476, 2022.

[51] Y. Fu, T. Wang, R. Zhao, Z. Zhu, Z. Wu, and H. Yu. Highly stretchable polysiloxane elastomers for wearable sensors: design strategies and applications. *Progress in Polymer Science*, 129:101568, 2022.

[52] H. Gao, G. Duan, Y. Li, K. Dai, B. Ding, and S. Zhang. Thermal transport in polymer nanocomposites. *Materials Today Physics*, 9:100099, 2019.

[53] S. Gao, Z. Tang, T. Li, X. Zhang, and H. Liu. Conductive silver nanowire-based aerogels: structure design and multifunctional applications. *Nano-Micro Letters*, 12:134, 2020.

[54] X. Gao, X. Li, L. Zhang, C. Xu, F. Kang, Q. Yang, and B. Li. Flexible, stretchable, and wearable supercapacitors based on conducting polymer hydrogel aerogels. *Advanced Energy Materials*, 11:2003201, 2021.

[55] D. García-Gutiérrez, A. Nogales, D. R. Rueda, and T. A. Ezquerra. Polymer nanostructures formed by nanoconfinement and their application in membranes. *Nanotechnology*, 21:375301, 2010.

[56] J. Ge, B. Lei, Y. Wang, X. Song, X. Zhang, and J. Liu. Mesoporous silica-based functional nanomaterials: synthesis, structure, and applications. *Journal of Materials Chemistry B*, 8:10752–10777, 2020.

[57] S. Gong, L. W. Yap, B. Zhu, and W. Cheng. Skin-inspired electronic devices for wearable health monitoring. *Advanced Functional Materials*, 31:2008081, 2021.

[58] T. Gong, R. Liu, X. Yan, and Y. Zhang. Sol-gel derived silica aerogels: progress and prospects. *RSC Advances*, 5:11657–11673, 2015.

[59] R. Goyal, S. Kumar, and R. Chauhan. Sio_2 nanofluid based heat transport systems: a comprehensive review. *Renewable and Sustainable Energy Reviews*, 82:1843–1867, 2018.

[60] C. Guo, C. Yu, J. Yang, L. Zhao, and Y. Zhou. Superelastic silica nanofiber aerogels for thermal insulation. *ACS Nano*, 15:1234–1243, 2021.

[61] H. Guo, M. Li, Y. Song, J. Huang, S. Chen, and L. Wu. Hydrophobic silica aerogels with improved mechanical performance via polymer crosslinking. *Microporous and Mesoporous Materials*, 283:258–266, 2019.

[62] R. Guo, J. Fang, L. Zhang, L. Liu, H. Li, X. Wang, and B. Chen. Highly conductive ag nanowire networks for flexible electrodes: strategies and applications. *Journal of Materials Chemistry A*, 10:10562–10588, 2022.

[63] S. Gupta, A. Singh, and R. Sharma. Applications of nanomaterials in catalysis: a review. *Materials Today: Proceedings*, 46:10071–10077, 2021.

[64] S. N. Habisreutinger, T. Leijtens, G. E. Eperon, S. D. Stranks, R. J. Nicholas, and H. J. Snaith. Carbon nanotube/polymer composites as novel electrode materials for perovskite solar cells. *Nano Letters*, 14:5561–5568, 2014.

[65] L. Han, X. Liu, C. Zhang, and H. Zhang. Flexible aerogels for heat and sound insulation: design, fabrication, and applications. *Advanced Materials*, 34:2108184, 2022.

[66] X. Han, Y. Liu, Y. Zhang, X. Zhao, and H. Xu. Thermal insulating porous silica aerogels: design strategies and applications. *Journal of Sol-Gel Science and Technology*, 95:601–617, 2020.

[67] Y. Han, C. Chen, D. Li, Z. Zhang, and X. Yang. Electrospun polymer nanofibers for flexible energy devices. *Energy Storage Materials*, 39:159–177, 2021.

[68] T. Hao, Y. Wang, L. Zhang, and M. Liu. A review of polysiloxane-based hybrid aerogels. *Polymer Reviews*, 58:1–35, 2018.

[69] J. He, J. Huang, Z. Lin, H. Liang, and X. Fan. Silver nanowire networks: synthesis, structure, properties and applications. *Advanced Functional Materials*, 31:2009672, 2021.

[70] L. He, Z. Wang, S. Liu, and Y. Chen. Flexible and highly conductive ag nanowire-based films for wearable electronics. *ACS Applied Materials & Interfaces*, 11:1893–1901, 2019.

[71] S. He, B. Yuan, Q. Xie, and X. Huang. Hydrophobic silica aerogels for oil–water separation: fabrication, structure and applications. *Journal of Colloid and Interface Science*, 599:522–538, 2021.

[72] X. He, Y. Cheng, J. Li, and W. Yu. Recent advances in freeze-casting of porous ceramics. *Ceramics International*, 46:19505–19518, 2020.

[73] Y. He, J. Zhang, M. Shen, and C. Li. Electrochemical properties of ptag nanostructures for methanol oxidation reaction. *Electrochimica Acta*, 302:316–324, 2019.

[74] J. Hernandez, A. Torres, M. Perez, and C. Rios. Silica aerogels reinforced with fiber networks: mechanical and thermal performance. *Materials & Design*, 216:110688, 2022.

[75] G. Hoang, T. Pham, and V. Nguyen. Nanomaterials in fuel cell catalysts: a review. *International Journal of Hydrogen Energy*, 45:24378–24398, 2020.

[76] H. Hou, H. Zhang, B. Liang, and X. Xu. Synthesis and functionalization of polysiloxanes for membrane applications. *Progress in Organic Coatings*, 156:106307, 2021.

[77] J. Hu, J. Li, H. Zhou, and J. Wang. Synthesis and catalytic properties of ptag alloy nanostructures: a review. *Catalysts*, 12:642, 2022.

[78] L. Hu, Y. Yang, C. Chen, and N. Wang. Electrospun ceramic nanofibers and their applications. *Nanoscale*, 5:4186–4194, 2013.

[79] M. Hu, M. Li, J. Zhou, F. Wang, and S. Yang. Porous polymer–metal nanowire composites for electromagnetic shielding. *Composites Part B: Engineering*, 177:107303, 2019.

[80] X. Hu, Y. Liang, R. Wu, and J. Liu. Hydrophobic and thermally insulating silica aerogels: recent advances. *Chemical Engineering Journal*, 455:140893, 2023.

[81] C. Huang, T. Liu, Y. Li, and X. Zhang. Nanofiber-based flexible materials for wearable sensors. *Advanced Materials Technologies*, 6:2100284, 2021.

[82] H. Huang, Z. Yang, R. Liu, and J. Zhao. Freeze casting of porous materials: mechanisms, structures and applications. *Materials Today*, 31:65–90, 2019.

[83] J. Huang, S. Li, Y. Chen, and W. Zhang. Mechanisms of catalytic methanol oxidation over pt-based electrocatalysts. *Electrochemical Energy Reviews*, 3:252–279, 2020.

[84] Z. Huang, Q. He, L. Chen, and M. Wang. Surface modification of ag nanowires for improved dispersion and stability. *Colloids and Surfaces A*, 648:129350, 2022.

[85] C. Hui, Y. Zhao, L. Wei, and D. Xu. Porous ceramics for thermal insulation: a review. *Journal of the European Ceramic Society*, 41:4512–4536, 2021.

[86] S. Kumar, R. Singh, T. P. Singh, and B. L. Sethi. Surface modification by electrical discharge machining: A review. *Journal of Materials Processing Technology*, 209:3675–3687, 2009.

[87] S. Kurmaz and A. Pyryaev. Synthesis of n-vinyl-2-pyrrolidone-based branched copolymers via crosslinking free-radical copolymerization in the presence of a chain-transfer agent. *Polymer Science Series B*, 52:1–8, 2010.

[88] B. E. Kwak, H. J. Yoo, E. Lee, and D. H. Kim. Large-scale centrifugal multispinning production of polymer micro- and nanofibers for mask filter application with a potential of cospinning mixed multicomponent fibers. *ACS Macro Letters*, 10:382–388, 2021.

[89] Y. Lai, G. Du, Z. Zheng, Y. Dong, H. Li, Q. Kuang, and Z. Xie. Facile synthesis of clean ptag dendritic nanostructures with enhanced electrochemical properties. *Inorganic Chemistry Frontiers*, 7:1250–1256, 2020.

[90] K. S. Lau, S. X. Chin, S. T. Tan, F. S. Lim, W. S. Chang, C. C. Yap, M. H. H. Jumali, S. Zakaria, S. W. Chook, and C. H. Chia. Silver nanowires as flexible transparent electrode: Role of pvp chain length. *Journal of Alloys and Compounds*, 803:165–171, 2019.

[91] N. T. Le, N. A. Vu, and L. T. Loc. New type of smoluchowski temperature jump condition considering the viscous heat generation. *AIAA Journal*, 55:474–483, 2017.

[92] J. S. Lee, K. H. Choi, H. D. Ghim, S. S. Kim, D. H. Chun, H. Y. Kim, and W. S. Lyoo. Role of molecular weight of atactic poly(vinyl alcohol) (pva) in the structure and properties of pva nanofabric prepared by electrospinning. *Journal of Applied Polymer Science*, 93:1638–1646, 2004.

[93] L. J. Lee, C. Zeng, X. Cao, X. Han, J. Shen, and G. Xu. Polymer nanocomposite foams. *Composites Science and Technology*, 65:2344–2363, 2005.

[94] S. Lee, S. Shin, S. Lee, J. Seo, J. Lee, S. Son, H. J. Cho, H. Algadi, S. Al-Sayari, and D. E. Kim. Ag nanowire reinforced highly stretchable conductive fibers for wearable electronics. *Advanced Functional Materials*, 25:3114–3121, 2015.

[95] B. A. Legg and J. J. De Yoreo. Effects of size and shape on the tolerances for misalignment and probabilities for successful oriented attachment of nanoparticles. *Langmuir*, 39:2985–2994, 2023.

[96] C.-C. Li, S.-J. Chang, F.-J. Su, S.-W. Lin, and Y.-C. Chou. Effects of capping agents on the dispersion of silver nanoparticles. *Colloids and Surfaces A: Physicochemical and Engineering Aspects*, 419:209–215, 2013.

[97] D. Li, Q. Chen, J. Chun, K. Fichthorn, J. De Yoreo, and H. Zheng. Nanoparticle assembly and oriented attachment: correlating controlling factors to the resulting structures. *Chemical Reviews*, 123:3127–3159, 2023.

[98] J. Li, P. C. Ma, W. S. Chow, C. K. To, B. Z. Tang, and J. K. Kim. Correlations between percolation threshold, dispersion state, and aspect ratio of carbon nanotubes. *Advanced Functional Materials*, 17:3207–3215, 2007.

[99] J. Li, H. Rong, X. Tong, P. Wang, T. Chen, and Z. Wang. Platinum–silver alloyed octahedral nanocrystals as electrocatalyst for methanol oxidation reaction. *Journal of Colloid and Interface Science*, 513:251–257, 2018.

[100] M. Li, H. Jiang, and D. Xu. Preparation of sponge-reinforced silica aerogels from tetraethoxysilane and methyltrimethoxysilane for oil/water separation. *Materials Research Express*, 5:045003, 2018.

[101] W. Li, S. Yang, and A. Shamim. Screen printing of silver nanowires: balancing conductivity with transparency while maintaining flexibility and stretchability. *npj Flexible Electronics*, 3:13, 2019.

[102] Y. Li, Y. Wang, J. Wu, Y. Pan, H. Ye, and X. Zeng. Synthesis of silver nanowires using a polyvinylpyrrolidone-free method with an alpinia zerumbet leaf based on the oriented attachment mechanism. *ACS Omega*, 8:2237–2242, 2023.

[103] B. Liang, Y. Yang, and J. Li. Research progress of water-based release agents. In *MATEC Web of Conferences*, page 01033, 2022.

[104] X. Liang, T. Zhao, Y. Hu, and R. Sun. Dielectric properties of silver nanowires-filled polyvinylidene fluoride composite with low percolation threshold. *Journal of Nanoparticle Research*, 16:1–10, 2014.

[105] J.-M. Lim, G.-R. Yi, J. H. Moon, C.-J. Heo, and S.-M. Yang. Superhydrophobic films of electrospun fibers with multiple-scale surface morphology. *Langmuir*, 23:7981–7989, 2007.

[106] F. Liu, Z. Guo, H. Ling, Z. Huang, and D. Tang. Effect of pore structure on the adsorption of aqueous dyes to ordered mesoporous carbons. *Microporous and Mesoporous Materials*, 227:104–111, 2016.

[107] Q. Liu, G. Nian, C. Yang, S. Qu, and Z. Suo. Bonding dissimilar polymer networks in various manufacturing processes. *Nature Communications*, 9:846, 2018.

[108] R. Liu, T. Xu, and C.-a. Wang. A review of fabrication strategies and applications of porous ceramics prepared by freeze-casting method. *Ceramics International*, 42:2907–2925, 2016.

[109] S. Liu, J. Duvigneau, and G. J. Vancso. Nanocellular polymer foams as promising high performance thermal insulation materials. *European Polymer Journal*, 65:33–45, 2015.

[110] W. Liu, D. Haubold, B. Rutkowski, M. Oschatz, R. Hübner, M. Werheid, C. Ziegler, L. Sonntag, S. Liu, and Z. Zheng. Self-supporting hierarchical porous ptag alloy nanotubular aerogels as highly active and durable electrocatalysts. *Chemistry of Materials*, 28:6477–6483, 2016.

[111] Y. Liu, J. Gao, N. Guo, J. Sun, H. Hu, and X. Chi. Nonlinear conductivity and thermal stability of anti-corona epoxy resin nanocomposites. *Polymers*, 16:1296, 2024.

[112] Y. Liu, X. Yang, L. Yue, W. Li, W. Gan, and K. Chen. Selective dispersion of silver nanowires in epoxy/polyetherimide binary composites with enhanced electrical conductivity: a study of curing kinetics and morphology. *Polymer Composites*, 40:4390–4401, 2019.

[113] Z. Liu, Y. Wang, Y. Zu, Y. Fu, N. Li, N. Guo, R. Liu, and Y. Zhang. Synthesis of polyethylenimine (pei) functionalized silver nanoparticles by a hydrothermal method and their antibacterial activity study. *Materials Science and Engineering: C*, 42:31–37, 2014.

[114] C. Loretan and A. Muller. Nano, bits, and feynman's dream: There's plenty of room at the (molecular) bottom. *Journal of Chemical Education*, 100:1366–1370, 2023.

[115] H. Maleki, L. Durães, and A. Portugal. An overview on silica aerogels synthesis and different mechanical reinforcing strategies. *Journal of Non-Crystalline Solids*, 385:55–74, 2014.

[116] J. E. Mark. Some interesting things about polysiloxanes. *Accounts of Chemical Research*, 37:946–953, 2004.

[117] M. Mauzac, F. Hardouin, H. Richard, M. Achard, G. Sigaud, and H. Gasparoux. Effect of the chemical constitution of the side-chain on the formation and the structure of mesophases in some polysiloxanes. *European Polymer Journal*, 22:137–142, 1986.

[118] S. R. K. Meka, S. K. Verma, V. Agarwal, and K. Chatterjee. In situ silication of polymer nanofibers to engineer multi-biofunctional composites. *ChemistrySelect*, 3:3762–3773, 2018.

[119] B. Mekuye and B. Abera. Nanomaterials: An overview of synthesis, classification, characterization, and applications. *Nano Select*, 4:486–501, 2023.

[120] I. Mel'Nik, Y. L. Zub, B. Alonso, N. Abramov, and P. Gorbik. Creation of a functional polysiloxane layer on the surface of magnetic nanoparticles using the sol-gel method. *Glass Physics and Chemistry*, 38:96–104, 2012.

[121] H.-Y. Mi, X. Jing, H. Xie, H.-X. Huang, and L.-S. Turng. Magnetically driven superhydrophobic silica sponge decorated with hierarchical cobalt nanoparticles for selective oil absorption and oil/water separation. *Chemical Engineering Journal*, 337:541–551, 2018.

[122] D. Miao, N. Cheng, X. Wang, J. Yu, and B. Ding. Integration of janus wettability and heat conduction in hierarchically designed textiles for all-day personal radiative cooling. *Nano Letters*, 22:680–687, 2022.

[123] A. Moghe and B. Gupta. Co-axial electrospinning for nanofiber structures: preparation and applications. *Polymer Reviews*, 48:353–377, 2008.

[124] M. Moscardini, Y. Gan, S. Pupeschi, and M. Kamlah. Discrete element method for effective thermal conductivity of packed pebbles accounting for the smoluchowski effect. *Fusion Engineering and Design*, 127:192–201, 2018.

[125] M. Mozetič. *Surface modification to improve properties of materials*. MDPI, 2019.

[126] F. Müller, S. Jokisch, H. Bargel, and T. Scheibel. Centrifugal electrospinning enables the production of meshes of ultrathin polymer fibers. *ACS Applied Polymer Materials*, 2:4360–4367, 2020.

[127] G. Naz, H. Asghar, M. Ramzan, M. Arshad, R. Ahmed, M. B. Tahir, B. U. Haq, N. Baig, and J. Jalil. High-yield synthesis of silver nanowires for transparent conducting pet films. *Beilstein Journal of Nanotechnology*, 12:624–632, 2021.

[128] M. Neurock, M. Janik, and A. Wieckowski. A first principles comparison of the mechanism and site requirements for the electrocatalytic oxidation of methanol and formic acid over pt. *Faraday Discussions*, 140:363–378, 2009.

[129] Q. N. Nguyen, R. Chen, Z. Lyu, and Y. Xia. Using reduction kinetics to control and predict the outcome of a colloidal synthesis of noble-metal nanocrystals. *Inorganic Chemistry*, 60:4182–4197, 2021.

[130] V. Nguyen, W. Yoshida, J. D. Jou, and Y. Cohen. Kinetics of free-radical graft polymerization of 1-vinyl-2-pyrrolidone onto silica. *Journal of Polymer Science Part A: Polymer Chemistry*, 40:26–42, 2002.

[131] T. Ohji and M. Fukushima. Macro-porous ceramics: processing and properties. *International Materials Reviews*, 57:115–131, 2012.

[132] A. Oluwalowo, N. Nguyen, S. Zhang, J. G. Park, and R. Liang. Electrical and thermal conductivity improvement of carbon nanotube and silver composites. *Carbon*, 146:224–231, 2019.

[133] Y. Ouyang, H. Cao, H. Wu, D. Wu, F. Wang, X. Fan, W. Yuan, M. He, L. Y. Zhang, and C. M. Li. Tuning pt-skinned ptag nanotubes in nanoscales to efficiently modify electronic structure for boosting performance of methanol electrooxidation. *Applied Catalysis B: Environmental*, 265:118606, 2020.

[134] Z. Pásztory. An overview of factors influencing thermal conductivity of building insulation materials. *Journal of Building Engineering*, 44:102604, 2021.

[135] Z. Peng, H. You, and H. Yang. An electrochemical approach to ptag alloy nanostructures rich in pt at the surface. *Advanced Functional Materials*, 20:3734–3741, 2010.

[136] T. Pirzada, S. A. Arvidson, C. D. Saquing, S. S. Shah, and S. A. Khan. Hybrid silica–pva nanofibers via sol–gel electrospinning. *Langmuir*, 28:5834–5844, 2012.

[137] R. Prasher, P. E. Phelan, and P. Bhattacharya. Effect of aggregation kinetics on the thermal conductivity of nanoscale colloidal solutions (nanofluid). *Nano Letters*, 6:1529–1534, 2006.

[138] B. Pukánszky and E. Fekete. Adhesion and surface modification. In *Mineral Fillers in Thermoplastics I: Raw Materials and Processing*, pages 109–153. 1999.

[139] X. Qi, T. Balankura, Y. Zhou, and K. A. Fichthorn. How structure-directing agents control nanocrystal shape: polyvinylpyrrolidone-mediated growth of ag nanocubes. *Nano Letters*, 15:7711–7717, 2015.

[140] L. Qian and H. Zhang. Controlled freezing and freeze drying: a versatile route for porous and micro-/nano-structured materials. *Journal of Chemical Technology & Biotechnology*, 86:172–184, 2011.

[141] M. Qiao, H. Wu, F. Y. Meng, Z. Zhuang, and J. X. Wang. Defect-rich, highly porous ptag nanoflowers with superior anti-poisoning ability for efficient methanol oxidation reaction. *Small*, 18:2106643, 2022.

[142] C. Qiu, Y. Li, H. Liu, X. Wang, S. Hu, and H. Qi. A novel crosslinking strategy on functional cellulose-based aerogel for effective and selective removal of dye. *Chemical Engineering Journal*, 463:142404, 2023.

[143] K. Rozga-Wijas, J. Chojnowski, M. Ścibiorek, and W. Fortuniak. Polysiloxane–silica hybrids from novel precursors by the sol–gel process. *Journal of Materials Chemistry*, 15:2383–2392, 2005.

[144] M. Rafatullah, O. Sulaiman, R. Hashim, and A. Ahmad. Adsorption of methylene blue on low-cost adsorbents: a review. *Journal of Hazardous Materials*, 177:70–80, 2010.

[145] S. Rajpoot, R. Malik, and Y.-W. Kim. Effects of polysiloxane on thermal conductivity and compressive strength of porous silica ceramics. *Ceramics International*, 45:21270–21277, 2019.

[146] S. Reich, M. Burgard, M. Langner, S. Jiang, X. Wang, S. Agarwal, B. Ding, J. Yu, and A. Greiner. Polymer nanofibre composite nonwovens with metal-like electrical conductivity. *npj Flexible Electronics*, 2:5, 2018.

[147] L. Ren, Z. Tang, J. Du, L. Chen, and T. Qiang. Recyclable polyurethane foam loaded with carboxymethyl chitosan for adsorption of methylene blue. *Journal of Hazardous Materials*, 417:126130, 2021.

[148] A. P. Roberts and E. J. Garboczi. Elastic properties of model porous ceramics. *Journal of the American Ceramic Society*, 83:3041–3048, 2000.

[149] T. S. Rodrigues, A. G. da Silva, M. C. Goncalves, H. V. Fajardo, R. Balzer, L. F. Probst, A. H. da Silva, J. M. Assaf, and P. H. Camargo. Catalytic properties of agpt nanoshells as a function of size: larger outer diameters lead to improved performances. *Langmuir*, 32:9371–9379, 2016.

[150] I. Sabree, J. E. Gough, and B. Derby. Mechanical properties of porous ceramic scaffolds: influence of internal dimensions. *Ceramics International*, 41:8425–8432, 2015.

[151] M. Schmuck and M. Z. Bazant. Homogenization of the poisson–nernst–planck equations for ion transport in charged porous media. *SIAM Journal on Applied Mathematics*, 75:1369–1401, 2015.

[152] H. Shan, X. Dong, X. Cheng, Y. Si, J. Yu, and B. Ding. Highly flexible, meso-porous structured, and metallic cu-doped c/sio$_2$ nanofibrous membranes for efficient catalytic oxidative elimination of antibiotic pollutants. *Nanoscale*, 11:14844–14856, 2019.

[153] F.-Q. Shao, J.-J. Feng, Z.-Z. Yang, S.-S. Chen, J. Yuan, and A.-J. Wang. Cytosine assisted aqueous synthesis of agpt hollow alloyed nanostructures as highly active electrocatalyst for ethylene glycol oxidation and hydrogen evolution. *International Journal of Hydrogen Energy*, 42:24767–24775, 2017.

[154] G. Shao, D. A. Hanaor, X. Shen, and A. Gurlo. Freeze casting: from low-dimensional building blocks to aligned porous structures—a review of novel materials, methods, and applications. *Advanced Materials*, 32:1907176, 2020.

[155] J. Shen, C. Zeng, and L. J. Lee. Synthesis of polystyrene–carbon nanofibers nanocomposite foams. *Polymer*, 46:5218–5224, 2005.

[156] J. Sheng, Y. Xu, J. Yu, and B. Ding. Robust fluorine-free superhydrophobic amino-silicone oil/sio$_2$ modification of electrospun polyacrylonitrile membranes for waterproof-breathable application. *ACS Applied Materials & Interfaces*, 9:15139–15147, 2017.

[157] A. M. Signori, K. d. O. Santos, R. Eising, B. L. Albuquerque, F. C. Giacomelli, and J. B. Domingos. Formation of catalytic silver nanoparticles supported on branched polyethyleneimine derivatives. *Langmuir*, 26:17772–17779, 2010.

[158] A. G. Slater and A. I. Cooper. Function-led design of new porous materials. *Science*, 348:aaa8075, 2015.

[159] P. Song, H. Xu, B. Yan, J. Wang, F. Gao, Y. Zhang, Y. Shiraishi, and Y. Du. Particle size effects of ptag nanoparticles on the catalytic electrooxidation of liquid fuels. *Inorganic Chemistry Frontiers*, 5:1174–1179, 2018.

[160] M. Stolarski, J. Walendziewski, M. Steininger, and B. Pniak. Synthesis and characteristic of silica aerogels. *Applied Catalysis A: General*, 177:139–148, 1999.

[161] Y. Sun, B. Gates, B. Mayers, and Y. Xia. Crystalline silver nanowires by soft solution processing. *Nano Letters*, 2:165–168, 2002.

[162] Y. Sun, B. Mayers, T. Herricks, and Y. Xia. Polyol synthesis of uniform silver nanowires: a plausible growth mechanism and the supporting evidence. *Nano Letters*, 3:955–960, 2003.

[163] K. Sundmacher, T. Schultz, S. Zhou, K. Scott, M. Ginkel, and E. Gilles. Dynamics of the direct methanol fuel cell (dmfc): experiments and model-based analysis. *Chemical Engineering Science*, 56:333–341, 2001.

[164] R. Szabó and G. Lente. Deterministic approximation for the nucleation-growth type model of nanoparticle formation: A validation against stochastic simulations. *Chemical Engineering Journal*, 446:137377, 2022.

[165] D. Szmigiel, K. Domański, and P. Grabiec. Polysiloxane coatings on biomedical micro devices: plasma etching and properties of protection layer. *Advances in Science and Technology*, 57:220–225, 2009.

[166] S. Tan, M. Erol, A. Attygalle, H. Du, and S. Sukhishvili. Synthesis of positively charged silver nanoparticles via photoreduction of $agno_3$ in branched polyethyleneimine/hepes solutions. *Langmuir*, 23:9836–9843, 2007.

[167] A. Tataroglu, Ş. Altındal, and M. Bülbül. Temperature and frequency dependent electrical and dielectric properties of Al/SiO_2/p-Si (MOS) structure. *Microelectronic Engineering*, 81:140–147, 2005.

[168] A. K. Tiwari, M. K. Gupta, G. Pandey, S. Pandey, and P. C. Pandey. Amine-functionalized silver nanoparticles: A potential antiviral-coating material with trap and kill efficiency to combat viral dissemination (covid-19). *Biomedical Materials & Devices*, 1:618–632, 2023.

[169] M. Tsuji, M. Ogino, M. Matsunaga, N. Miyamae, R. Matsuo, M. Nishio, and M. J. Alam. Crystal structures and growth mechanisms of icosahedral au@ag core-shell and au/ag twin nanocrystals prepared by pvp-assisted n,n-dimethylformamide reduction. *Crystal Growth & Design*, 10:4085–4090, 2010.

[170] A. von Harpe, H. Petersen, Y. Li, and T. Kissel. Characterization of commercially available and synthesized polyethylenimines for gene delivery. *Journal of Controlled Release*, 69:309–322, 2000.

[171] M. Wan, J. Tao, D. Jia, X. Chu, S. Li, S. Ji, and C. Ye. High-purity very thin silver nanowires obtained by ostwald ripening-driven coarsening and sedimentation of nanoparticles. *CrystEngComm*, 20:2834–2840, 2018.

[172] L. Wang, D. Liu, Z. Zhang, Y. Li, J. Liu, Y. Yang, B. Xue, and F. Li. Self-adaptively electrochemical reconstruction of nife-layered double hydroxide on ni foam for high-performance water splitting. *Journal of Alloys and Compounds*, 934:167846, 2023.

[173] Q. Wang, S. Zhang, G. Liu, T. Lin, and P. He. The mixture of silver nanowires and nanosilver-coated copper micronflakes for electrically conductive adhesives to achieve high electrical conductivity with low percolation threshold. *Journal of Alloys and Compounds*, 820:153184, 2020.

[174] X. Wang, Z. Li, J. Shi, and Y. Yu. One-dimensional titanium dioxide nanomaterials: nanowires, nanorods, and nanobelts. *Chemical Reviews*, 114:9346–9384, 2014.

[175] Z. Wang, C. Liu, and Q. Chen. In-situ imaging of nucleation and growth of superlattices from nanoscale colloidal nanoparticles. *Journal of Crystal Growth*, 601:126955, 2023.

[176] Z. Wang, J. Liu, X. Chen, J. Wan, and Y. Qian. A simple hydrothermal route to large-scale synthesis of uniform silver nanowires. *Chemistry–A European Journal*, 11:160–163, 2005.

[177] M. Wellons. The stefan-boltzmann law, 2007.

[178] X. Weng, Q. Liu, J.-J. Feng, J. Yuan, and A.-J. Wang. Dendrite-like ptag alloyed nanocrystals: Highly active and durable advanced electrocatalysts for oxygen reduction and ethylene glycol oxidation reactions. *Journal of Colloid and Interface Science*, 504:680–687, 2017.

[179] X. Weng, Q. Liu, A.-J. Wang, J. Yuan, and J.-J. Feng. Simple one-pot synthesis of solid-core@porous-shell alloyed ptag nanocrystals for the superior catalytic activity toward hydrogen evolution and glycerol oxidation. *Journal of Colloid and Interface Science*, 494:15–21, 2017.

[180] R. J. White, R. Luque, V. L. Budarin, J. H. Clark, and D. J. Macquarrie. Supported metal nanoparticles on porous materials. methods and applications. *Chemical Society Reviews*, 38:481–494, 2009.

[181] C. B. Whitehead, S. Özkar, and R. G. Finke. Lamer's 1950 model of particle formation: a review and critical analysis of its classical nucleation and fluctuation theory basis, of competing models and mechanisms for phase-changes and particle formation, and then of its application to silver halide, semiconductor, metal, and metal-oxide nanoparticles. *Materials Advances*, 2:186–235, 2021.

[182] M. Xie, H. Lu, L. Zhang, J. Wang, Q. Luo, J. Lin, L. Ba, H. Liu, W. Shen, and L. Shi. Fully solution-processed semi-transparent perovskite solar cells with ink-jet printed silver nanowires top electrode. *Solar RRL*, 2:1700184, 2018.

[183] F. Xu and Y. Zhu. Highly conductive and stretchable silver nanowire conductors. *Advanced Materials*, 24:5117–5122, 2012.

[184] J. Xue, T. Wu, Y. Dai, and Y. Xia. Electrospinning and electrospun nanofibers: Methods, materials, and applications. *Chemical Reviews*, 119:5298–5415, 2019.

[185] M. T. Yagub, T. K. Sen, S. Afroze, and H. M. Ang. Dye and its removal from aqueous solution by adsorption: a review. *Advances in Colloid and Interface Science*, 209:172–185, 2014.

[186] H. Yang, T. Chen, H. Wang, S. Bai, and X. Guo. One-pot rapid synthesis of high aspect ratio silver nanowires for transparent conductive electrodes. *Materials Research Bulletin*, 102:79–85, 2018.

[187] Q. Yang, Z. Li, Y. Hong, Y. Zhao, S. Qiu, C. Wang, and Y. Wei. Influence of solvents on the formation of ultrathin uniform poly(vinyl pyrrolidone) nanofibers with electrospinning. *Journal of Polymer Science Part B: Polymer Physics*, 42:3721–3726, 2004.

[188] L. Yaqoob, T. Noor, and N. Iqbal. Recent progress in development of efficient electrocatalyst for methanol oxidation reaction in direct methanol fuel cell. *International Journal of Energy Research*, 45:6550–6583, 2021.

[189] A. Yarin. Coaxial electrospinning and emulsion electrospinning of core–shell fibers. *Polymers for Advanced Technologies*, 22:310–317, 2011.

[190] C. C. Yec and H. C. Zeng. Synthesis of complex nanomaterials via ostwald ripening. *Journal of Materials Chemistry A*, 2:4843–4851, 2014.

[191] K. Yin, P. Divakar, and U. G. Wegst. Freeze-casting porous chitosan ureteral stents for improved drainage. *Acta Biomaterialia*, 84:231–241, 2019.

[192] J. Yoon, H. S. Yang, B. S. Lee, and W. R. Yu. Recent progress in coaxial electrospinning: New parameters, various structures, and wide applications. *Advanced Materials*, 30:1704765, 2018.

[193] A. B. Yousaf, M. Imran, A. Zeb, T. Wen, X. Xie, Y.-F. Jiang, C.-Z. Yuan, and A.-W. Xu. Single phase ptag bimetallic alloy nanoparticles highly dispersed on reduced graphene oxide for electrocatalytic application of methanol oxidation reaction. *Electrochimica Acta*, 197:117–125, 2016.

[194] Y. Yousefi and F. Tariku. Thermal conductivity and specific heat capacity of insulation materials at different mean temperatures. 012090, 2021.

[195] M. Zandieh and J. Liu. Nanozymes: definition, activity, and mechanisms. *Advanced Materials*, 36:2211041, 2024.

[196] J. Zeng, Z. Cao, D. Yang, L. Sun, and L. Zhang. Thermal conductivity enhancement of ag nanowires on an organic phase change material. *Journal of Thermal Analysis and Calorimetry*, 101:385–396, 2010.

[197] C. Zhang, L. Qu, Y. Wang, T. Xu, and C. Zhang. Thermal insulation and stability of polysiloxane foams containing hydroxyl-terminated polydimethylsiloxanes. *RSC Advances*, 8:9901–9909, 2018.

[198] Y.-H. Zhao, Z.-K. Wu, and S.-L. Bai. Thermal resistance measurement of 3d graphene foam/polymer composite by laser flash analysis. *International Journal of Heat and Mass Transfer*, 101:470–475, 2016.

[199] S. Zheng, X. Wang, W. Li, Z. Liu, Q. Li, and F. Yan. Pressure-stamped stretchable electronics using a nanofibre membrane containing semi-embedded liquid metal particles. *Nature Electronics*, pages 1–10, 2024.

[200] W. Zhou, X. Yu, Y. Li, W. Jiao, Y. Si, J. Yu, and B. Ding. Green-solvent-processed fibrous membranes with water/oil/dust-resistant and breathable performances for protective textiles. *ACS Applied Materials & Interfaces*, 13:2081–2090, 2020.

[201] D.-M. Zhu and H.-F. Weng. Thermal conductivity and heat capacity study of a densified a-sio$_2$. *Journal of Non-Crystalline Solids*, 185:262–267, 1995.

(Eidesstattliche) Versicherungen und Erklärungen

(§9 Satz 2 Nr. 3 PromO BayNAT)

Hiermit versichere ich eidesstattlich, dass ich die Arbeit selbstständig verfasst und keine anderen als die von mir angegebenen Quellen und Hilfsmittel benutzt habe (vgl. Art. 97 Abs. 1 Satz 8 BayHIG).

(§9 Satz 2 Nr. 3 PromO BayNAT)

Hiermit erkläre ich, dass ich die Dissertation nicht bereits zur Erlangung eines akademischen Grades eingereicht habe und dass ich nicht bereits diese oder eine gleichartige Doktorprüfung endgültig nicht bestanden habe.

(§9 Satz 2 Nr. 4 PromO BayNAT)

Hiermit erkläre ich, dass ich Hilfe von gewerblichen Promotionsberatern bzw. - vermittlern oder ähnlichen Dienstleistern weder bisher in Anspruch genommen habe noch künftig in Anspruch nehmen werde.

(§9 Satz 2 Nr. 7 PromO BayNAT)

Hiermit erkläre ich mein Einverständnis, dass die elektronische Fassung meiner Dissertation unter Wahrung meiner Urheberrechte und des Datenschutzes einer gesonderten Überprüfung unterzogen werden kann.

(§9 Satz 2 Nr. 8 PromO BayNAT)

Hiermit erkläre ich mein Einverständnis, dass bei Verdacht wissenschaftlichen Fehlverhaltens Ermittlungen durch universitätsinterne Organe der wissenschaftlichen Selbstkontrolle stattfinden können.

. . . . . .

Ort, Datum, Unterschrift